HYDROLOGY OF A FIRN AQUIFER IN SOUTHEAST GREENLAND

by

Olivia Leigh Miller

A dissertation submitted to the faculty of
The University of Utah
in partial fulfillment of the requirements for the degree of

Doctor of Philosophy

in

Geology

Department of Geology and Geophysics

The University of Utah

August 2017

The University of Utah Graduate School

STATEMENT OF DISSERTATION APPROVAL

The dissertation of **Olivia Leigh Miller**

has been approved by the following supervisory committee members:

Douglas Kip Solomon	, Chair	**6/8/2017** Date Approved
Brenda B. Bowen	, Member	**6/12/2017** Date Approved
Thure E. Cerling	, Member	**6/8/2017** Date Approved
Richard R. Forster	, Member	**6/8/2017** Date Approved
Lora S. Koenig	, Member	**5/19/2017** Date Approved

and by **Thure E. Cerling**, Chair/Dean of

the Department/College/School of **Geology and Geophysics**

and by David B. Kieda, Dean of The Graduate School.

ABSTRACT

The Greenland ice sheet is losing mass, which can contribute to sea level rise. Firn aquifers covering between 22,000 – 90,000 km^2 have been discovered within the ice sheet. In summer, surface snowmelt infiltrates to depth, saturating pore space within the compacting firn. Recharge ceases when the surface temperatures cool below 0ºC in the fall. Instead of refreezing, the meltwater stays in liquid phase throughout the year because of the insulation produced by high snow accumulation rates. This liquid flows through the firn, and discharges from the aquifer, likely to crevasses at the edge of the ice sheet. Flow through the firn behaves according to Darcy's law. The firn aquifer is a modern feature of the ice sheet, likely caused by warming of the Arctic associated with global climate change. Water in the aquifer recharged the aquifer within the past ~50 years. Instead of permanently storing meltwater, either through refreezing or simple storage in pore space, firn aquifers allow large volumes of meltwater to discharge from the ice sheet. The fate of that meltwater and its pathways to the ocean remain unknown and require further work as some scenarios (e.g., hydrofracturing crevasses leading to basal lubrication) could play important roles in accelerating ice flow and discharge to the ocean.

TABLE OF CONTENTS

LIST OF TABLES

Tables

LIST OF FIGURES

Figures

ACKNOWLEDGEMENTS

This has been the graduate school experience of a lifetime, and I am grateful for the opportunity to work on such an interesting and exciting research question with such an insightful, efficient, and friendly group of people. I would like to thank my advisor, Kip Solomon, for his thoughtful, patient, and constructive guidance (and for sharing his favorite powder stashes with me). Kip provided the freedom and focus I needed to complete this dissertation. I would like to thank Brenda Bowen and Jim Ehleringer for their support through the Global Change and Sustainability Center, in addition to their positive mentorship throughout my time at the University of Utah. I am thankful to Rick Forster and Lora Koenig for teaching me all about glaciology and doing fieldwork in Greenland, and for their thoughtful guidance to address our research questions. I thank Thure Cerling for encouraging me to think about the big picture questions in science. I couldn't have done the numerical simulations without the tenacious cooperation and humor from Clifford Voss. Thanks to Clément Miège, Lynn Montgomery, and Nicholas Schmerr for being so responsive to requests for assistance, teaching me about their research and about doing fieldwork in Greenland, and always having a positive attitude. I appreciate all the advice and assistance from Wil Mace, Stewart Gubler, Alan Rigby, Stefan Ligtenberg, and Anatoly Legchenko. I appreciate the support and opportunities provided through the Geology and Geophysics Department, and the Think Globally, Learn Locally, and STEM Ambassadors programs at the University of Utah. I gratefully acknowledge that this work was made possible through grants from the National Science

Foundation and National Aeronautics and Space Administration.

Thanks also to Joe McConnell for firn core salt data and Lawrence Spangler for assistance with fluorescein dye analysis. I would also like to thank Kyli Cosper, Kathy Young, and the entire CH2M Polar Field Services team for logistical assistance. Thanks also to Josh Goetz and IDDO for drilling support in April, 2015 and Jay Kyne for drill consultation and development.

A huge thanks to my friends and family for their constant support and encouragement over the years. I couldn't do this without you.

CHAPTER 1

INTRODUCTION

The Greenland ice sheet (GrIS) reacts to and mediates the Earth's climate. Warming of the Arctic has impacted the GrIS significantly. The ice sheet is losing mass and the rate of loss is increasing [*Shepherd et al.*, 2012]. Melt area is expanding, melt seasons are getting longer, the ice sheet is thinning, and glaciers are flowing faster to the ocean [*Vaughan et al.*, 2013; *Richter-Menge et al.*, 2016]. The GrIS contains the second largest ice volume on the world, after Antarctica, and would raise sea level ~7 m if it all melted.

Sea level has risen over the past 100 years, and this is likely to continue as the Earth continues to warm. Current sea level rise is approximately equally distributed between increased meltwater input from land ice and the expansion of the ocean water as it warms. Even if CO_2 emissions stabilized, sea level rise will almost certainly continue for many centuries [*IPCC*, 2014]. Thermal expansion will also increase as temperatures increase [*Church et al.*, 2013]. The GrIS can contribute to sea level rise either through surface runoff or ice discharge into the ocean. Mass losses from either process have been roughly equal in past decades, although recent surface mass balance losses are accelerating and have outpaced ice discharge [*Enderlin et al.*, 2014].

Sea level rise will impact global populations. People who live in low-lying areas near the ocean face increased risks of flooding, extreme weather events, food insecurity,

increased coastal erosion, loss of marine ecosystems and their services. Even people who don't live in coastal areas may be affected as coastal systems are disrupted. For example, if a coastal area is flooded, people may have to move inland. If fishing industries are disrupted, food supply for inland people may be reduced as well.

The cost of climate change, while difficult to estimate, will be large and depends on a wide range of complex systems including future supply of resources, the labor market, supply and demand, and technological advances. Still, in the US the cost of a 1 m rise in sea level has been estimated at between $270 and $475 billion, ignoring future development [*Titus et al.*, 1991]. This cost comes from pumping sand onto beaches to protect ocean resort communities, levees and bulkheads to protect developed areas, and the loss of coastal wetlands and undeveloped lowlands. Smart planning for the future requires understanding how the Earth system is currently changing, and how that may evolve in the future.

In 2011, researchers discovered a firn aquifer in the Greenland ice sheet [*Forster et al.*, 2014; *Koenig et al.*, 2014]. Firn aquifers form in areas of high accumulation and melt rates [*Kuipers Munneke et al.*, 2014]. The accumulation provides adequate pore space and thermal insulation from cold surface temperatures during the winter while the high melt rates provide adequate liquid and associated heat for liquid water to persist throughout the year.

Firn aquifers have been observed in mountain glaciers in the Alps, the Cascades, Japan, and Svalbard [*Vallon et al.*, 1976; *Oerter and Moser*, 1982; *Fountain*, 1989; *Kawashima*, 1997; *Nienow et al.*, 1998; *Schneider and Jansson*, 2004; *Christianson et al.*, 2015]. Compared to the GrIS firn aquifer system, these firn aquifers are much smaller in extent, are steeper, can be much shallower or of similar depth, and either fully or partially

drain annually.

Although meltwater retention in firn in Greenland had previously been described [*Humphrey et al.*, 2012], the scale of these firn aquifers is much larger. They cover ~20,000 – 90,000 km^2 between ~1200 – 2000 m elevation range [*Forster et al.*, 2014; *Miège et al.*, 2016; *Steger et al.*, 2017]. The water table ranges between 5-50m, and at one site in southeast Greenland, have an average thickness of 11 m [*Forster et al.*, 2014; *Montgomery et al.*, 2017]. This discovery highlighted significant gaps in our understanding of ice sheet hydrology and the related implications for ice sheet mass balance and sea level rise.

Ice sheet mass loss is the largest uncertainty in future projections of sea level rise [*Cazenave*, 2006]. In order to predict future GrIS mass balance, we need to understand the role firn aquifers currently play in the mass balance, and how they may evolve under a warming climate. Improved understanding of ice sheet mass balance will allow us to plan wisely for future changes.

Meltwater on an ice sheet can either runoff or remain stored within the ice sheet as internal accumulation. Along this spectrum of behaviors, firn aquifers temporarily store water inside firn that may eventually flow to the ocean [*Poinar et al.*, 2017]. Firn aquifers are not currently included in any climate, ice sheet, or sea level rise models. In order to include firn aquifers in these models, some basic understanding of their formation and existence is needed.

Building on the initial discovery of the aquifer, my research group has now defined the geometry, flow rates and patterns, age, and water volume of the aquifer. We focused our field work on an ice flow line upstream from Helheim Glacier, the fifth largest contributor of ice discharge to the ocean from Greenland [*Enderlin et al.*, 2014].

This site has a long history of airborne radar surveys as part of NASA's Operation IceBridge enabling assessment of water table changes over time. Over the course of three field visits, we installed instruments to monitor firn temperature and aquifer water levels, logged ice cores at five sites, made nearly 150 hydraulic conductivity measurements, measured fluid flow at three sites, and collected tritium and chlorofluorocarbon samples at six sites, in addition to ~15 km profile of active source seismic surveys and magnetic resonance soundings.

In the following chapters, I describe measurements of aquifer hydraulic properties, flow within the aquifer, aquifer recharge, aquifer timescales, and a conceptual model of the firn aquifer backed by numerical simulations. Chapters were written as individual papers. Therefore, some of the introductory material is repeated. Although I have developed an understanding of the basic components of this hydrologic system, many questions remain related to aquifer formation and evolution, and the role the aquifer plays in the englacial and subglacial hydrologic system, and the associated impacts on ice dynamics. Firn aquifers have been thought to influence glacier velocity behavior [*Moon et al.*, 2014]. Meltwater discharging from the aquifer may hydrofracture crevasses to the base of the ice sheet [*Mcnerney*, 2016; *Poinar et al.*, 2017], and potentially increase ice flow rates, which are variable for Helheim Glacier [*Howat et al.*, 2007; *Moon et al.*, 2012]. This connection to the broader hydrologic system, and the associated implications to sea level rise, remain unknown, and require further work.

CHAPTER 2

HYDRAULIC CONDUCTIVITY OF A FIRN AQUIFER IN SOUTHEAST GREENLAND [1]

2.1 Abstract

Some regions of the Greenland ice sheet, where snow accumulation and melt rates are high, currently retain substantial volumes of liquid water within the firn pore space throughout the year. These firn aquifers, found between ~10-30 m below the snow surface, may significantly affect sea level rise by storing or draining surface meltwater. The hydraulic gradient and the hydraulic conductivity control flow of meltwater through the firn. Here we describe the hydraulic conductivity of the firn aquifer estimated from slug tests and aquifer tests at six sites located upstream of Helheim Glacier in southeastern Greenland. We conducted slug tests using a novel instrument, a piezometer with a heated tip that melts itself into the ice sheet. Hydraulic conductivity ranges between 2.5×10^{-5} and 1.1×10^{-3} m/s. The geometric mean of hydraulic conductivity of the aquifer is 2.7×10^{-4} m/s with a geometric standard deviation of 1.4 from both depth specific slug tests (analyzed using the Hvorslev method) and aquifer tests during the

---

This chapter has been published as Miller, O. L., D. K. Solomon, C. Miège, L. Koenig, R. R. Forster, L. N. Montgomery, N. Schmerr, S. Ligtenberg, A. Legtchenko, and L. Brucker (2017), Hydraulic conductivity of a firn aquifer in southeast Greenland, *Front. Earth Sci.*, *5*, 38, doi:10.3389/FEART.2017.00038. Reprinted with permission.

recovery period. Hydraulic conductivity is relatively consistent between boreholes and only decreases slightly with depth. The hydraulic conductivity of the firn aquifer is crucial for determining flow rates and patterns within the aquifer, which inform hydrologic models of the aquifer, its relation to the broader glacial hydrologic system, and its effect on sea level rise.

2.2 Introduction

Across the percolation zone of the southeast portion of the Greenland ice sheet, surface meltwater infiltrates to depth within the ice sheet, where it currently forms an extensive firn aquifer. The firn aquifer contains liquid water within the pore space of the compacting snow/firn throughout the year at depths of ~10-30 m. Initially documented in 2011 [*Forster et al.*, 2014], the aquifer has been identified and monitored with ground penetrating radar, airborne radar, and in situ measurements since then [*Koenig et al.*, 2014; *Miège et al.*, 2016]. Over the entire ice sheet, firn aquifers are estimated to cover an area between 20,000 - 70,000 km^2, with ~50% of this total extent located in the southeastern portion of the ice sheet [*Forster et al.*, 2014; *Miège et al.*, 2016]. Firn aquifers form in areas with a combination of high accumulation and high melt rates [*Forster et al.*, 2014; *Kuipers Munneke et al.*, 2014]. Complete drainage of the aquifer could contribute up to 0.4 mm to sea level rise globally [*Koenig et al.*, 2014].

In a firn aquifer, water storage occurs as meltwater fills firn pore space until the residual liquid water content of the firn is achieved, which allows horizontal flow to occur [*Freeze and Cherry*, 1979; *Pfeffer et al.*, 1991]. Water flow within the firn aquifer may allow surface meltwater originating far from the edge of the ice sheet to discharge to the ocean. The saturation of the firn allows more meltwater that would otherwise rest in

pore spaces if the firn remained unsaturated to flow laterally. Crevasses at the edge of the ice sheet represent one possible pathway for aquifer water to discharge to the ocean [*Alley et al.*, 2005; *Chu*, 2014; *Koenig et al.*, 2014]. Transport of liquid water to the base of the ice sheet, likely via crevasses [*Miège et al.*, 2016; *Poinar et al.*, 2017] may also influence ice dynamics and ice discharge to the ocean [e.g., *Zwally*, 2002; *Joughin et al.*, 2008; *Sole et al.*, 2011a].The hydrologic properties of the aquifer and its connections to the broader glacier hydrologic system remain unclear. The aquifer may be storing meltwater and buffering sea level rise, or it may be constantly draining and routing water toward the ocean. To characterize the connection between surface melt and discharge to the ocean, and quantify water flow, hydraulic properties of the aquifer are required.

This process of water storage and transport differs from meltwater discharge to the ocean in other parts of Greenland, where inland meltwater is routed through surface lakes and streams to crevasses and moulins [*Das et al.*, 2008; *Lewis and Smith*, 2009; *Chu*, 2014; *Smith et al.*, 2015]. In some areas outside of firn aquifer regions, thick ice layers prevent meltwater percolation to depth and surface runoff is favored, contributing to sea level rise [*Machguth et al.*, 2016]. In other areas, meltwater storage occurs by refreezing in the firn, buffering sea level rise [*Pfeffer et al.*, 1991; *Harper et al.*, 2012].

The storage and transmission of meltwater through firn is similar in many ways to water flow through a rocky or unconsolidated porous media, where water flows from recharge to discharge areas (high hydraulic head to low hydraulic head). The undulating water table observed in radar profiles [*Forster et al.*, 2014] resembles the topographically driven flow of an unconfined aquifer [*Tóth*, 1963]. In the unsaturated zone above the water table, where fluid pressures are less than atmospheric, pores can contain both gas and liquid. The aquifer is defined as the saturated zone below the water table, where fluid

pressures are positive. Isolated gas phases within the saturated zone can exist. We conceptualize saturated groundwater flow to follow Darcy's law:

$$q = \frac{Q}{A} = -K\frac{\partial h}{\partial x} \tag{2.1}$$

where q is the specific discharge (length/time), Q is the discharge (length^3/time), A is the cross sectional area across which flow occurs (length^2), K is the hydraulic conductivity (length/time), h is the hydraulic head (length) and x is the distance (length). To quantify aquifer discharge, the hydraulic gradient can be estimated from ground penetrating radar surveys of the aquifer but site-specific in situ measurements of hydraulic conductivity are needed.

Hydraulic conductivity is typically measured in situ by two major techniques: aquifer tests and piezometer tests [*Freeze and Cherry*, 1979]. Each test introduces a different hydraulic stress to the system. Aquifer tests involve injecting or pumping water from or into an aquifer at a controlled rate and observing the change in water level over time. Slug tests, a type of piezometer test, involve instantaneously changing the hydraulic head within a well and recording recovery in that well over time [*Hvorslev*, 1951; *Butler*, 1997]. Both tests induce horizontal flow within the aquifer, and therefore indicate horizontal hydraulic conductivity. Slug tests can provide depth-specific measurements of hydraulic conductivity within a formation. However, the conditions immediately surrounding the piezometer have a larger influence on slug test results.

Aquifer tests assess the hydraulic properties, including hydraulic conductivity, of an aquifer over a larger area (~m – km) than slug tests because they perturb a larger

volume of water over a longer period of time [*Ferris et al.*, 1962]. Thus, aquifer tests are less subject to formation disturbance caused by the drilling or melting processes that may alter hydraulic conductivity close to the borehole or piezometer. As a result, aquifer tests generally provide a better estimate of the effective hydraulic parameters of an aquifer than slug tests. However, they are technically more difficult to conduct, require more equipment, and take longer than slug tests. The water level response during the recovery period of an aquifer test can provide the most accurate estimate of hydraulic conductivity as it is generally independent of well construction or pumping effects. A comparison of slug and aquifer test results, as is presented in this manuscript, can provide a comprehensive estimate of the hydraulic conductivity within an aquifer.

Firn aquifers have been observed in mountain glaciers, and their hydraulic conductivities have been measured using slug tests and aquifer tests [*Oerter and Moser*, 1982; *Oerter et al.*, 1983; *Fountain*, 1989; *Fountain and Walder*, 1998; *Schneider*, 1999; *Jansson et al.*, 2003]. Slug tests have also been used to estimate subglacial hydraulic properties [*Stone and Clark*, 1972; *Iken et al.*, 1996; *Kulessa et al.*, 2005; *Meierbachtol et al.*, 2008]. Hydraulic conductivity depends on properties of both the porous media (grain size, shape, distribution, and packing) and the fluid (viscosity and density). Firn permeability, which only depends on porous media properties, has been measured at various sites across Greenland using permeameters [*Albert and Shultz*, 2002; *Adolph and Albert*, 2014; *Keegan et al.*, 2014] and Antarctica [*Albert et al.*, 2000, 2004]. Hydraulic conductivity (K) is related to permeability (k) as:

$$K = \frac{k\rho g}{\mu} \tag{2.2}$$

where ρ is fluid density, g is the acceleration due to gravity, and μ is the fluid dynamic viscosity. These parameters can shed light on the depositional and metamorphic history of the firn.

In this manuscript, we describe the methods and results of field experiments conducted to determine, for the first time, the hydraulic conductivity of a firn aquifer in the southeastern area of the Greenland ice sheet. Mathematical solutions to determine hydraulic conductivity involve matching curves to water displacement data. These results, combined with aquifer geometry, are essential to developing a hydrologic model of the firn aquifer and understanding the impact of the aquifer on ice sheet mass balance estimates.

2.3 Materials and Methods

2.3.1 Site Description

The study site is located along an elevation gradient of an ice flow line upstream of Helheim Glacier in southeast Greenland (Figure 2.1). Field work was conducted approximately 40 km west of the glacier front in April, July, and August 2015, and July and August 2016. Five 6.4 cm diameter boreholes were drilled with an electrothermal drill to ~50 m depth, and a heated piezometer, described in Section 2.3.2, was installed at 6 sites (Table 2.1) to a maximum depth of almost 40 m. At two of those drilling sites, piezometers were installed less than 5 m away from the borehole to perform aquifer tests. The 6.4 cm diameter holes were enlarged with a heated reamer to 8 cm diameter in order to accommodate the pump inside the borehole.

We determined the thickness of the aquifer using in situ and geophysical methods. We measured the depth to the water table with both a chalked steel tape [*Garber and*

Koopman, 1968] and with ground penetrating radar [*Forster et al.*, 2014; *Miège et al.*, 2016]. We also determined the bottom of the aquifer with a borehole dilution test. Briefly, during the borehole dilution test, we mixed a small amount of saltwater into the 8 cm diameter borehole and measured the specific conductance of the water within the borehole at 30 cm intervals over ~20 hours. The reduction in specific conductance due to inflow of freshwater is proportional to the specific discharge through the borehole. Within the aquifer, the change in specific discharge was significant, but below a certain depth, the specific discharge did not change, indicating the bottom of the flow zone. We only did this test in 2016. The other method to determine the bottom of the aquifer is with a seismic survey, described in *Montgomery et al.* [2017]. The depth to the water table and aquifer bottom and aquifer thickness using each method at each site are shown in Table 2.2. The thickness of the saturated zone determined by the borehole dilution test was used where available. The seismic bottom depths were also used. The borehole dilution and seismic thicknesses do not perfectly agree (5-17 m differences) and so a range of thicknesses were used for the hydraulic conductivity estimates.

2.3.2 Heated Piezometer

A piezometer, commonly used in groundwater hydrology, consists of a sealed pipe with an open end installed in the porous media to measure depth-specific hydraulic heads. We adapted a piezometer to penetrate the numerous ice lenses within the firn through the addition of a heated tip that allows the piezometer to advance by melting through the firn and ice (Figure 2.2). The 3 cm diameter piezometer standpipe is closed along its entire length except for a 32 cm screened interval near the tip which allows water to enter or exit when advanced below the water table. The casing radius is 1.5 cm,

and the well radius is 1.5 cm. The piezometer also features a 108 cm long packer made of rubber surgical tubing, which can be inflated from the surface and allows for depth-specific measurements and water sampling. A generator at the surface powers the 500 watt heated tip. A power cable and hollow tube to inflate the packer run from the surface to the heated tip and packer along the inside of the metal pipe above the packer. A bicycle pump is used to inflate the packer, which surrounds a section of the metal pipe above the screened interval, to a pressure of approximately 1.7 atm (25 psi) above the water pressure.

As the piezometer melts through the firn, additional lengths (1.5 m) of threaded pipe are added at the surface. The pipe allows the creation of a sealed volume required to accumulate enough pressure to displace water during the slug tests. The walls of the piezometer were flush to the firn. The piezometer advances at a rate of approximately 13 cm/min in firn with a density below ~600 kg/m^3 and approximately 3 cm/min in firn and ice above a density of ~600 kg/m^3. We advanced the piezometer to a maximum depth of 38 m, limited by the length of pipe available in the field, but in concept could go deeper. The temperature at the maximum piezometer depth was 0°C (± 0.2°C), from borehole temperature sensors. Although never encountered, firn or ice temperatures below 0°C could cause the piezometer to freeze into the ice.

We removed the piezometer with a tripod equipped with a hand winch. The pipe can be pulled out by hand, but can be heavy enough that the tripod pulley system is safer. The piezometer standpipes were commercially available while the tip and packer were custom fabricated. Prior to use on the Greenland ice sheet, the piezometer was tested in ice blocks and on a frozen lake.

2.3.3 Slug Tests

Slug tests are widely used to determine hydraulic conductivity in the saturated zone [*Kruseman et al.*, 1994]. During a slug test, water within a piezometer is displaced, and the recovery, which depends on the hydraulic properties of the aquifer, is recorded (Figure 2.3). These tests are made depth-specific when a seal is formed between the screened interval of the piezometer and the porous media above.

At each site, the piezometer was used to conduct depth-specific slug tests, resulting in profiles of hydraulic conductivity with depth. After the piezometer melted to a desired depth below the water table, the packer was inflated and a pressure transducer was inserted into the piezometer standpipe until it was below the water table but above the screened interval. The piezometer was closed at the top using a PVC manifold with seals around the power and pressure transducer cables. Air was then pumped into the metal standpipes using a bicycle pump to displace water out of the screened interval (the only outlet in the piezometer) at the bottom of the piezometer. Once the water level was lowered to the pressure transducer, a valve at the surface was opened to instantaneously release the air pressure and allow water to flow back into the piezometer through the screened interval. Displacement ranged from 0.3 – 6 m, depending on the depth of the piezometer tip (less for shallower tests). The pressure transducer recorded pressure at 1 second intervals. Tests were repeated at each depth between 1 and 3 times. Sampling frequency varied from site to site. Slug tests were conducted every 0.3 m at FA15_1, every 3 m at FA15_2, every 4.5 m at FA15_3, every 3 m at FA16_4, and FA16_5, and ~every 7 m at FA16_6. A total of 145 slug tests were conducted across the 6 sites.

The hydraulic conductivity of an aquifer can be estimated from slug test data through several curve fitting techniques. The firn aquifer is considered unconfined

because no continuous, impermeable boundaries above the water table have been observed. The methods of both *Hvorslev* [1951], originally developed for a confined aquifer, and *Bouwer and Rice* [1976], developed for unconfined aquifers, are used in this study. The Hvorselv method for a confined aquifer can be applied to an unconfined aquifer because the water table boundary in an unconfined aquifer does not greatly affect the slug test response as long as the well screen is fully below the water table [*Hvorslev,* 1951; *Bouwer and Rice,* 1976]. Both the Hvorslev method and the Bouwer and Rice solution for slug test analysis of an unconfined aquifer assume the aquifer has an infinite aerial extent and is homogeneous, and of uniform thickness [*Hvorslev,* 1951; *Bouwer and Rice,* 1976]. Further, they are both applicable for a fully or partially penetrating test well, and neglect any aquifer storage (flow to the well is quasi-steady state). The Bouwer and Rice method also assumes that drawdown at the well is negligible, flow above the water table can be ignored, and well losses are negligible. The equations used for the Hvorselv and Bouwer and Rice methods are shown in Appendix A.

2.3.4 Aquifer Tests

Although slug tests are simple and relatively reliable, the results are sensitive to conditions immediately surrounding the piezometer and are generally considered less reliable than aquifer pumping tests [*Kruseman et al.*, 1994]. During an aquifer test, the water level is lowered by pumping water out at a constant rate (Figure 2.3). The removal of water causes the water level to lower. This response, which depends on the hydraulic properties of the aquifer, is measured in the pumping well and/or an observation well some distance away (1-5 m). Aquifer pumping tests are more complex to conduct (they require multiple boreholes and more equipment) and take longer to conduct than slug

tests, but they provide insight into the hydraulic conductivity over a larger volume of the aquifer.

Aquifer tests were conducted at two sites 7 km apart (FA16_4, upstream, and FA16_6, downstream). To conduct aquifer tests within the firn aquifer, 8 cm diameter boreholes formed from ice core drilling and widened with a heater reamer were used as fully penetrating pumping wells and piezometers were installed and removed to create observation wells. Water was pumped from the borehole at a constant rate (0.0011 m^3/s at FA16_4 and 0.0012 m^3/s at FA16_6) and discharged ~30 m downslope. The water level change was measured with pressure transducers lowered down the pumping and observation wells. Pressure was measured at 1 minute intervals, and at 1 second intervals for some of the periods around the time the pump was turned off. The higher frequency was employed to capture water level during times of rapid change in water level.

At FA16_4 the water level was monitored in the pumping well and in one fully penetrating observation well 1m away. At FA16_6 the water level was monitored in the pumping well and in two observation wells 2 m (fully penetrating) and 5 m (partially penetrating, depth to screen is 0 cm, screen length is 460 cm) away. Drawdown from pumping forms a cone of water level depression surrounding the pumping well. The shape of this cone depends on the storage and transmissive properties of the aquifer. A more permeable aquifer will develop a narrower, shallower cone of depression than a less permeable aquifer. The observation wells were placed close to the pumping wells to capture drawdown in a highly permeable material.

The Theis theoretical response curves for unconfined aquifers were compared to observed water level changes to estimate aquifer transmissivity and storativity [*Theis*, 1935]. The Theis solution of aquifer parameters for the drawdown distribution

surrounding a well at any time is shown in Appendix A.

Prior to curve fitting, the drawdown data were adjusted according to Equation 2.3 because the Theis solution was originally developed for confined aquifers where the saturated thickness remains constant with pumping. The saturated thickness of an unconfined aquifer changes due to pumping. The adjusted drawdown, which accounts for changing saturated thickness, is calculated as:

$$s' = s - s\,2/2\,b \tag{2.3}$$

where *s'* is the corrected displacement (length), *s* is the observed displacement, and *b* is the saturated aquifer thickness (length) [*Jacob*, 1944; *Kruseman et al.*, 1994]. The aquifer thickness was obtained from ground penetrating radar, seismic investigations [*Montgomery et al.*, 2017], water level measurements, and borehole dilution tests [*Freeze and Cherry*, 1979]. The observed displacements were small (less than 2 m), causing this correction to be minimal.

Hydraulic conductivity (*K*), can then be calculated as:

$$K = \frac{T}{b} \tag{2.4}$$

where *T* is transmissivity (length^2/time). The Theis solution assumes that the aquifer has an infinite aerial extent and is homogeneous, isotropic, and of uniform thickness. The diameter of the pumping well must be relatively small so that storage in the pumping well is assumed to be negligible. The pumping well can be fully or partially penetrating.

Further, the method assumes that flow to the pumping well is horizontal when the pumping well is fully penetrating, and there is no delayed response to gravity within the aquifer.

2.3.5 Hydraulic Conductivity Estimation

Solutions of aquifer parameters to the Bouwer-Rice, Hvorselv, and Theis equations can be obtained through a curve matching method. The publicly available program AQTESOLV, by HydroSOLVE, Inc. © [*Duffield*], was used to estimate hydraulic conductivity from slug and aquifer test data. AQTESOLV has both automatic and visual curve matching options. The automatic curve matching option uses a nonlinear least squares method to match theoretical to observed data by minimizing the sum of squared residuals. The visual curve matching option allows the user to manually match solutions to the observed data. The automatic curve matching was applied, and visually checked to ensure a match between observed slug test data and test solution line within the recommended normalized head ranges (0.15-0.25 for Hvorslev method and 0.2-0.3 for Bouwer and Rice method) [*Butler,* 1996].

The water level rose several centimeters over the course of the longer duration aquifer tests (~hours), likely due to aquifer recharge from surface melt. A linear relationship between water level and time was used to calculate the water level change at a given time due to recharge. This additional water level rise was removed from the water level data prior to input into AQTESOLV in order to isolate the water level change effects (lowering water level) induced by pumping from those due to recharge (rising water level).

The correction to apply the Theis solution for a confined aquifer to data from an

unconfined aquifer is automatically applied to drawdown data by AQTESOLV. However, to analyze the recovery data, the correction was manually applied and the residual recovery Theis solution for a confined aquifer was used.

2.4 Results

2.4.1 Slug Tests

Several types of water level response curves to the slug test were noted (Figure 2.4). Generally, the early time response, within the recommended normalized head ranges, fits the Hvorslev and Bouwer and Rice solutions well. A few tests mostly followed the response predicted by the Hvorslev method (1%) (Figure 2.4, panel **A**). The oscillatory (Figure 2.4, panel **B**), water level response to the slug test, which reflects the high permeability of the firn [*Bredehoeft et al.*, 1966; *Van der Kamp*, 1976], occurred in 25% of responses. For some tests (65%), the later time water levels recovered more quickly than predicted (Figure 2.4, panel **C**), and for other tests (10%), the late time water levels took longer to recover than predicted (Figure 2.4, panel **D**). The concave up response (Figure 2.4, panel **D**) is often observed in confined and unconfined aquifers, and is likely due to a storage parameter of the aquifer and the piezometer [*Butler*, 1996]. This could look like the double straight line effect, which has been observed when the well is screened across the water table [*Bouwer*, 1989]. However, the screened interval of the piezometer was always below the water table and so we do not think this contributes to the poor fit. About 8% of responses showed a quicker than predicted and oscillatory response. Individual sites tend to have dominant response types, but can have a variety of responses. The dominant response type does not correspond to site location or slope of the water table. Overall, we found good fits within the recommended normalized head

ranges.

Initial water level displacements within the piezometer ranged from 0.3-6 m. Despite initial displacements up to 6 m for some slug tests, the Reynolds number is still within the laminar flow range. For this analysis, we assumed that K_z/K_r was 1. A sensitivity analysis showed that decreasing ratio of K_z/K_r from 1 to .01 changed the hydraulic conductivity of one slug test from 1.6 $x10^{-4}$ m/s to 2.7 $x10^{-4}$ m/s, which is within the range of variation observed between repeat tests.

Hydraulic conductivity within the firn aquifer was estimated from slug tests using two analysis methods (Appendix B, Table B1). Hydraulic conductivity estimated using the Hvorslev method ranges from $1.1x10^{-3}$ to $2.5x10^{-5}$ m/s, with a geometric mean of $2.8x10^{-4}$ m/s and geometric standard deviation of 1.6. Hydraulic conductivity estimated using the Bouwer and Rice method ranges from $8.8x10^{-4}$ to $2.4x10^{-5}$ m/s, with a geometric mean of $2.5x10^{-4}$ m/s and geometric standard deviation of 1.7 (Table 2.3). The geometric mean is reported because hydraulic conductivity tends to be log normally distributed [*Neuman*, 1982]. The Hvorselv method yields a larger range in hydraulic conductivity estimates ($1.1x10^{-3}$ m/s) than the Bouwer and Rice method ($8.5x10^{-4}$ m/s). The effective radius over which the water level change occurred ranges from 0.16 m for a test at 12 m depth to 1.18 m for a test at 38 m.

Hydraulic conductivity varies slightly between sites. The hydraulic conductivity decreases slightly with depth through the firn aquifer, although the relationship is weak ($r^2 = 0.17$) (Figure 2.5). The greatest decrease with depth occurs at FA16_4. Ice layer stratigraphy does not seem to dramatically influence hydraulic conductivity within the aquifer. This is likely because the horizontal flow induced by the slug test is controlled by the firn with the highest hydraulic conductivity within the screened interval of the

piezometer. Further, ice layers can be permeable [*Keegan et al.*, 2014]. *Humphrey et al.* [2012] describe meltwater bypassing ice layers in the percolation zone, a more similar setting to our work than *Keegan et al.* [2014]. Still the general decrease in hydraulic conductivity can be attributed to a gradual increase in density with depth, indicating an increase in ice, which may be more uniformly distributed as opposed to distributed in layers. This is addressed in further detail in Section 2.5, Discussion.

The Hvorslev method and Bouwer and Rice methods for estimating hydraulic conductivity yield similar results (Figure 2.6). The linear fit between the estimates from both methods ($y = 0.84x + 2x10^{-5}$ m/s) indicates that the Bouwer and Rice method predicts hydraulic conductivity estimates that are roughly 20% lower than the Hvorslev method. This is consistent with the findings described in *Butler* [1996] of *Hyder et al.* [1994] and *Hyder and Butler* [1995] in terrestrial groundwater systems. The average percent difference between estimates is 8%. The Bouwer and Rice method has been found to underestimate hydraulic conductivity, and yield superior estimates relative to the Hvorslev method [*Brown et al.*, 1995]. The largest uncertainty in the hydraulic conductivity estimates from slug tests is that both the Hvorselv and Bouwer and Rice methods ignore the storage properties (specific storage) of the aquifer, which can contribute to uncertainties of over 60% [*Brown et al.*, 1995]. However, the difference between the estimates from both methods in this study is ~20%, smaller than the uncertainty from ignoring storage. The mean hydraulic conductivity estimated using both methods is not statistically different, as indicated by a t-test (at $p = 0.05$). The similarity to each other and to the aquifer test results, described below, indicates that both methods seem to represent the firn aquifer well.

2.4.2 Aquifer Tests

Aquifer test drawdown and recovery over time, and predicted displacements for a range of hydraulic conductivities are shown in Figure 2.7. The comparisons between observed drawdown and recovery data to theoretical curves predicted by the Theis solution are shown in Figure 2.8. The hydraulic conductivity estimated from all aquifer tests ranges from $3.7x10^{-4}$ to $2.8x10^{-5}$ m/s, with a geometric mean of $1.8x10^{-4}$ m/s and geometric standard deviation of 1.6 (Tables 2.3, 2.4). Changing the ratio of K_z/K_r does not affect hydraulic conductivity estimates. The observed drawdown is close to the predicted drawdown for a hypothetical aquifer test in a 15 m thick aquifer with hydraulic conductivity of $2x10^{-4}$ m/s, a pumping rate of 0.001 m^3/s and a radial distance of 1 m between the pumping and observation well (Figure 2.7). Increasing or decreasing the hydraulic conductivity by an order of magnitude results in much larger or smaller displacements than what we observed.

The fit between observed and theoretical drawdown for some tests varies. A generally poor fit to early time data probably results from wellbore storage of water and transience in the pumping rate at very early times. The pump gradually increases the pumping rate over the first minute, which violates the constant pumping rate assumption. Wellbore storage serves as the primary source of pumped water at early times, but as pumping continues, wellbore storage decreases and the aquifer becomes the primary source of pumped water. Therefore, many of the early time data (~min) were discarded. The pumping well at site FA16_4 experienced drawdown below the pressure transducer, causing a loss of data. These data were excluded from hydraulic conductivity estimates. Further, the observation well at site FA16_4 is located only 1 m from the pumping well, and may have been subject to turbulent flow effects caused by pumping as observed in

the significantly greater drawdown at this site compared to FA16_6 and the difference between the hydraulic conductivity estimates during the drawdown and recovery periods. Increased and turbulent flow causes head loss in the borehole [*Jacob*, 1947], which would lead to an underestimation of hydraulic conductivity during the drawdown period. Excluding data influenced by turbulent flow (excluding data from FA16_4 pumping well, and observation well during the drawdown period) results in a range of hydraulic conductivity between $3.7x10^{-4}$ m/s and $1.4x10^{-4}$ m/s, with a geometric mean of $2.3x10^{-4}$ m/s and geometric standard deviation of 1.4.

The displacement data from the recovery period were not influenced by turbulent effects as the pump is not used during this period. Therefore, the recovery data likely result in a more accurate estimate with a range between $3.7x10^{-4}$ m/s and $1.4x10^{-4}$ m/s, with a geometric mean of $2.4x10^{-4}$ m/s and geometric standard deviation of 1.4.

The distance between the pumping and observation wells was measured at the surface, and if the boreholes deviated from vertical, then the true distance between the boreholes may vary. A sensitivity analysis comparing the hydraulic conductivity estimated from the observation well at site FA16_4 showed that increasing the distance between the wells from 1m to 20 m had no effect on the hydraulic conductivity estimate. This is likely because in a highly permeable system, the cone of depression is wide and shallow, and therefore insensitive to the distance between the wells.

The geometric mean of hydraulic conductivity estimated using both slug tests (Hvorselv method) and aquifer tests (only recovery period) is $2.7x10^{-4}$ m/s with a geometric standard deviation of 1.4. The hydraulic conductivity decreases most with depth at site FA16_4, shown in the slug test results. The aquifer test at this site indicates that the hydraulic conductivity at this site is roughly the average of the depth-specific

slug test measurements.

2.5 Discussion

To our knowledge, these are the first hydraulic conductivity measurements of a firn aquifer in the southeastern Greenland ice sheet and these are the first depth specific slug tests conducted in a firn aquifer. We find relatively homogeneous hydraulic conductivity between measurement sites, and a slight decrease with depth. While ice layers within the firn aquifer may reduce vertical hydraulic conductivity, we did not test for this. Ice layers do not appear to dramatically reduce horizontal hydraulic conductivity and thus horizontal flow. Any horizontal fluid flow within the aquifer and discharge into the englacial hydrologic system is controlled by the horizontal firn layers with the highest hydraulic conductivity. Quantifying hydraulic conductivity and its spatial variation is a crucial step in developing realistic hydrologic models of the aquifer systems, and for understanding the impact the firn aquifer has on ice sheet mass balance. The observed spatial and vertical homogeneity should reduce firn aquifer hydraulic modeling complexity.

The largest uncertainties in the hydraulic conductivity estimates from slug tests result from ignoring the storage properties of the aquifer, and possible leakage around the packer. This could contribute to the weak vertical gradient in hydraulic conductivity. However, water level differences were observed as the packer was inflated, suggesting that the seal was strong enough to counter the hydraulic gradient. The largest uncertainties in the hydraulic conductivity estimates from the aquifer tests likely result from turbulent effects in this highly permeable system. The high permeability of the aquifer meant that the observation wells had to be placed close to the pumping well in

order to observe any measurable drawdown. However, this also resulted in some turbulent effects in the water level data (much lower hydraulic head than predicted), leading to a poor fit to theoretical solutions, particularly in the pumping well. This was addressed by discarding data where these effects were obvious, and by fitting the theoretical curves to the later time data and the recovery period data.

Although the very early time recovery data (~seconds) may be subject to turbulent effects, most of them are not. The recovery data, particularly in the observation wells, are also not subject to influences by well construction. These data depend solely on aquifer parameters. The recovery data are also not subject to any turbulent effects from pumping and are therefore the more reliable data and provide the most reliable estimate of hydraulic conductivity. Further, the general agreement with the hydraulic conductivity estimates from multiple sites and methods suggests that the hydraulic conductivity of the system is generally well represented. The agreement between the slug tests and the aquifer tests, which perturb a larger volume of the aquifer (over 10 m diameter), suggests that meltwater from the installation of the piezometer or drilling of the borehole does not seem to impact the hydraulic conductivity estimates. Numerical modeling combined with an independent measurement of fluid flow, can better constrain hydraulic conductivity. In the absence of an independent measurement of flow, the in situ measurements described in this manuscript represent the best estimates of hydraulic conductivity. The overall range of hydraulic conductivity values seems to capture the uncertainty.

The porosity and permeability of the firn could be altered by the melting caused by the heated piezometer or the heated thermoelectric drill. This would particularly bias the slug test results towards a higher hydraulic conductivity because they perturb a relatively smaller volume of the aquifer. However, the aquifer test results, which perturb

a much larger volume of the aquifer (> 10 m diameter), are less subject to significant alteration from melting and provide a good comparison to, and generally agree with, the slug test results. The agreement between multiple complementary methods (slug tests and aquifer tests during pumping and recovery periods in particular) suggests that the hydraulic conductivity estimates are robust.

No seasonal changes were observed in hydraulic conductivity. However, only one site was tested in the spring, prior to surface melt onset. The other five sites were tested in the summer. Still, we do not expect substantial changes to hydraulic conductivity within the saturated zone because the temperature within the saturated zone remains at 0ºC throughout the year. Thus, we do not expect significant freezing or thawing to occur within the saturated zone, which could alter the hydraulic conductivity by reducing or enhancing pore connectivity. However, longer time monitoring in different seasons would be required to identify seasonal impacts.

Our measurements of the hydraulic conductivity of the firn aquifer in southeast Greenland overlap with estimates for a firn aquifer in the Holtedahlfonna ice field, Svalbard, between 3.2×10^{-5} and 1.8×10^{-4} m/s [*Christianson et al.*, 2015]. The hydraulic conductivities measured in southeast Greenland, however, are approximately an order of magnitude higher than those taken from firn aquifers in various mountain glaciers where hydraulic conductivities show a relatively narrow range from 1.2×10^{-5} to 5×10^{-5} m/s, [*Oerter and Moser*, 1982; *Oerter et al.*, 1983; *Fountain*, 1989; *Fountain and Walder*, 1998; *Schneider*, 1999; *Jansson et al.*, 2003]. Hydraulic conductivity depends on the properties of the porous media (e.g., grain size, shape, or packing) and the fluid flowing through the porous media. *Christianson et al.* [2015] hypothesized that aquifers at deeper locations within an ice sheet/ glacier will have decreased conductivities as firn densifies

and pore space decreases. While this hypothesis may generally hold for a firn column in a single location, the growing number of spatially distributed hydraulic conductivity measurements of firn show variations across glaciers and ice sheets. This is expected as firn stratigraphy and microstructure vary across climates.

We can also compare permeability, which is only a function of the porous media, to sites where no aquifer exists. Permeability increases from mountain glaciers (~10^{-12} m^2) to the southeast Greenland firn aquifer (~10^{-12} – 10^{-10} m^2) to dry firn (~10^{-10} m^2) [*Oerter and Moser*, 1982; *Oerter et al.*, 1983; *Fountain*, 1989; *Fountain and Walder*, 1998; *Schneider*, 1999; *Albert et al.*, 2000; *Luciano and Albert*, 2002; *Adolph and Albert*, 2014; *Keegan et al.*, 2014]. We attribute the difference in permeability across regions to the ice content represented in density profiles of the different locations where average density decreases from mountain glaciers to southeast Greenland firn aquifer to dry firn [*Fountain*, 1989; *Adolph and Albert*, 2014; *Koenig et al.*, 2014]. Although *Keegan et al.* [2014] and *Adolph and Albert* [2014], and *Albert et al.* [2000] report vertical permeability, *Keegan et al.* [2014] note that differences between lateral and vertical permeability are smaller than differences between vertical permeability of different layers [see *Luciano and Albert*, 2002] and are therefore adequate for a general comparison. Also, the horizontal and vertical permeability are within the same order of magnitude. The density profiles recorded at measurement sites offer an initial explanation, as follows, for the changes in permeability; however, detailed microstructure measurements are needed, specifically to resolve pore interconnectivity and orientation, to more fully describe permeability differences.

The differences in ice content, and therefore densities, between mountain glaciers and the southeast Greenland firn aquifer are in part due to the long-term (decades),

perennial nature of the aquifer in southeast Greenland. Aquifers in mountain glaciers are generally smaller, thinner, and steeper, allowing for annual drainage and more refreeze when air temperatures dip below 0ºC in the winter [*Vallon et al.*, 1976; *Oerter et al.*, 1983; *Fountain*, 1989, 1996; *Jansson et al.*, 2003]. The perennial aquifer in southeast Greenland is in general deeper (10's of m) and thicker (10's of m), which limits refreezing in the saturated zone (Table 2.2). This increased annual refreezing in mountain glaciers likely leads to more ice and reduced pore connectivity.

The differences in ice content between dry firn and the southeast Greenland firn aquifer are due to climatic and geographic differences [*Kuipers Munneke et al.*, 2014]. The dry-firn sites experience little to none of the surface melt and subsequent freezing that occurs at our site, in the percolation zone of southeast Greenland. Therefore, the dry-firn sites do not accumulate as much refrozen ice, leading to more permeable firn. The lateral homogeneity of hydraulic conductivity observed in the Greenland firn aquifer has also been observed in South Cascade Glacier [*Fountain*, 1989]. This similarity likely reflects the homogenizing effect of saturating firn at 0ºC on firn microstructure. While the ice layer stratigraphy at a specific location doesn't seem to dramatically influence the horizontal hydraulic conductivity, as shown in our measurements and noted by *Keegan et al.* [2014], increases in overall ice content of the firn column do seem to reduce hydraulic conductivity and permeability (e.g., from mountain glaciers to water saturated firn to dry firn).

This study provides estimates on hydraulic parameters for a newly discovered firn aquifer and proves the effectiveness of the heated piezometer, particularly as a light weight (~200 kg), fast method to access an aquifer from the snow surface for in situ physical measurements and water sampling. The heated piezometer is a unique tool

developed to study firn hydrology in Greenland, but can be used in any firn aquifer setting. The hydraulic conductivities measured can be used to improve models of water flow within, and discharge from, firn aquifers and further constrain the storage and retention time estimates for aquifers within the Greenland ice sheet. As melt is projected to increase under a predicted warmer climate, the firn aquifer could have an increasingly important effect on Greenland ice sheet mass balance by efficiently transporting meltwater through firn to the ocean.

Table 2.1. Site locations. Description of sites where boreholes were drilled, piezometers were installed, and hydraulic testing was conducted.

Site Name	Latitude (°)	Longitude (°)	Elevation (m)	Tests conducted and field season
FA15_1	66.362	-39.312	1664	Slug tests, April 2015
FA15_2	66.355	-39.179	1543	Slug tests, July 2015
FA15_3	66.355	-39.190	1553	Slug tests, August 2015
FA16_4	66.360	-39.287	1648	Slug tests and aquifer tests, July 2016
FA16_5	66.358	-39.239	1619	Slug tests, July 2016
FA16_6	66.353	-39.135	1519	Slug tests and aquifer tests, August 2016

Table 2.2. Aquifer geometry. Depth to water table and aquifer bottom, and aquifer thickness measurements from in situ and geophysical methods. *Seismic line names are from *Montgomery et al.* [2017].

Site Name	FA15_1	FA15_2	FA15_3	FA16_4	FA16_5	FA16_6
Name of nearest seismic line*	6a	10d	10a	7	8a	12a
Water table depth from chalked steel tape (m)	19.9	14.6	20.8	20.1	22.5	10.0
Bottom of aquifer depth from borehole dilution (m)				33.25	30.15	47.78
Aquifer thickness from in situ measurements(m)				13.2	7.7	37.8
Radar water table depth (m)	18.4	14.4	19.7	18.9	19.3	10.7
Seismic bottom (m)	32.2	35.0	25.7	27.1	28.0	30.8
Minimum bottom depth (m)	29.9	29.0	24.7	25.7	25.2	27.5
Maximum bottom depth (m)	35.5	42.0	28.5	30.8	30.3	33.6
Seismic thickness (m)	13.8	20.6	6	8.2	8.7	20.1
Minimum thickness (m)	11.5	14.6	5.1	6.8	5.9	16.8
Maximum thickness (m)	17.1	27.6	8.8	11.9	11.0	22.9
Thickness used for hydraulic conductivity estimate (m)	13.8, 17.1	20.6, 27.6	6, 8.8, 11.06	13.2	7.7, 11	37.8

Table 2.3. Hydraulic conductivity results. Summary of geometric mean and standard deviations of slug tests and aquifer tests analyzed using different methods, excluding turbulent flow, and focusing on the recovery period of the aquifer tests.

Test			Hydraulic conductivity geometric mean (m/s)	Geometric standard deviation
Slug tests		Hvorselv method	2.8E-04	1.6
		Bouwer and Rice method	2.5E-04	1.7
Aquifer tests		All results	1.8E-04	2.1
		Turbulent flow excluded	2.3E-04	1.4
		Recovery period only	2.4E-04	1.4
Slug tests and aquifer tests together	Hvorselv method	All results	2.6E-04	1.7
		Turbulent flow excluded	2.7E-04	1.6
		Recovery period only	2.7E-04	1.6
	Bouwer and Rice method	All results	2.4E-04	1.7
		Turbulent flow excluded	2.5E-04	1.6
		Recovery period only	2.5E-04	1.6

Table2.4. Aquifer test results. Hydraulic conductivity estimates from aquifer tests during drawdown and recovery periods in each well. Asterisk indicates estimates likely subject to turbulent flow effects caused by pumping.

		Hydraulic conductivity (m/s)			
		Drawdown		Recovery	
Site	**Well**	**Test 1**	**Test 2**	**Test 1**	**Test 2**
FA16_4	Observation	3.1E-05*	2.8E-05*	1.4E-04	1.4E-04
FA16_6	Pumping	1.6E-04	1.6E-04	3.5E-04	2.4E-04
FA16_6	Observation 1	1.6E-04	2.5E-04	3.6E-04	1.9E-04
FA16_6	Observation 2	3.2E-04	3.1E-04	3.7E-04	2.3E-04

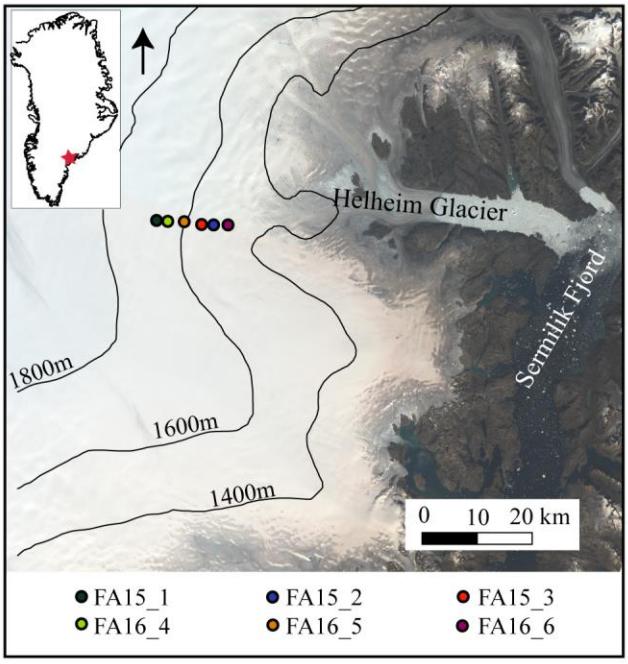

Figure 2.1. Site map. Landsat 8 composite image (August 21, 2014) showing sites in southeast Greenland where slug tests and aquifer tests were conducted in April, July, and August 2015 and July and August, 2016. Elevation contours from Cryosat-2 DEM [*Helm et al.*, 2014].

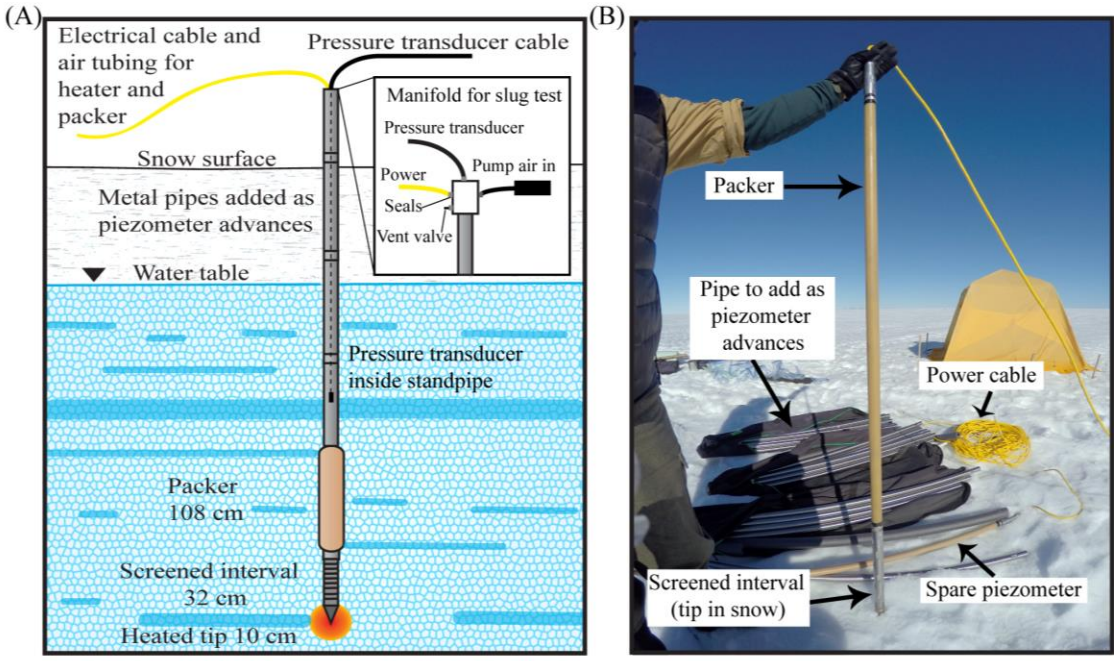

Figure 2.2. The heated piezometer. Diagram (A) and photo (B) of the heated piezometer. The piezometer, consisting of a sealed pipe above an inflatable packer, screened interval, and heated tip at depth, advances to greater depth as the heated tip melts through the firn and ice lenses. Lengths of threaded pipe can be added at the surface as the tip moves downward. A power cable and hollow tube run the length of the pipe to power the heater and allow for packer inflation from the surface. Tubing can be lowered into the piezometer to collect water samples. The screened interval allows for hydraulic testing and water sampling from the entire thickness of firn/ice that the screened interval is open to.

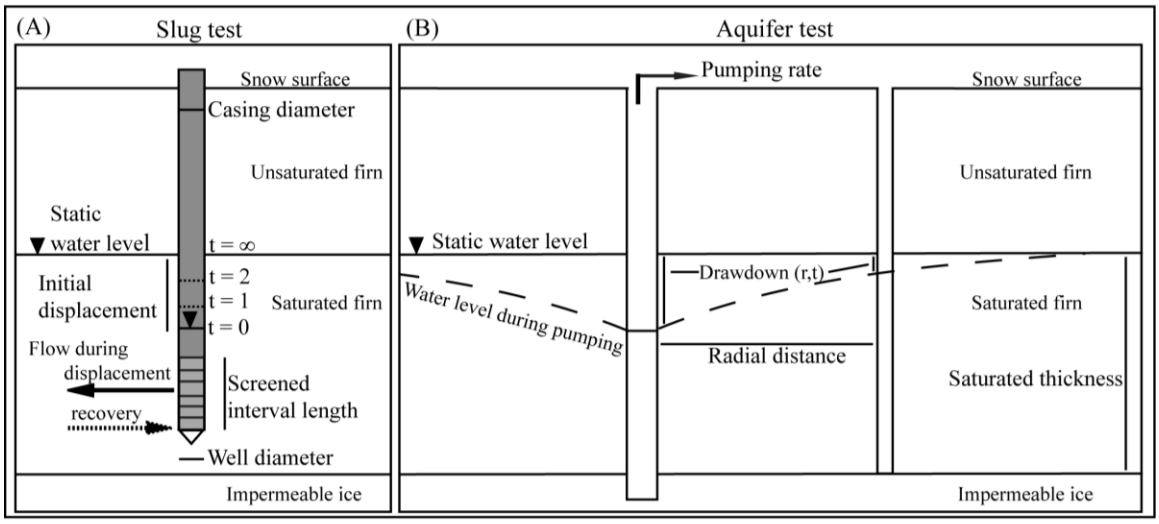

Figure 2.3. Diagrams of slug and aquifer tests. Diagrams showing the aquifer and well geometries for slug (A) and aquifer (B) tests used in analysis of slug and aquifer tests.

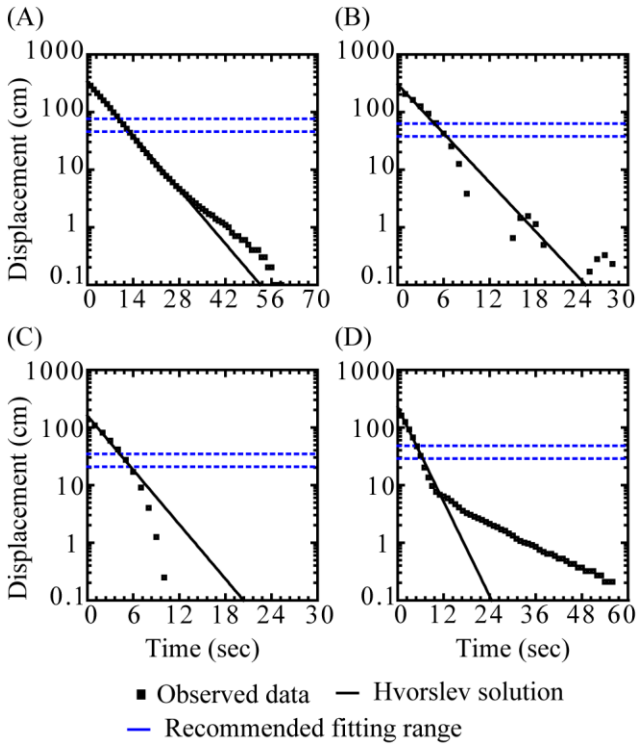

Figure 2.4. Slug test curve fitting. Water level responses over time (squares), Hvorslev solution (lines) for representative slug tests, and recommended fitting range (blue dashed lines). Water levels generally match the predicted recovery (A), recover rapidly, and sometimes oscillate slightly (B), recover more quickly than predicted (C), or recover more slowly than predicted (D).

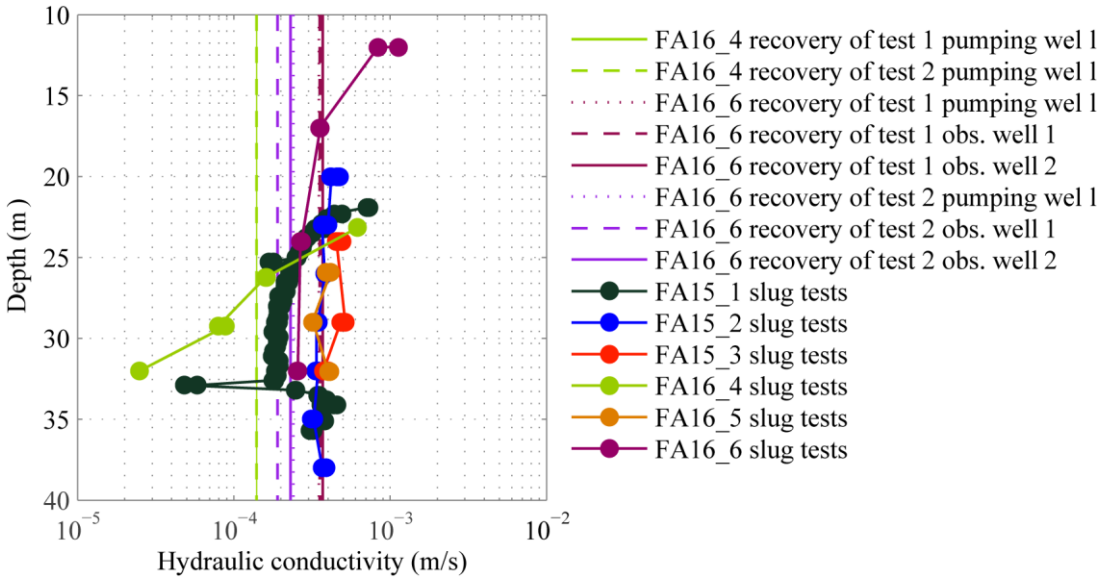

Figure 2.5. Hydraulic conductivity across ~10 km and between ~10-40 m depth. Hydraulic conductivity estimates determined using the Hvorselv method for slug test data and the Theis method for aquifer test data. The slug test measurements were taken at specific depths while the aquifer test data are not depth-specific. Water level rise due to recharge during the aquifer tests has been removed, as have data from the pumping well at site FA16_4 (see section 3.2). Data points are larger than standard error of estimate.

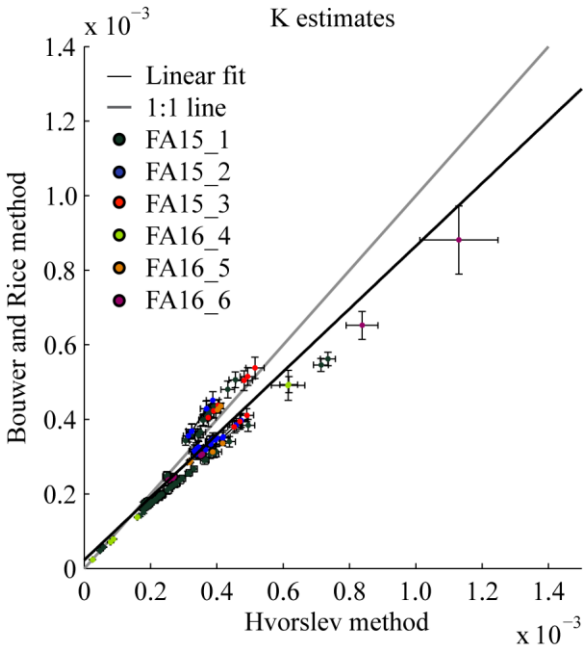

Figure 2.6. Comparison of hydraulic conductivity estimates by method. Graph comparing the hydraulic conductivity estimated using Hvorslev's method and Bouwer and Rice's method for each site. Error bars represent standard error of the hydraulic conductivity estimates. A linear fit of these estimates (black line) has a slope of 0.84, intercept of $2x10^{-5}$, and an r^2 of 0.89 (r = 0.94). The grey line indicates a 1:1 fit.

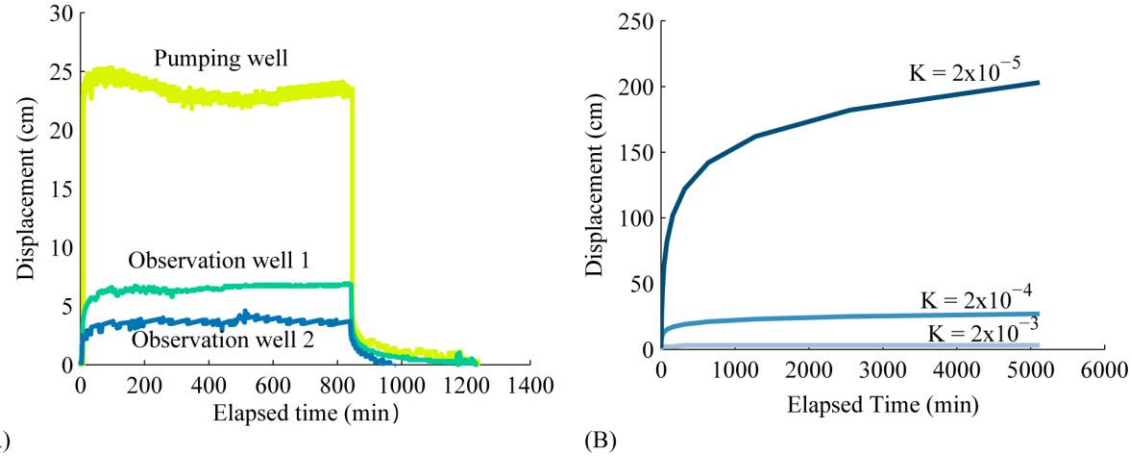

Figure 2.7. Observed and theoretical drawdown. Displacement over time at site FA16_6 in the pumping and observation wells during the first test (A) and predicted drawdown in an observation well for a hypothetical aquifer test with varying hydraulic conductivity (B). For this scenario, the aquifer is 15 m thick, the pumping rate is 0.0011 m^3/s, the storativity is 0.2, and the distance between the pumping and observation well is 1m. The predicted drawdown when hydraulic conductivity is $2x10^{-4}$ m/s is most similar to the drawdown we observed.

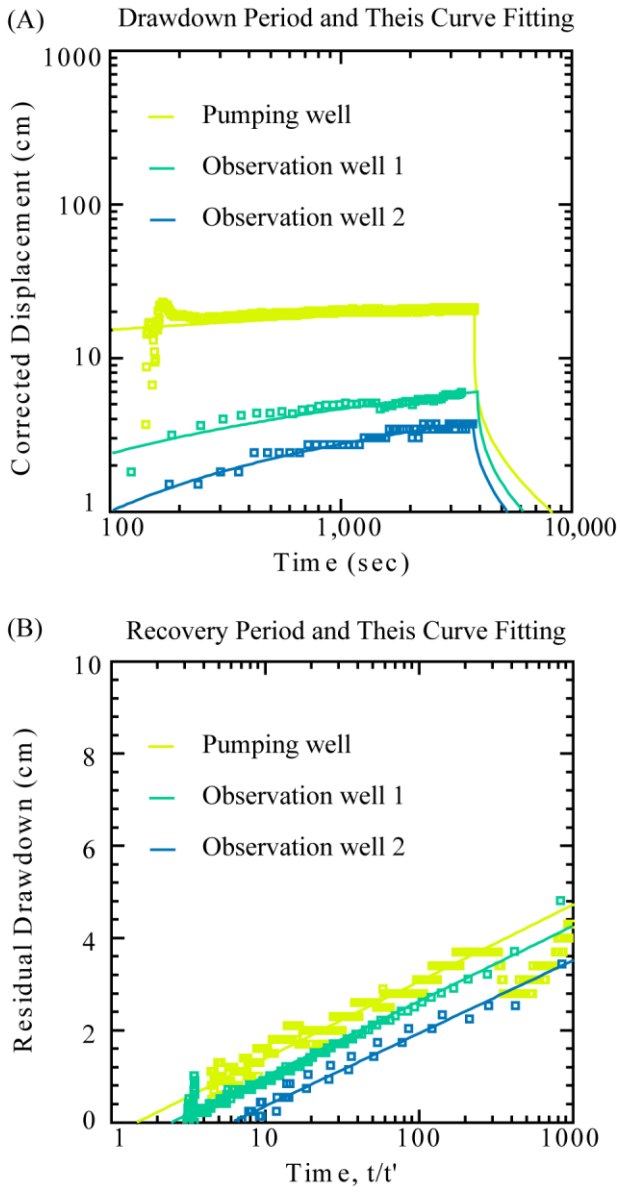

Figure 2.8. Aquifer curve fitting. (A) Recharge-corrected drawdown over time and Theis solution curves in the pumping and two observation wells during the second aquifer test at FA16_6. The squares represent water level displacement from the water level prior to pumping in different wells. The lines represent the Theis solution to the drawdown data. (B) Residual drawdown versus time elapsed since the start of pumping relative to the time since pumping stopped (t/t') and the Theis solution curves for aquifer test 1 at FA16_6 and FA16_6 The squares represent water level measurements after pumping stops and the lines represent the Theis solution to the recovery data.

CHAPTER 3

DIRECT EVIDENCE OF MELTWATER FLOW WITHIN THE SOUTHEASTERN GREENLAND ICE SHEET FIRN AQUIFER

3.1 Abstract

The Greenland ice sheet is losing mass due to surface meltwater runoff and ice discharge, with important implications for sea level rise [*Shepherd et al.*, 2012]. Surface mass balance processes are expected to control the ice sheet's increasing contribution to sea level rise in the future [*Enderlin et al.*, 2014]. In some areas of the Greenland ice sheet, liquid meltwater has accumulated within firn pore space, forming an extensive firn aquifer system [*Forster et al.*, 2014; *Koenig et al.*, 2014]. Previously it was unclear if the aquifer impeded or facilitated meltwater runoff by either retaining meltwater in pore space or allowing fluid flow to occur within the aquifer. Following injection and mixing of a saline solution into boreholes within the firn aquifer in southeastern Greenland, specific conductance measurements decreased over time as flowing freshwater diluted the saline mixture in the borehole. These borehole dilution tests indicate that meltwater flows through the aquifer with an average specific discharge of 4.3×10^{-6} m/s ($\sigma = 2.5 \times 10^{-6}$ m/s). The specific discharge drops dramatically to 0 m/s, defining the bottom of the aquifer between ~30 to ~50 m depth. Small changes in specific discharge are observed between boreholes and specific discharge generally decreases with depth. The observed flow indicates that the firn pore space is not a long-term storage mechanism in this region.

Instead, meltwater is flowing out of the aquifer, likely into crevasses at the edge of the ice sheet. Specific conductance measurements made prior to saline solution injection correlate with clear ice thickness measured in firn cores, suggesting that natural specific conductance increases over time as dissolved solids are continually supplied from surface deposition and meltwater transport to depth and ion exclusion during clear ice formation and burial. We hypothesize that the longer the aquifer exists at a site and the clear ice formation process occurs, the greater the ion concentration in liquid water will be. Thus, the salinity of the water constrains the timing of aquifer formation. Preliminary mass balance calculations suggest that the aquifer formed no earlier than the late 1980s and therefore is the result of recent global climate change and the associated warming of the Arctic.

3.2 Introduction

Greenland hosts the second largest ice mass in the world after Antarctica. The Greenland ice sheet has experienced warming of ~0.5 ºC/decade [*Hall et al.*, 2013]. Understanding ice melt in polar regions, including Greenland, is critical to understanding how sea levels will change in response to climate change. Between 1992 and 2011, the Greenland ice sheet (GrIS) lost ~2700 ± 930 Gt of ice [*Shepherd et al.*, 2012]. The Greenland ice sheet mass loss is accelerating [*Vaughan et al.*, 2013]. Mass loss results from surface meltwater runoff and ice discharge to the ocean, with surface mass balance processes becoming increasingly dominant [*Enderlin et al.*, 2014]. Surface melt extent area has increased since the late 1950s [*Fettweis et al.*, 2011], with an extreme melt event in 2012 melting over 90% of the ice sheet surface [*Nghiem*, 2012; *Tedesco*, 2013]. While meltwater from the Greenland ice sheet contributes to sea level rise, how and when

surface meltwater reaches the ocean is poorly constrained [*Tedesco*, 2013].

Meltwater transport within the percolation zone, where much of the increased surface melt occurs, is also poorly understood. Longer term meltwater storage can occur when infiltrated meltwater freezes at depth within cold firn, thereby buffering sea level rise [*Pfeffer*, 1991; *Parry et al.*, 2007; *Harper et al.*, 2012]. Modeling studies show that ~45% of meltwater refreezes [*Ettema et al.*, 2009]. However, the evolution of the firn capacity varies spatially and temporally [*van Angelen et al.*, 2013; *de la Peña et al.*, 2015; *Lindbäck et al.*, 2015; *Machguth et al.*, 2016]. Meltwater discharge can occur when meltwater flows through the glacial hydrologic system and can contribute to sea level rise [*Lewis and Smith*, 2009; *Chu*, 2014; *Smith et al.*, 2015]. This process can occur over shorter (daily - seasonal) or longer time scales (annually, as described in this manuscript).

An extensive firn aquifer system exists within the GrIS. Surface snowmelt infiltrates into the upper layers of the ice sheet and fills available pore space above the firn-ice transition, thus forming a large unconfined aquifer that persists throughout the year [*Forster et al.*, 2014; *Koenig et al.*, 2014]. Firn aquifers form where accumulation and melt rates are high [*Miège et al.*, 2013; *Kuipers Munneke et al.*, 2014]. The high accumulation provides pore space and insulation for the liquid water to persist through cold winters. The aquifer covers between 22,000 – 90,000 km^2 and, if released into the ocean, would contribute about 0.4 mm of sea level rise globally [*Forster et al.*, 2014; *Koenig et al.*, 2014; *Miège et al.*, 2016; *Steger et al.*, 2017].

The effect the firn aquifer has on meltwater runoff has been unclear. Two end-member hypotheses representing pathways for the stored meltwater to exit the aquifer motivate this research: 1) the aquifer drains constantly to the base of the ice sheet through a connected englacial hydrologic network including crevasses and moulins, or 2) the

aquifer stores water in pore space until all available pore space is filled and/or a threshold is met, leading to a catastrophic release [*Koenig et al.*, 2014]. The firn storage capacity across the percolation zone of the Greenland ice sheet has been estimated between ~300-1,200 Gt [*Harper et al.*, 2012]. At our study site, the firn capacity is already half filled [*Koenig et al.*, 2014].

Theoretically, meltwater within the firn aquifer should flow if a connected network of pores exists. Darcy's law indicates that the hydraulic conductivity and the hydraulic gradient within an aquifer control the specific discharge. Field observations of highly permeable firn and a sloping water table suggest that the meltwater should flow within the aquifer. Horizontal fluid flow within the aquifer accompanied by the observed undulating water table [*Forster et al.*, 2014] favors the first hypothesis. If meltwater flows through the aquifer, it must be discharging from the aquifer, possibly flowing to the ocean via crevasse drainage at the edge of the ice sheet. Thus, characterizing water flow within the aquifer is critical to determining whether the aquifer is storing meltwater or allowing it to leave the ice sheet.

The effect the firn aquifer may have on ice sheet dynamics is also unclear. Meltwater drainage through crevasses or moulins to the base of the ice sheet could enhance basal melt [*Parizek and Alley*, 2004] and basal sliding and increase ice velocity and discharge to the ocean [*Zwally*, 2002; *Alley et al.*, 2005; *Koenig et al.*, 2014]. These effects depend on a previously uncertain connection between the firn aquifer and the broader subglacial hydrologic system.

Here we present the first direct evidence that fluid flow occurs within the aquifer accompanied by estimates of specific discharge and average linear velocity within the aquifer as well as bottom depths of the aquifer. These measurements support a direct

connection between meltwater within the firn aquifer and a drainage system. To estimate specific discharge and average linear velocity, we conducted borehole dilution tests at three sites in the aquifer. Dilution tests can be used to estimate groundwater flow by measuring the dilution rate of a tracer in a borehole by freshwater inflow [*Drost et al.*, 1968; *Freeze and Cherry*, 1979]. We also report for the first time the enrichments of dissolved solids in liquid water within a firn aquifer. We hypothesize that this occurs due to ion exclusion during clear (bubble free) ice formation at the base of the aquifer and meltwater infiltration transport of dissolved solids from the unsaturated zone above the aquifer to the saturated zone. The specific conductance of water in the aquifer correlates with the observed thickness of clear ice and likely places time constraints on aquifer formation.

3.3 Methods

We collected firn cores at three sites on the Greenland ice sheet on a flow line ~50km upslope from the terminus of Helheim Glacier, southeastern Greenland in July and August, 2016 (Figure 3.1). Cores were collected using a lightweight Thermal Drill developed by Jay Kyne. The drill consists of a ~ 1 m long metal tube with spring-driven core dogs and a heat ring at one end, that hangs by a poly-jacketed, Kevlar-reinforced power cable from a tripod at the snow surface. The system weighs approximately 55 kg total (~25 kg drill, Variac, and tools, and ~30 kg tripod). A 2 kW generator powers the heat ring. A variable transformer (Variac) controls power to the heat ring.

Cores were logged for density and stratigraphy. Four ice types were noted: firn, ice lenses, bubbly ice, and clear ice (Figure 3.2). Firn is dry or wet snow that lasts longer than a year without transforming to ice. Ice lenses form as surface meltwater infiltrates

downward through subzero snow and firn. Bubbly ice is equivalent to B-type (bubbly) ice defined by *Kameda et al.* [1993] or bubbly ice described by *Vallon et al.* [1976]. Clear ice is equivalent to T-type (transparent) ice defined by *Kameda et al.* [1993] and blue ice described by *Vallon et al.* [1976].

We used borehole dilution tests in boreholes left from firn core collection to determine rates of horizontal fluid movement within the aquifer. Borehole dilution tests have been used in a variety of settings to determine groundwater fluxes [*Havely et al.*, 1967; *Drost et al.*, 1968; *Jamin et al.*, 2015]. Many tracers have been used including radioactive or isotopic tracers, salinity, fresh water, or dye [*Ronen et al.*, 1986; *McLinn and Palmer*, 1988; *Pitrak et al.*, 2007]. During a test, a tracer is injected into the borehole. Groundwater flow through the borehole reduces the concentration of the tracer over time. Diffusion was not expected to contribute significantly to flow, particularly for pore water velocities greater than ~0.3 m/day [*Taylor et al.*, 1990]. Temperature driven flow was not expected to contribute significantly to flow as the measured temperature within the borehole at all depths was 0 °C (±0.2 °C). Hydraulic gradients drive horizontal and vertical flow. The observed vertical hydraulic gradients in the firn aquifer are generally less than the horizontal hydraulic gradient, which is approximately 0.01 m/m (slope = 0.8º), indicating that flow is primarily horizontal. The tests are relatively simple to conduct, a necessity for our light weight field operation, and provide detailed profiles of flow within the aquifer that we compare to theoretical flow estimates based on Darcy's law.

After measuring background specific conductance of the liquid water in the open boreholes at 30 cm intervals using a Hydrolab, we injected a dilute saltwater solution (10 g salt in 1 L water, resulting in a specific conductance around ~130 µS/cm in a borehole

with a 20 m saturated thickness) into the borehole and mixed it into the water in the borehole using a submersible well pump (12 volt Tornado pump by Proactive). The mass of salt added was designed to minimize density driven flow in the borehole and still provide a measurable change in specific conductance. For comparison, the specific conductance of drinking water typically ranges between 500-1000 uS/cm. To ensure complete mixing, we monitored the specific conductance in the borehole. We then monitored the specific conductance at 30 cm intervals in the borehole over the next ~24 hours to observe changes in specific conductance, which depend on the specific discharge of the aquifer. The specific discharge within an aquifer can be calculated as:

$$q = \frac{-\pi r}{2t\alpha} ln\left(\frac{C}{C_o}\right) \quad (3.1)$$

where q is the specific discharge (length/time), r is the borehole radius (length), t is time, α is a formation factor accounting for the attenuation of the velocity field by the borehole, commonly 2 [*Pitrak et al.*, 2007], and C/C_o is the relative concentration at a given time. The specific discharge is the flow of water per unit area of porous media (SI units of $m^3/(m^2\ s)$) and refers to the flux of water flowing through an area of the porous medium, even though the water only flows through connected pores. Thus, the actual velocity of the water flowing through connected pores will differ from the specific discharge. A combination of error in measurements of the borehole size, specific conductance, and time contribute to the specific discharge errors.

The average linear velocity (i.e., the actual velocity through connected pores), v, (length/time) can be calculated as:

$$v = \frac{q}{n} \tag{3.2}$$

where *n* is porosity. Average linear velocity refers to the average time that a tracer injected into an aquifer would travel a given distance.

To determine the relationship between stratigraphy and specific conductance, we correlated the total thickness of clear ice, firn, bubbly ice, and ice lenses at each site with the integrated specific conductance curve.

3.4 Results and Conclusions

3.4.1 Dilution of Saltwater Over Time in Boreholes

The specific conductance within the borehole at FA16_4 prior to saltwater injection is shown in Figure 3.3. The specific conductance of the injected salt water in the borehole decreases over time above a certain depth, indicating dilution of saltwater by freshwater flow through the borehole (Figure 3.3). The rate of dilution varies with depth. Below a certain depth, the specific conductance does not change, and never returns to the initial background value. The specific conductance returns to background levels above this depth in under 24 hours, indicating that freshwater is flowing across the borehole and rapidly diluting the saline mixture. The specific conductance profiles at FA16_5 and FA16_6 are not shown, but they show similar dilution within the flow zone and no dilution below the flow zone as at FA16_4.

The specific conductance increases between 35 - 40 m at 21 hours (Figure 3.3). However, within 6 hours, the increase is less that 10 µS/cm, and within 21 hours, it is only 25 µS/cm, so the change is small and has little influence on the overall dilution rates

because they are based on the dilution at each time interval. During the initial saltwater injection and mixing, some higher salinity water may have flowed to the very bottom of the borehole, below the intake of the pump at the bottom of the borehole. We removed the pump at the end of the day (after the measurements at 5.5 hours) and this may have mixed some higher salinity water up into the borehole that we measured after 21 hours.

The specific conductance profiles at FA16_5 at times between 16:00 and 18:00 increase and decrease unexpectedly. The profiles made at 1.5 and 3 hours were made by lowering the probe through the aquifer. The profiles made at 2.5 and 4 hours were made by raising the probe up through the aquifer. The profiles made while lowering the probe into the borehole have lower specific conductance than the profiles made while raising the probe up through the aquifer, suggesting that perhaps some fresher water from higher in the aquifer was dragged down with the probe or some saltier water from deeper in the borehole was pulled up with the probe. The variability in specific conductance related to logging direction results in specific discharge changes of 14% increase if logs at 1.5 and 3 hours are excluded or 29% decrease if logs at 2.5 and 4 hours are excluded. Future tests of this sort may consider using a smaller diameter specific conductance probe to minimize these effects and logging in one consistent direction.

3.4.2 Specific Discharge and the Bottom of the Flow Zone

Specific discharge and preinjection specific conductance profiles within the aquifer are shown for three sites in Figure 3.4. The specific discharge profiles reveal flow zones within the aquifer. The bottom of the flow zone can clearly be defined by the decrease in specific discharge to zero, and an aquifer thickness can be calculated as the difference between the water table and the bottom depths (Table 3.1). The specific

discharge is highest at the top of the aquifer (~$5x10^{-6}$ m/s), and generally decreases with depth towards the bottom (~$1x10^{-7}$ m/s). Some zones of higher specific discharge occur as well. Average and total specific discharge integrated over the aquifer thickness is shown in Table 3.2. The average at FA16_6 likely overestimates the specific discharge as the measurements stopped above the bottom of the flow zone, and so the portion of the aquifer with lower specific discharge at the other two sites is not included in the average. Increases and decreases in specific conductance and specific discharge correspond to large scale stratigraphic changes within the firn core. Still, clear ice and ice lenses do not completely prevent fluid flow. This may be related to the lateral extent of these layers. Even if they are impermeable, they may not be laterally extensive enough to prevent flow through layers below. The bottom of the flow zone flow cannot be determined from the firn stratigraphy or density profiles alone.

The preinjection specific conductance generally increases with depth to a peak, and then decreases near the bottom of the borehole. The maximum preinjection specific conductance is 18 µS/cm at FA16_6. The bottom of the flow zone from the borehole dilution tests coincides with the depth that the background specific conductance goes to zero at FA16_5. At site FA16_4, these depths differ by 5 m (the background specific conductance goes to zero at ~37 m while the specific discharge goes to zero at ~32 m). Our specific conductance measurements during the borehole dilution test at site FA16_6 did not go to the bottom of the flow zone because we incorrectly thought that the clear ice defined the bottom of flow. However, the background specific conductance measurements do go deep enough to observe specific conductance values of 1 µS/cm at the very bottom, suggesting that the bottom at this site is between 40 m to nearly 50 m depth, if the specific conductance trends behave similarly to site FA16_5.

For borehole FA16_4, between depths 31.3 m – 34.0 m, the initial specific conductance was slightly lower than the 1st reading, so the 1st reading was used as the initial condition. This is could be due to the Hydrolabs low precision at low total dissolved solids concentrations, combined with lower velocities near the bottom of the aquifer, which would not dilute the water enough to see measurable change at early times.

The hydraulic conductivity has been estimated as 2.7×10^{-4} m/s [*Miller et al.*, 2017] and the hydraulic gradient, determined from ground penetrating radar [*Forster et al.*, 2014] is about 0.01 m/m, yielding a specific discharge of 2.7×10^{-6} m/s. This Darcy's law estimate compares favorably to the specific discharge from the borehole dilution tests. The average specific discharge of all measurements within the aquifer at all sites is 4.3×10^{-6} m/s with a standard deviation of 2.5×10^{-6} m/s.

Montgomery et al. [2017] describe active source seismic surveys to identify the seismic velocity associated with the base of the aquifer. The bottom of the flow zone defined by the borehole dilution tests generally agree with the seismic bottom at two of the three sites. At FA16_4 and FA16_5, the depth defined by the seismic surveys generally aligns, within a few meters, with the bottom of flow identified in with the borehole dilution tests. However, at FA16_6, the seismic surveys identify the base at ~30 m, while the borehole dilution tests detect fluid flow below this depth. This difference is likely due to sensitivity of the seismic method to the substantial amounts of clear ice at this site.

3.4.3 Average Linear Velocity Profiles

The average linear velocity in the aquifer is shown in Figure 3.5 for 3 different assumed porosity values and mean average linear velocities for each site are shown in Table 3.3. The maximum average linear velocity is 9.2 m/d. The mean average linear velocity ranges from 0.1 – 4.6 m/d, depending on porosity. For these calculations, the porosity is assumed constant throughout the thickness of the aquifer. While this is likely not realistic, estimating velocities using a range of constant porosities produces a range of possible velocities within the aquifer. Further, the average linear velocity is presented to give a conceptual framework for fluid flow rates. However, porosity can vary significantly spatially and has been difficult to precisely define at our site. Further, we focus on specific discharge at it characterizes flow through the aquifer, whereas average linear velocity characterizes the velocity at which a tracer in the water would move.

The borehole dilution technique assumes instantaneous homogeneous mixing of the tracer in the borehole. Without this, artificial mixing can occur, altering velocity estimates. The velocities estimated are all relative to the initial specific conductance following saltwater injection and mixing, and so the velocities estimated may underestimate actual average linear velocities that would result from greater initial specific conductance.

3.4.4 Background Specific Conductance, Clear Ice Thickness, and Aquifer Age

The background specific conductance varies from site to site, and ranges between 0-2 µS/cm to 5-20 µS/cm at different sites (Figure 3.4). Increases and decreases in specific conductance correspond to stratigraphic changes within the firn core. The

background specific conductance generally increases with depth through the aquifer, peaks around depths featuring clear ice layers, and decreases to near zero below the bottom of the flow zone, near the deepest observation of clear ice (Figure 3.4).

Linear regressions were applied to the depth-integrated specific conductance and thickness of clear ice, ice lenses, bubbly ice, and firn (Table 3.4). The thickness of clear ice correlates with increased specific conductance within the aquifer (Figure 3.6). The depth-integrated specific conductance has a positive relationship to clear ice thickness. Although the correlation is not significant ($p = 0.1$), the specific conductance appears to have the strongest relationship to clear ice thickness relative to the other ice types. More field work is necessary to fully characterize this relationship including stratigraphy and background specific conductance measurements at more locations.

Impurities such as salts and minerals are present at low levels within firn due to surface deposition. When meltwater from the surface infiltrates through the firn, it can leach some amount of these impurities and transport dissolved solids (minerals, salts, or ions) to depth. The related smearing of geochemical records in ice cores by meltwater flow has been observed [*Koerner,* 1997; *Van Der Wel et al.*, 2011]. The total dissolved solids (TDS) concentration is greatest near the water table, indicating that the source of ions is from above. When a firn aquifer forms, the impurities present within the saturated firn dissolve into the liquid water as meltwater infiltration from the surface transports additional dissolved solids from above. As freezing at the base of the aquifer occurs, due to the cold interior of the ice sheet, the dissolved solids are excluded from the ice crystal lattice and concentrate instead in solution in the aquifer. We assume that this freezing process occurs uniformly across the base of the aquifer. Consequently, any horizontal concentration gradient that develops is weak to nonexistent, so dissolved solids

concentrations do not change laterally.

Over time, as burial continues, the prior bottom of the aquifer and associated clear ice move deeper. The dissolved solids are concentrated in the liquid and excluded from the clear ice, which gets buried, while the aquifer does not. Assuming that the temperature distribution with depth within the ice sheet remains constant, the basal freezing occurs at approximately the same depth over time, resulting in a new layer of clear ice at the same depth. The basal freezing and formation of clear ice prevent the burial of salts that normally would occur if the salts remained in place in dry firn following deposition. Over time, as surface salt and mineral deposition, meltwater transport of salts to depth, and basal freezing continues, the concentration of ions in solution in the aquifer increases. Thus, the salinity of water within the aquifer depends on surface deposition, meltwater transport to depth, and basal freezing. This is shown in Figure 3.7. Assuming these are generally constant processes, the longer the aquifer has existed at a given location, the more dissolved solids will accumulate within the aquifer.

The correlation between the specific conductance and the clear ice thickness supports the idea that the specific conductance increases due to the formation of clear ice (as well as surface sources). Clear ice forms when water freezes slowly enough that air bubbles, which contribute to a cloudy appearance by scattering light, can escape, and bigger ice crystals, which scatter light less, can freeze. Clear ice formation in glaciers has been attributed to freezing of percolating meltwater within a surface snowpack, and refreezing of gas-poor meltwater [*Hubbard et al.*, 2000]. As meltwater freezes slowly, bubbles and dissolved ions are excluded from the ice crystal lattice, and ions are concentrated in the remaining liquid, contributing to elevated specific conductance [*Canfield et al.*, 1983; *Miller and Aiken,* 1996]. The concentration of ions in solution

increases as this process continues.

Clear ice forms when water freezes very slowly or from water containing no dissolved gasses [*Carte*, 1961]. Snowmelt should have low dissolved gas content as ice crystals contain little gas, and meltwater recharge to the aquifer occurs too quickly for equilibration with the atmosphere. Completely clear ice can form when water is agitated enough to prevent buildup of dissolved air and freezing is slow [*Carte*, 1961]. Thus, the presence of clear ice is another indication that fluid flow and slow freezing occur in the aquifer. The flow allows dissolved gasses to escape from the already likely undersaturated meltwater, and gradual freezing forms clear ice. We assume this happens at the base of the aquifer, defined by the depth that the temperature dips below 0ºC, and liquid water freezes.

Bilelo [1968] attributes bubbly ice formation to freezing of slush that forms when liquid water saturates snow. Bubbles, which increase opacity, form as water containing dissolved gasses freezes. The freezing rate, amount of dissolved gas, pressure, water layer thickness, and bubble escape control bubble size and concentration in ice [*Carte*, 1961]. The faster ice forms, the greater the concentration of bubbles. Reduced gas content also leads to reduced bubble concentration and smaller bubbles. Bubbles tend to form at ice/water interfaces, indicating that gas supersaturation has occurred [*Carte*, 1961]. Bubbles tend to form in layers or waves, alternating with layers containing fewer bubbles, likely because the bubbles reduce the local availability of dissolved gas. Bubble formation can be inhibited until the supply of dissolved gas increases [*Carte*, 1961]. Some dissolved air that the ice expels as it forms may escape by diffusion through water, which can form a gas concentration gradient in front of forming ice. Gas may have a greater chance of diffusing if the ice forms slowly [*Carte*, 1961].

The growth rate of ice formed with air-saturated water at 0°C can be estimated from bubble concentrations using this relationship:

$$N = 20R^{1.7} \quad (3.3)$$

where N is the bubble concentration (number of bubbles/mm^3) and R is the rate of ice growth (mm/min) [*Carte*, 1961]. A simple calculation shows that in a 6 cm long core section of clear ice with 1 bubble, the formation rate would be ~1.5x10^{-4} mm/m. However, core microstructure work such as CT scans is required to meaningfully determine bubble concentration in our firn samples.

3.4.5 Salt Mass Balance

If we knew a refreezing rate, we could use the specific conductance to determine how long the aquifer has existed at a given location. This requires further study of the effect the aquifer has on grain metamorphism and melt/freeze processes within the saturated zone. In the absence of this information, we can apply a dissolved solids mass balance to estimate aquifer formations times. We can compare calculated total dissolved solids (TDS) in the aquifer to the mass of Na^+ and Cl^- in dry firn to show that the mass of salts in the liquid is close to or greater than the total mass of Na^+ and Cl^- in a dry firn column, indicating that the salts have been washed into the aquifer from the unsaturated zone and concentrated by clear ice formation and burial. Total dissolved solids include other ions in addition to Na^+ and Cl^-, so the comparison assumes that the major ions in solution are Na^+ and Cl^-. However, the core was extracted from a site ~ 60 km from the ocean and so this is an acceptable assumption.

We integrated concentrations of sodium (Na^+) plus chloride (Cl^-) from the ACT11b firn core (Joe McConnell, personal communication), taken near our study site but where no aquifer exists, over a range of core lengths (10m – 60 m) to determine the total mass of Na^+ and Cl^- per unit area (Table 3.5). Then we calculated the specific conductance if all the Na^+ and Cl^- in a unit area dissolved in volumes of water comparable to those at our field sites. We converted between specific conductance and total dissolved solids (T, mg/L_{liquid}) according to:

$$T = S_c * 0.6 \quad (3.4)$$

where S_c is specific conductance (µS/cm).

The specific conductance predicted if all the Na^+ and Cl^- in a range of core lengths dissolved in a 10 m thick aquifer (for a range of average porosities from 0.1-0.3), generally agrees with the average specific conductance measured at our field sites (2.9 µS/cm, 1.3 µS/cm, and 8.7 µS/cm at FA16_4, FA16_5, and FA16_6 respectively), as shown in Table 3.6. This supports the interpretation that the aquifer acquires salts through dissolution of salts within the firn, concentrates salts in the aquifer through ion exclusion during clear ice formation, and gains new salts through surface deposition and recharge. The total mass of Na^+ and Cl^- available to dissolve in the aquifer increases as the length of the dry core increases. A longer core section contributing salt to the aquifer implies that the aquifer has existed longer. The longer the aquifer has existed, the higher the specific conductance should be as the aquifer concentrates dissolved solids. The bottom of the clear ice is located at approximately 34 m, 35 m, and 48 m at FA16_4, FA16_5, and FA16_6 respectively. Although we estimate that the average porosity is less than 0.3,

we include the scenarios as an upper boundary.

Through this relationship, the salt mass balance constrains the date of aquifer formation. Dissolution and concentration of all the salt from a 40-60 m thick firn column is required to achieve the measured specific conductance in the aquifer. An approximate depth-age scale indicates that firn at 60 m depth was deposited in 1969. This layer would be the bottom of the aquifer when it first formed. The aquifer has concentrated all the salt within the firn pack from ~1969 onward. If we assume that the aquifer formed at ~30 m (the depth that the aquifer forms at the upstream edge), and remove 30 m (~19 years), this suggests the aquifer formed around ~1988. If the aquifer formed 100 years ago, the salt concentration in the aquifer would be higher than we measured. If the aquifer formed more recently, the salt concentration would be lower than we measured.

TDS includes other ions in addition to Na^+ and Cl^-. If these additional ions were included in calculations, the predicted specific conductance in the aquifer would increase. This would require a shorter length of core necessary, and indicate that the aquifer formed later than we have estimated. Therefore, our estimate is an early bound on the timing of aquifer formation.

As stated above, we assume that the clear ice formation occurs uniformly across the bottom of the aquifer. If this is true, we can treat this as a ~1D process, where the salt lost through discharge out of the aquifer is replaced by inputs from aquifer expansion upslope. Approximately 1 km/year of aquifer expansion inland is required to provide new salt inputs that balance salt loss due to aquifer discharge. This compares favorably with observed aquifer expansion rates of ~0.5 km/year inland. Additionally, ice flow towards the ocean brings ~ 100 m new firn into the aquifer each year.

Assuming the aquifer has existed at the low elevation site for 30 years, energy for

basal freezing can diffuse 65 m below the initial aquifer base. We do not have temperature measurements below ~50 m depth and so we cannot accurately describe the temperature 65 m below the base of the aquifer. However, the cold content of a 1 m x 1 m x 65 m column of ice, with an average temperature of -5 ºC to – 15 ºC, ranges between $1.9x10^9$ and $6.5x10^8$ J/m^2. At this site, we measured 7.11 m of clear ice. Clear ice formation at this site required $2.2x10^8$ – $6.6x10^8$ J, assuming firn porosity of 0.1- 0.3 prior to clear ice formation. The $6.6x10^8$ J represents a high estimate as the porosity at the base of the aquifer (depth >30 m) is likely much lower than 0.3 due to firn compaction. Therefore, the cold ice below the aquifer can accommodate the energy released from clear ice formation. Ice flow (~0.3 m/d) will supply additional cold content to allow basal refreezing to occur.

This first order analysis does not include a complete assessment of salt mass loss through aquifer discharge, nor do we account for temporal variability of recharge, surface deposition, or basal freezing rates. The predicted specific conductance represents lower limits on the specific conductance in an aquifer as they do not include all dissolved solids. However, we observe the general correlation of specific conductance to clear ice thickness, and describe a preliminary salt mass balance that describes sources and processes of salt accumulation over time within the aquifer. The longer the aquifer exists at a site, the higher the salt concentration should be.

The similarity between the measured specific conductance and predicted specific conductance, in addition to the correlation between background specific conductance and clear ice thickness, indicates that the total mass of salts within the firn column is retained within the aquifer. The water dissolves salts in the firn column and the clear ice formation prevents their downward movement through firn burial, thus concentrating the salts

within the aquifer. The correlation between background specific conductance and clear ice thickness, and lack of correlation with other ice type thicknesses, suggests that the clear ice formation process controls the specific conductance signal within the aquifer. More complete measurement of firn, water and surface impurity chemistry, surface deposition spatial variability, and aquifer expansion rate, and a more precise depth-age model would aid in the development of this model.

3.5 Conclusion

During the borehole dilution test in the firn aquifer, salt water mixed into an open borehole was diluted by freshwater inflow through the borehole. Dilution of saltwater over time in the borehole indicates that the water within the aquifer is flowing, and therefore must discharge from the aquifer somewhere down gradient. Discharge most likely occurs in the crevasse field downslope near the edge of the ice sheet as supported by radar imaging [*Miège et al.*, 2016]. The water moves through the aquifer relatively quickly. The specific discharge measurements from the borehole dilution tests (mean specific discharge of 4.3×10^{-6} m/s = 0.4 m/d) generally agree with the specific discharge predicted by Darcy's law (average specific discharge of 2.7×10^{-6} m/s. The ice sheet moves ~0.3 m/day, slower than the liquid flowing through the firn. The specific discharge of meltwater estimated in this study represents flow through the aquifer under current recharge rates (surface melt rates), and permeability within the aquifer that may change over time under changing climatic conditions.

The bottom depths identified with the specific discharge profiles agree with the bottom depth estimates from seismic surveys for two out of three sites that we can compare [*Montgomery et al.*, 2017]. The site where the two methods disagree is the

lowest elevation site, where the aquifer has likely existed for a longer time. The seismic method is sensitive to the presence of clear ice, which is greater at this site than at the other two sites, contributing to differences in the bottom depth estimates. The bottom of the aquifer is not apparent from ice core observations alone. Despite the impermeable appearance of ice, and specifically clear ice, it only reduces horizontal and vertical flow instead of preventing it. The true bottom of flow is determined by the temperature profile within the ice sheet. The bottom of the aquifer occurs where enough freezing occurs to close of connected pores to prevent fluid flow.

Firn can serve as a massive storage reservoir for meltwater [*Harper et al.*, 2012; *Humphrey et al.*, 2012]. However, the flow within the firn aquifer suggests that in areas where firn aquifers occur, storage is not long term, and discharge, possibly to the ocean, may actually be enhanced. Firn storage has already reached 50% of capacity [*Koenig et al.*, 2014]. The saturation of the pore space maximizes hydraulic conductivity and allows meltwater generated inland to travel faster, and further, towards the edge of the ice sheet than if the meltwater were flowing through unsaturated firn. The insulating properties of the thick overlying firn prevent the meltwater from refreezing, resulting in a perennial mechanism for meltwater originating tens of kilometers from the edge of the ice sheet to connect with the englacial hydrologic system near the edge and discharge. Although the firn contains a large storage capacity, the firn aquifer and its connection to the broader glacial hydrologic system allows meltwater to flow out of the firn, thus reducing the effective storage capacity.

This differs from areas without firn aquifers. In some cases, discharge of meltwater generated during the melt occurs during the melt season (e.g., streams and lakes flowing across bare ice and discharging to the land or ocean). In some cases, melt

generated during a melt season is stored in the firn column as ice following infiltration and refreezing. In some cases, meltwater is stored in firn pore space as liquid over multiple melt seasons [*Humphrey et al.*, 2012], but it may not be connected to the broader hydrologic system required for discharge from the ice sheet. Once the connection to the broader hydrologic system develops, this meltwater can leave the ice sheet. In the absence of an aquifer connected to the broader englacial hydrologic system, meltwater may refreeze without flowing very far because the hydraulic conductivity in unsaturated material is much lower than in saturated material. Once enough meltwater accumulates to saturate the firn, it can develop connections to the glacial hydrologic system. Without an aquifer, the firn can act as a more effective meltwater storage reservoir. In southeast Greenland, meltwater recharges the aquifer, travels through the saturated zone, and flows out of the aquifer, likely into crevasses at the edge of the ice sheet. Still, the fate of meltwater after it discharges from the aquifer remains unknown, and requires further study to fully quantify the effects on ice sheet dynamics, mass balance, and sea level rise.

The relationship between clear ice formation and increased background specific conductance within the aquifer sheds light on refreezing processes within the aquifer and the duration of aquifer existence at a given site. The more clear ice formed, the greater the total dissolved solids concentration and background specific conductance in the liquid water. Total dissolved solids increase as ions in solution in the aquifer, transported by meltwater infiltration from above, are excluded into the liquid during clear ice formation. The aquifer continues to receive dissolved solids from the surface, but the downward movement of these ions is prevented by the clear ice formation, resulting in enrichment of the liquid water over time. Dating cores from areas with firn aquifers is difficult as the meltwater infiltration obscures geochemical signatures. This makes simply using the

bottom depth of clear ice as the age of the aquifer formation difficult. However, a mass balance approach to the total dissolved solids concentration of the liquid water places time limits on the extent the aquifer has existed at a given location. From this perspective, the aquifer formed in this area no earlier than the late 1980s, suggesting it formed as an impact of global climate change and the associated warming of the Arctic.

Table 3.1.Water table and aquifer base depths. Depth to water table, bottom of flow, and aquifer thickness at three sites determined by borehole dilution tests. We did not measure changes in specific conductance deep enough to detect the bottom of flow at FA16_6. Therefore, we provide a range from the bottom of our measurements to the bottom to the specific discharge measurements, which go to zero coincident with the bottom of flow at FA16_5.

Site	**FA16_4**	**FA16_5**	**FA16_6**
Depth to water table (m)	20.14	22.53	9.98
Depth to bottom of flow (m)	31.7	30.5	40.2 -47.8
Aquifer thickness (m)	11.6	8.0	30.2-37.8

Table 3.2. Specific discharge estimates. Average specific discharge, standard deviation, and total specific discharge (per unit width of aquifer) at each site. The total discharge is the specific discharge integrated over the thickness of the flow zone. *The estimates at FA16_6 are likely an overestimate as we did not capture the bottom of the flow zone, where the specific discharge should be lower. Specific discharge calculated using Darcy's law is 2.7×10^{-6} m/s.

	FA16_4	**FA16_5**	**FA16_6***
Average specific discharge (m/s)	2.9×10^{-6}	2.2×10^{-6}	5.6×10^{-6}
Standard deviation	1.5×10^{-6}	2.2×10^{-6}	2.2×10^{-6}
Total discharge through flow zone (m^2/s)	3.3×10^{-5}	1.7×10^{-5}	1.7×10^{-4}

Table 3.3. Average linear velocity estimates. Mean average linear velocity at each site with different porosity estimates.

	FA16_4			**FA16_5**			**FA16_6**		
Porosity	0.1	0.2	0.3	0.1	0.2	0.3	0.1	0.2	0.3
Average (m/d)	2.5	0.4	0.1	1.9	0.9	0.7	4.6	1.1	0.3
Standard deviation	1.4	0.2	0.0	1.9	1.0	0.6	1.3	0.4	0.1

Table 3.4. Ice types and relationship to specific conductance. Thickness of ice type, depth-integrated specific conductance, and the linear model relationship.

Site	Clear ice thickness (cm)	Ice thickness (cm)	Bubbly ice thickness (cm)	Firn thickness (cm)	Total (cm)	Total specific conductance (µS/cm)
FA16_4	157	780	1068	2045	4050	170.4
FA16_5	122	503	1102	2112	3839	9.5, 9.6
FA16_6	711	517	1323	2392	4943	328.4
Slope	0.47	0.25	1.03	0.74		
Intercept	-2	-16	-1056	-1473		
Pearson Correlation Coefficient	0.89	0.23	0.79	0.75		
r^2	0.80	0.05	0.63	0.56		
p- value	0.10	0.77	0.20	0.25		

Table 3.5. Measured and predicted salt content of cores. Mass of Na^+ and Cl^- in ACT11b firn core, and estimates of concentration if all Na^+ and Cl^- in a range of core lengths dissolved in a 10 m thick aquifer. For comparisons, the average specific conductance at FA16_4 is 2.9 µS/cm, at FA16_5 is 1.3 µS/cm , and at FA16_6 is 8.7 µS/cm.

Core	Total Na^+ & Cl^-	Concentration if all salt in a length of core dissolved in a 10 m thick aquifer						Predicted specific conductance		
		p = 0.1	p= 0.2	p= 0.3	p = 0.1	p= 0.2	p= 0.3	p = 0.1	p= 0.2	p= 0.3
m	mg/m^2	mg/m^3	mg/m^3	mg/m^3	mg/L	mg/L	mg/L	µS/cm	µS/cm	µS/cm
10	279.5	279.5	139.7	93.2	0.3	0.1	0.1	0.5	0.2	0.2
20	1456.7	1456.7	728.4	485.6	1.5	0.7	0.5	2.4	1.2	0.8
30	1965.7	1965.7	982.9	655.2	2.0	1.0	0.7	3.3	1.6	1.1
40	3426.7	3426.7	1713.3	1142.2	3.4	1.7	1.1	5.7	2.9	1.9
50	4179.0	4179.0	2089.5	1393.0	4.2	2.1	1.4	7.0	3.5	2.3
60	4529.7	4529.7	2264.9	1509.9	4.5	2.3	1.5	7.5	3.8	2.5

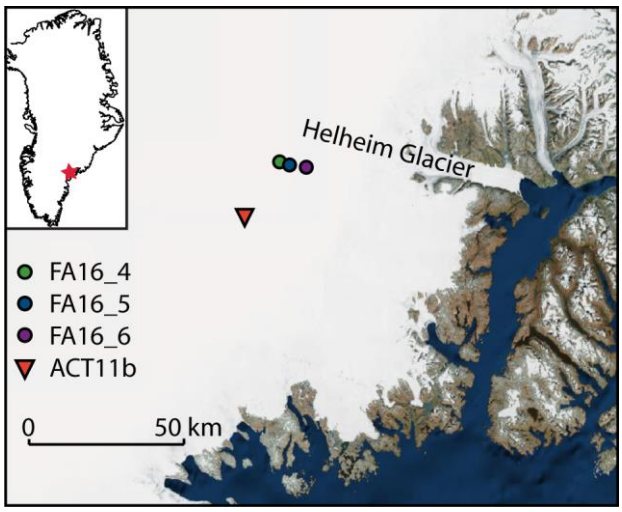

Figure 3.1.Site map. Site map showing sites where we collected firn cores and conducted borehole dilution tests (FA16_4, FA16_5, and FA16_6) in 2016 and where a dry firn core was collected (ACT11b), which was analyzed for Na^+ and Cl^- concentrations. Source: Esri, DigitalGlobe, GeoEye, Earthstar Geographics, CNES/Airbus, USDA, USGS, AeroGRID, IGN, and the GIS User Community.

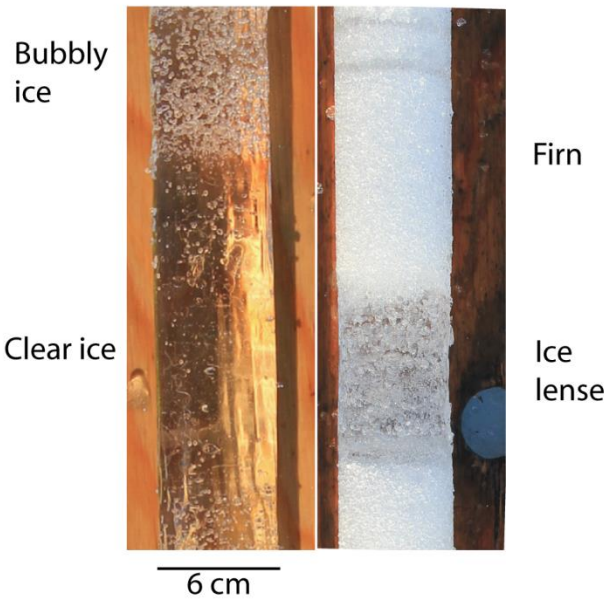

Figure 3.2. Photo of ice types in cores. Photos of firn cores showing bubbly ice, clear ice, firn, and ice lenses lying on top of wooden boards.

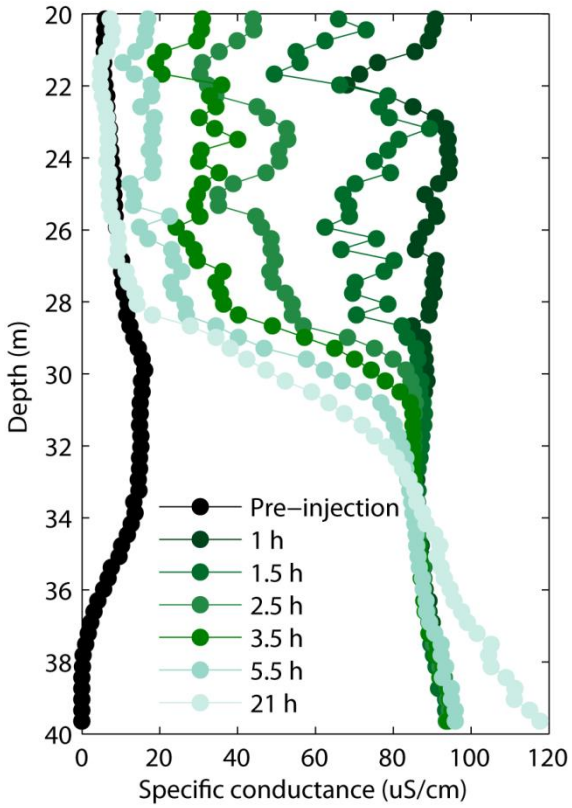

Figure 3.3. Specific conductance over time. Plot showing dilution of injected salt water over time within a borehole at FA16_4 due to inflow of freshwater. The water table is at 20 m. Specific conductance returns to background levels in ~21 hours within the flow zone (20 m – 32 m). Below 32 m, no dilution occurs, indicating that no water flow occurs. A pump to mix saltwater uniformly within the borehole was located at 41 m depth. The increase in specific conductance between 35 and 40 m after 21 hours is likely related to removal of the pump and mixture of higher salinity water up into the borehole following the measurement at 5.5 hours.

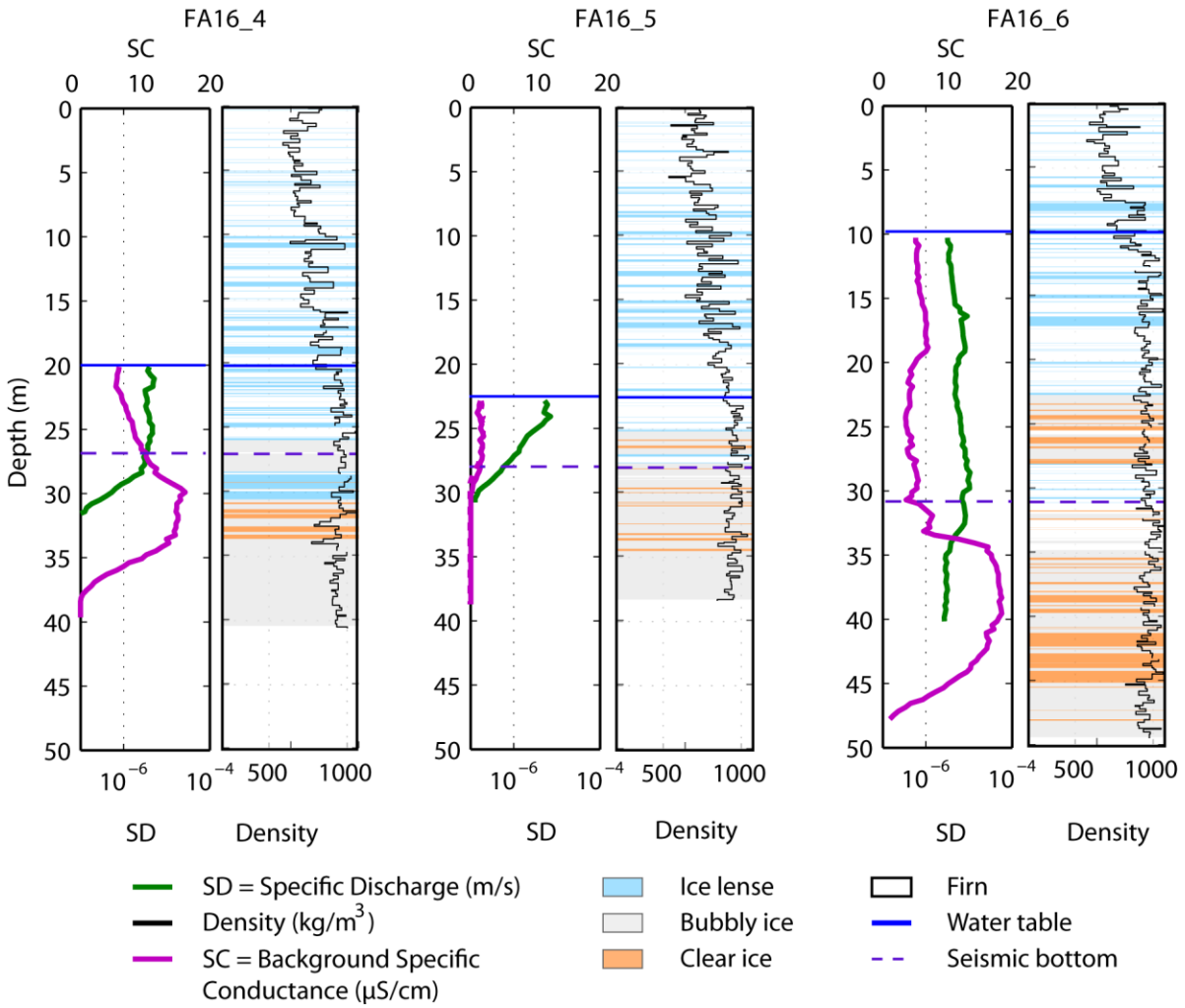

Figure 3.4. Specific discharge, specific conductance, density, and stratigraphy. Plots showing the specific discharge (SD), background specific conductance prior to saltwater injection (SC), firn density, and stratigraphy, depth to the water table, and aquifer base from seismic survey for sites where borehole dilution tests were performed. The background specific conductance was measured twice at FA16_5 with similar results (dashed pink line).

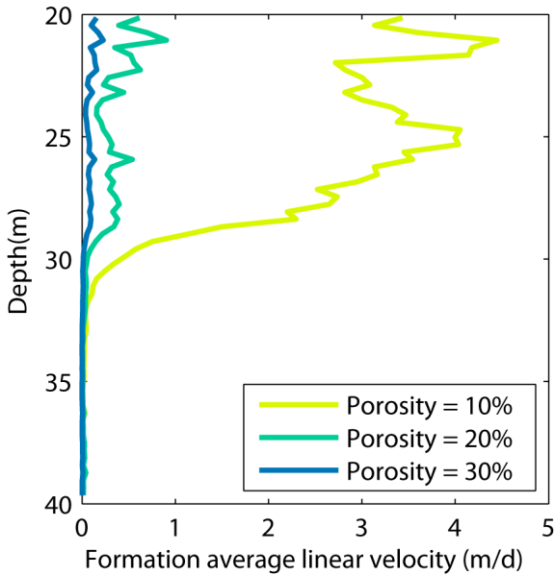

Figure 3.5.Average linear velocity. Average linear velocities of water within the firn at site FA16_4 for porosities between 10% and 30%.

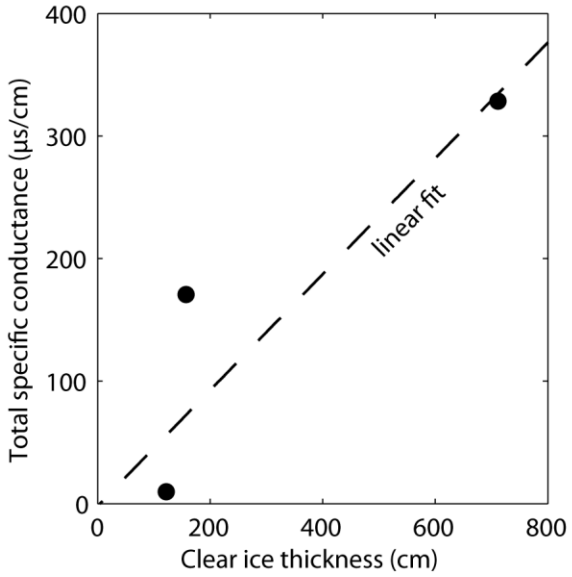

Figure 3.6. Clear ice thickness compared to the integrated specific conductance profile. The integrated specific conductance profile correlates with clear ice thickness (r^2 = 0.8).

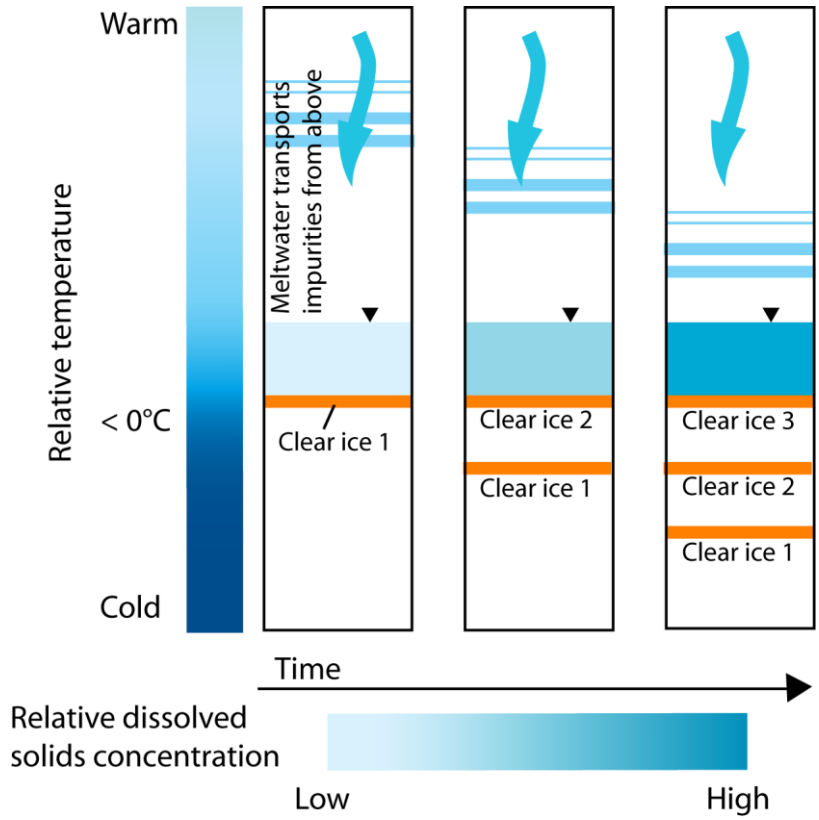

Figure 3.7. Diagram showing total dissolved solids increasing in the aquifer over time. Initially, the ions in the aquifer result from dissolution within the saturated zone. Clear ice (orange) forms at the base of the aquifer as the temperature decreases with depth. During refreezing, dissolved solids concentrate within the liquid. Over time, new surface deposition occurs, bringing a supply of impurities at the surface and burial of the firn. Surface meltwater percolation through the unsaturated zone transports dissolved solids to the aquifer. The clear ice gets buried, while dissolved solids previously associated with the firn that has refrozen as clear ice remain in the aquifer.

CHAPTER 4

CONCEPTUAL AND NUMERICAL HYDROLOGIC MODELING OF A FIRN AQUIFER IN SOUTHEAST GREENLAND

4.1 Abstract

Firn aquifers have been observed across regions of the Greenland ice sheet with high accumulation and melt rates [*Forster et al.*, 2014; *Kuipers Munneke et al.*, 2014]. Firn aquifers form when surface meltwater infiltrates to depth, warming the subsurface to the melting point, such that future melt can persist perennially in liquid form. Meltwater within the aquifer flows through the firn and discharges, likely to crevasses at the edge of the ice sheet (Chapter 3). Here we present data to characterize firn temperatures, recharge rates and timing, and aquifer age and residence time. Temperatures within the upper 10 m of the firn vary seasonally, while below 10 m and through the aquifer they remain at the melting point until ~40 m, where they begin to cool. Recharge rates range between 13-33 cm/year, with an average of 22 cm/year. Meltwater from the surface infiltrates to the aquifer in under 2 days, and can stay in the aquifer between ~8-23 years before discharging from the aquifer. We integrate field observations into a conceptual hydrologic model that we test with numerical simulations to understand how recharge rates influence the growth of the aquifer. Aquifers grow as recharge rates, which depend on melt rates, increase. We find little evidence in model simulations that the firn aquifer

stores liquid and catastrophically releases it. Instead, water appears to be able to continuously drain, although further research is needed to obtain direct observations of this

4.2 Introduction

Large firn aquifers, located around the perimeter of the Greenland ice sheet [*Forster et al.*, 2014; *Miège et al.*, 2016] are a potentially significant contributor to sea level rise (0.4 mm) [*Koenig et al.*, 2014]. The aquifers store meltwater within the compacting snow/firn throughout the year and persist over multiple years [*Miège et al.*, 2016]. Although initially thought to serve as potential meltwater storage mechanisms, flow measurements indicate that water discharges from the aquifers (Chapter 3). Aquifers form within the percolation zone at elevations between 1200 and 2000 m, in areas of high snow accumulation [*Forster et al.*, 2014; *Miège et al.*, 2016].

The high accumulation provides pore space necessary to contain meltwater. Firn pore space has the potential to store considerable volumes of meltwater (300-1300 Gt) [*Harper et al.*, 2012]. Retention and refreezing of meltwater prevent ~40% of rain and meltwater from reaching the ocean [*van Angelen et al.*, 2012, 2013]. However, pore space volume has been predicted to decrease by over 50% by the end of the 21st century, thereby accelerating surface mass loss [*van Angelen et al.*, 2013]. Meltwater that refreezes warms the surrounding firn and reduces pore space as ice fills previously open pore space [*Pfeffer*, 1991]. Meltwater in an aquifer doesn't refreeze and contribute to permanent storage. Aquifers that discharge meltwater reduce the buffering capacity of the firn by allowing meltwater to drain instead of being stored in pore space.

While meltwater storage may decrease through refreezing, meltwater production

on the ice sheet is projected to increase as global temperatures rise, and this may allow firn aquifers to expand inland. It may also increase the supply of water available to hydrofracture crevasses to the base of the ice sheet, potentially increasing ice velocity [*Alley et al.*, 2005; *Koenig et al.*, 2014; *Mcnerney*, 2016; *Poinar et al.*, 2017]. Understanding the fate and transport of that meltwater is critical to predicting the ice sheet's response to climate change, and impact on sea level rise.

In this chapter, we describe aquifer recharge characteristics (amount, timing, and rate), the mean residence time of water within the aquifer, and temperature conditions within the firn. We combine these with descriptions of the aquifer geometry [*Montgomery et al.*, 2017] , hydraulic properties [*Miller et al.*, 2017], and flow observations (Chapter 3) to describe a conceptual model of the aquifer persistence. The geometry of the aquifer has been determined through both in situ and geophysical methods at our field site in southeast Greenland. The water table depth and elevation have been determined by ground penetrating radar and water level measurements, while the base of the aquifer has been determined by active source seismic surveys and borehole dilution tests [*Miège et al.*, 2013; *Montgomery et al.*, 2017, Chapter 3]. On average, the water table is located at 20m depth, the bottom is located at 30 m depth, and the aquifer is ~10 m thick [*Miège et al.*, 2016; *Montgomery et al.*, 2017]. Hydraulic conductivity profiles were measured with depth-specific slug tests and as a bulk measurement with aquifer tests, described in Chapter 1 [*Miller et al.*, 2017]. Flow within the aquifer has also been observed, and behaves according to Darcy's law (Chapter 3).

We then integrate this conceptual model into a numerical groundwater flow model, SUTRA-ICE in 1D and 2D. SUTRA-ICE simulates fluid flow through the unsaturated and saturated zones, and accounts for freezing and thawing processes [*Voss*

and Provost, 2010; *McKenzie et al.*, 2007]. We show that the basic conceptual model can be simulated numerically, indicating that the major controls on the aquifer are adequately constrained. We also show how increasing or decreasing recharge rates can cause the aquifer to grow or shrink in response to climate change.

4.3 Methods

4.3.1 Site Description

The surface-based measurements were made in the southeast region of the Greenland ice sheet ~60 km west of Sermilik Fjord on a flow line of Helheim Glacier (Figure 4.1). This location has a history of measurements including annual measurements from NASA Operation IceBridge beginning in 2010 [*Miège et al.*, 2016]. The history of data at this site provides a broad sampling of additional geophysical measurement to support our new hydrologic measurements.

We conducted field work in April, July and August, 2015 and July and August, 2016. At all six sites we advanced a heated piezometer through the upper snowpack and firn and aquifer to collect depth specific water samples for chemical analysis and conduct hydraulic measurements [*Miller et al.*, 2017]. At five of the six sites, we also drilled firn cores to a maximum depth of ~60 m with mechanical and thermoelectric drills (all sites except FA15_2). We subsampled these for tritium measurements. At two of the five core sites we installed temperature strings and pressure transducers in the boreholes to records hourly changes in temperature and water levels (FA15_1, FA15_2) and at FA16_4 we installed a pressure transducer. We installed devices to measure compaction at two sites (FA15_2, FA16_4). At FA16_4, we sprayed fluorescent dye on the snow surface and cored through the dye. An automatic weather station (iWS), installed in April 2014 as

part of the PROMICE network (www.promice.org) has collected standard weather data. The station was located ~25 km south of our field sites, but we relocated it to FA16_1 in August 2015.The spatial variations in depth and extent of the water table were imaged using ground penetrating radar (GPR).

4.3.2 Recharge Estimates

4.3.2.1 Meltwater Generation from Surface Energy Balance and Degree Day Modeling

The melt in 2014, 2015, and 2016 was calculated by the surface energy balance, following [*Van Den Broeke et al.*, 2010]. The iWS station was relocated on August 10, 2015 from 66.18N and 39.04W at 1560 m elevation to a new location along our study profile at 66.36N 39.31W at 1661 m elevation. Gaps in the dataset exist because the station was buried during the late spring and summer of 2015. The dataset also ends in early August, 2016, when we were last able to download data. To account for the incomplete melt totals during the 2015 and 2015 melts season, we assumed that the melt season lasted 100 days, as it did in 2014, and multiplied the total calculated melt from the existing data by a factor to complete the 100 days. For example, if we only had 50 days of data, we multiplied the total melt by 2 to get 100 days of data. The energy available for melting (M) is calculated as:

$$-M = SW_{in} + SW_{out} + LW_{in} + LW_{out} + SHF + LHF + G_s \quad (4.1)$$

where SW_{in} and SW_{out} are incoming and reflected shortwave radiation fluxes, LW_{in} and LW_{out} are incoming and emitted longwave radiation fluxes, and SHF and LHF and

turbulent fluxes of sensible and latent heat, and Gs is the subsurface conductive heat flux.

We also estimated total snowmelt available for recharge using a degree day model. The degree-day model takes all the time when the air temperature is above zero (and thus snowmelt can occur) and multiplies that by a Degree Day Factor (DDF, kg melt/$m^{-2}d^{-1}K^{-1}$). Surface melt is calculated using the simple positive degree day equation [*Braithwaite,* 1985; *Hock,* 2003]:

$$m = DDF \sum (T - T_0)\, \Delta t \qquad (4.2)$$

where m is melt (length), DDF is a degree day factor (mass $lengh^{-2}$ $time^{-1}$ $temperature^{-1}$), T is temperature above a threshold, T_0, and Δt is a time interval. A range of DDFs calculated for similar latitudes in the ablation zone in SW Greenland were used, and compared for reference temperatures of 273.15 and 268 K [*Van Den Broeke et al.*, 2010].

The surface melt represents the total amount of water available to recharge the aquifer. However, some of the total melt is retained and refrozen during infiltration through the unsaturated zone and never reaches the aquifer. Recharge to the aquifer was estimated using several techniques: the volumetric flow method and the water table fluctuation method.

4.3.2.2 Darcy/Volumetric Flow Method

To estimate recharge using the volumetric flow method, the volumetric flow (*Q*) is divided by the length of aquifer as:

$$R_D = \frac{Q}{\partial x} = \frac{AK\partial h}{\partial x} \quad (4.3)$$

where R_D is the recharge rate (length/time), Q is the volumetric flux of water (length^3/time), A is the cross sectional area across which flow occurs (length^2), K is the hydraulic conductivity (length/time), ∂h is the change in hydraulic head (length) across a distance of ∂x (length). The water table has an average gradient of 0.01 m/m at our study site [*Miège et al.*, 2016] and an average thickness of 11 m [*Montgomery et al.*, 2017]. The mean hydraulic conductivity at our site is 2.7x10^{-4} m/s [*Miller et al.*, 2017].

4.3.2.3 Specific Yield and Water Table Fluctuation Method

Water table fluctuations in boreholes are commonly used to estimate recharge [*Risser et al.*, 2005] as:

$$R = S_y * \Delta h \quad (4.4)$$

and

$$R_r = S_y \frac{\Delta h}{\Delta t} \quad (4.5)$$

where R is recharge (length), R_r is recharge rate (length/time), s_y is specific yield, h is water table height (length), and t is time. We conducted aquifer tests, described fully in *Miller et al.* [2017] to determine aquifer specific yield. During an aquifer test, water was pumped from a borehole and the water level change was recorded in the pumping well

and one or two observation wells. The aquifer storage and trasmissive parameters are determined through a curve fitting method.

The water table fluctuation method assumes that the specific yield is constant and that the water level rises as recharge water arrives at the water table. While the water level can rise for other reasons (changes in atmospheric pressure, earth tides, and entrapped air), the water level rise in the firn aquifer is assumed to be solely due to recharge. However, lateral flow from upslope may also contribute to water level changes. Lateral flow from upslope contributing to water table rise results in overestimation of recharge. Downslope lateral flow that occurs while the water table rises results in underestimation of recharge.

4.3.3 Aquifer Time Scales

4.3.3.1 Tritium and CFC Ages in Firn and Meltwater

Tritium is a naturally and anthropogenically produced isotope of hydrogen whose concentration in the atmosphere has changed over time as a result of above-ground nuclear weapons testing. Tritium can be used to date waters recharged with the past ~60 years. As part of the water molecule, tritium is a useful tracer of water movement. To date firn and water in the aquifer, we matched the atmospheric tritium signal to the tritium measured in profiles through the aquifer [*Cook and Solomon*, 1997]. This provides a general timeframe of the firn and meltwater (pre- or post-1960s).

Tritium concentration was measured in subsamples of firn cores and water pumped out of the aquifer. Liquid water samples were collected in 0.5 liter LDPE sample bottles. Firn core was collected in plastic bags following stratigraphic description, melted, and transferred to 0.5L LDPE bottles. Tritium concentrations are reported in tritium units

(TU) where one TU equals one molecule of $^{3}H^{1}HO$ in 10^{18} $^{1}H_2O$ molecules. Tritium was analyzed with the in-growth method at the University of Utah's Dissolved Gas Lab.

Tritium concentrations in precipitation were obtained from IAEA/WMO [2015]. The precipitation dates were converted to depths using a depth-age model developed from an ice core taken at ACT11B similar to *Miege et al.* [2013].

Chlorofluorocarbons (CFCs) are synthetic organic compounds used in a wide range of industrial applications beginning in the 1930s, resulting in widespread release into the atmosphere. Following the 1987 Montreal Protocol, their emissions have been reduced to prevent ozone depletion. CFC-11, CFC-12, and CFC-113, can be used to determine the apparent year water recharges an aquifer. To determine apparent recharge ages, the CFC concentration in a groundwater sample is compared to the known historical (~ past 60 years) atmospheric concentration, assuming that the water was in equilibrium with the atmosphere prior to recharge. Concentrations of CFC gasses were measured in samples of firn aquifer water on a gas chromatography system at the University of Utah's Environmental Tracers Lab.

4.3.3.2 Fluorescein Dye and Recharge Timing

After spraying fluorescent dye across a 5m x 5m area at FA16_4, we drilled a firn core through the center of the area, and sampled it for dye concentration. We measured dye concentration of melted firn core samples at the USGS Utah Water Science Center using a Turner Designs 700 laboratory fluorometer.

4.3.3.3 Mean Residence Time Estimates

The mean residence time of water within the aquifer is calculated as:

$$T = \frac{b*\phi}{R} \tag{4.6}$$

where b is aquifer thickness (length), ϕ is porosity, and R is recharge rate (length/time) [*Focazio et al.*, 1998; *Cook and Böhlke*, 2000]. This calculation assumes steady state flow conditions exist and aquifer thickness and recharge rates remain constant.

4.3.4 SUTRA-ICE Numerical Simulations

After developing a conceptual model from field measurements and observations, we tested this model using SUTRA-ICE (v 4.0) [*Voss et al.* in preparation], a code that simulates saturated and unsaturated groundwater flow, energy transport, and accounts for freezing and thawing of groundwater. SUTRA-ICE is a progression of the SUTRA code. The freeze-that capability accounts for the latent head to fusion and varies thermal properties with changing total-water saturation, liquid saturation, and ice saturation. Total water saturation is the sum of liquid saturation and ice saturation, and saturation refers to the volume per pore volume. It also allows the effective permeability to change as a result of phase changes. The model does not account for air flow, vaporization, or sublimation in unsaturated zones. To adapt SUTRA-ICE, which has primarily been used in permafrost studies, to ice sheet conditions, the mineral phase of the model domain was assigned a permanent 'backbone' fraction of 0.4 and given the properties of ice. Within the remaining 0.6 pore space, the saturation of liquid and ice varies depending on pressure

and temperature. Seasonal snow cover porosity ranges between 0.4 for dense snow to 0.98 for freshly fallen, dry snow [*Armstrong*, 2008]. The permanent 'backbone' of ice can never melt. Therefore, we cannot simulate complete melting of the ice, although if this were to occur, there would be no aquifer to simulate either.

The properties of liquid and ice are shown in Table 4.1. For discussions related to SUTRA-ICE, water refers to liquid and ice. Liquid refers to the liquid phase and ice refers to the solid phase. The user must define three functions: 1) the total water saturation (unsaturated function), 2) the relative permeability function, and 3) the liquid water saturation (freezing function). Currently, no direct data exist to accurately characterize these processes so we made some data-informed estimates to develop these functions. As the fluid pressure decreases, 1% of total water is assumed to be retained in pore space as the total residual water saturation. When total water decreases, ice is lost first. Liquid water is assumed to freeze exponentially from 0 ºC to the minimum residual liquid saturation at -0.2 ºC. As liquid freezes, the effective permeability is assumed to decrease ~100 times.

For the residual liquid saturation, we considered the range of values described in *Langen et al.* [2017], and also tested a range of values to match a measured firn temperature profile. The functions used in SUTRA-ICE are not directly comparable to those in *Langen et al*. [2017]. In SUTRA-ICE, the total water saturation (ice and liquid) depends on the fluid pressure, the relative permeability depends on the liquid saturation, and the liquid saturation depends on the temperature. In *Langen et al*. [2017] the liquid saturation depends on the mass of water and snow in each layer and the density. The relative permeability functions are comparable, although *Langen et al.* [2017] use the van Genuchten form, and we use a piecewise linear form to reduce numerical instability

during simulations. *Langen et al.* [2017] do not use a function directly comparable to the total water saturation function.

4.3.4.1 1D Simulations

To calibrate the functions and parameters in SUTRA-ICE we conducted a sensitivity analysis using a 1D model, which focuses on unsaturated zone processes. We compared modeled temperature profiles to measured temperature profiles for April 2016. We installed a temperature string at FA15_1 in April 2015. In August 2016, the surface temperature sensor was located ~1.5 m below the new snow surface. A burial rate of 0.1 m/month was applied to the temperature sensor depths from 2015 to determine the sensor depth in April 2016. In reality, each sensor was lowered by ~1.2 m. However, SUTRA-ICE observation nodes occur at 1 m intervals, and so the measured depths were only lowered by 1 m to align with SUTRA-ICE temperature observations.

For the sensitivity analysis, April temperature profiles in a 1D firn column were simulated. The firn column simulation begins during the prior summer, when the firn pack is isothermal at 0 ºC, and the water table is located at 20 m depth. Recharge of 0 ºC water occurs for 1.5 months, then stops. The liquid water is allowed to drain from the unsaturated zone to the aquifer for 1 month, and then the surface temperature is lowered to a specified temperature for 7 months. From the iWS data, the average air temperature for 2015 was -13 ºC. The average winter temperature for 2015 (January 1- April 30, and October 1-December 31) was -19 ºC.

To characterize the effect of liquid water on the unsaturated zone temperature, ‘dry’, ‘wet’, and ‘icy’ base cases were established. In the ‘dry’ base case, the residual total water saturation (ice + liquid) is low (0.01). In the ‘icy’ base case, the residual total

water saturation is higher (0.2). In the ‘wet’ base case, the residual liquid saturation is high (0.2, which was the highest irreducible liquid content determined in *Langen et al.* [2017]), which keeps more liquid in the firn pack as the temperature decreases. For each base case, the surface temperature during the winter, amount of summer recharge, fraction of backbone ice, unsaturated function, relative permeability function, and freezing function were varied over a range of values (see Table 4.2). Final temperatures for each scenario were compared to the base cases and the measured firn temperatures.

4.3.4.2 2D Simulations

To simulate the firn aquifer profile, we defined temperature and fluid pressure boundary conditions, and the freezing, unsaturated, and relative permeability functions over a 16 km, 50 m thick 2D profile. The downslope boundary is simulated as the edge of an open crevasse that fluid can flow in or out of with a constant, hydrostatic fluid pressure. For simplicity, recharge occurs uniformly across the top of the model, although in reality, non-uniform recharge is likely. The temperature at the base of the profile is constant at -1 ºC. Permeability was defined according to field measurements. The dispersivity was increased to reduce numerical instability in the nonlinear calculations during simulations. Recharge rates were varied to see their impact on the aquifer.

4.4 Results and Discussion

4.4.1 Temperature Profiles

A generalized depth profile of temperature throughout the year is shown in Figure 4.2. The surface temperature and firn temperature above ~10 m varies seasonally. The firn is coldest in May, and then warms throughout June as the surface temperature

increases until it becomes isothermal at 0 ºC. It remains isotheral at 0 ºC through August, until surface temperatures cool. This cooling continues through the fall and winter. The firn within the aquifer is close to 0 ºC throughout the year. Below the aquifer, the temperature decreases below 0 ºC. The temperature of the firn controls the bottom of the aquifer. At FA15_2, the lower elevation site, the ice below the aquifer is warmer by ~1 ºC than at FA15_1, the upper elevation site.

4.4.2 Recharge Estimates

4.4.2.1 Meltwater Generation from Surface Energy Balance and Degree Day Model

The surface energy balance suggests ~30-54 cm of meltwater were generated at the snow surface. The meltwater available for infiltration estimated from the degree day modeling is summarized in Table 4.3. The melt rates from the energy balance estimates also constrain the appropriate DDF for this site to lower values of 1-1.5 mm/d K for a reference temperature of 268 K or 8-10 mm/d K for a reference temperature of 273.15 K. The surface melt estimates represent the total available water at the snow surface that could infiltrate through the unsaturated zone and recharge the aquifer. However, some of this meltwater is retained in the unsaturated zone through refreezing, which warms the firn and forms ice pipes and lenses, and so the actual amount of water that recharges the aquifer is less than this total amount. This is shown in Figure 4.3, which compares the total amount of meltwater generated at the surface compared to the estimates of water that recharges the aquifer. The recharge cannot be greater than the total melt generated. The difference indicates the amount of water that is retained through refreezing processes in the unsaturated zone, or is sublimated to the atmosphere.

4.4.2.2 Recharge from Volumetric Flow Method

The recharge estimated using the volumetric flow method ranges between 16-24 cm/year, depending on the hydraulic conductivity and aquifer thickness at the lower edge of the aquifer (Table 4.4) for a profile 15 km long. This recharge rate is slightly less than the 27 -36 cm/year predicted by the measured average specific discharge or for 35-47 cm/year predicted by the measured specific discharge at FA16_6 for a thickness of 30 and 40 m, respectively. The aquifer thickness nearest to the edge of the aquifer is described at FA16_6 in Chapter 3 between 30 and 40 m. These recharge estimates are lower than the available recharge estimated using the Degree Day method, consistent with some refreezing within the firn column to warm the unsaturated firn.

4.4.2.3 Recharge from Specific Yield and

Water Table Fluctuation Methods

Not all of the available meltwater recharges the aquifer as some of it is retained in the firn through refreezing. The portion of the total meltwater that recharges the aquifer can contribute to water level changes. In 2016, meltwater generation began around May 9th, when surface air temperatures rose above 0 ºC (Figure 4.3). The water level takes about a month to respond to the onset of melt. During this time, surface meltwater warms the firm temperature to 0 ºC. Once the unsaturated firn is at 0 ºC, surface meltwater can infiltrate and recharge the aquifer. At this time (June 22, 2016), the water level begins to rise. Meltwater recharges the aquifer until mid-September, when surface temperatures cool below 0 ºC, and meltwater generation ceases. The water level continues to rise after this date due to drainage of the unsaturated firn and lateral flow from upslope. These measurements do not account for any surface compaction. However, the measured

compaction is about 10 cm/year, which would not substantially alter the recharge results. The storativity of the firn aquifer, which is approximately equal to the specific yield in an unconfined aquifer, is shown in Table 4.5.

The water level rises nearly 4 m at FA15_2, and about 2 m at FA15_1, indicating that more recharge occurs at the lower elevation site, assuming that the specific yield is uniform. This is a reasonable assumption because the hydraulic conductivity is relatively homogeneous laterally. The total recharge ranges from ~2-80 cm/year (Table 4.6). These estimates are consistent with, or higher than the recharge estimates using the volumetric flow method. They are consistent with or lower than the meltwater available for infiltration estimated using the Degree-Day method. The melt generation and recharge results are summarized and compared in Figure 4.4.

The firn aquifer has a fairly high hydraulic conductivity. Consequently, we were not able to draw the water table down very much (~cm-m) during aquifer tests, and this weak perturbation of the system makes constraining the specific yield difficult. Still, it appears generally low, with an average of 0.04, excluding the 0.22 value as an outlier, and 0.06 including the 0.22 value. The recharge estimates using a specific yield of 0.05, result in recharge estimates between ~10-20 cm/year.

Overall, our best estimate for recharge to the aquifer is between ~10-30 cm/year, as shown in Figure 4.4. The estimates from the water level change are site specific, while the volumetric flow and dilution methods average over the length of the aquifer, and therefore provide a more general estimate. Further, the agreement between the specific discharge estimated from Darcy's law and the borehole dilution tests (Chapter 3) supports the recharge estimate using the volumetric flow method, using the mean hydraulic conductivity, and the recharge estimates from the borehole dilution method. Our best

estimate of the average recharge, which comes from the volumetric flow and borehole dilution methods, is 22 cm/year, with a lower 95% confidence limit of 13 cm/year and an upper 95% confidence limit of 33 cm/year. The average of all method averages (except for SUTRA-ICE) is 18 cm/year, with an upper 95% confidence interval of 28 cm/year and a lower 95% confidence interval of 8 cm/year. The specific discharge at the lowermost elevation site, FA16_6 results in a recharge rate of 35 cm/year. The different recharge estimates for FA15_1 and FA15_2 indicate that recharge varies spatially. The lower elevation site gets more recharge than the upper elevation site. The error on the average specific yield results in high errors on the mean recharge using the water level change method. However, each measurement included in these estimates has uncertainties and potential temporal and spatial variability, and so these initial recharge estimates require further work, especially refining measurements of specific yield, which contribute substantially to the uncertainty.

4.4.3 Aquifer Time Scales

4.4.3.1 Tritium

Tritium measurements of liquid water show that the water in the aquifer is modern (i.e., it recharged after ~1960). This indicates that water in the aquifer is not older than 1960. The measured ^{3}H concentration in firn and water samples is shown in Figure 4.5. In the spring at FA15_1, prior to the onset of melt, the tritium in the water is very similar to tritium in the surrounding firn, suggesting that the liquid water and firn are in isotopic equilibrium. During the summer, recharge from surface meltwater, which has a higher tritium concentration, causes the tritium in the liquid water to increase above the firn. Tritium in firn at depth has experienced longer periods of radioactive decay,

resulting in lower concentrations. This indicates that the aquifer is indeed recharged by surface meltwater infiltrating through the unsaturated firn above the aquifer.

The tritium at our field sites is similar to the winter time tritium at Summit at the time of deposition [*Fourré, E. et al.*, 2006]. Tritium concentration varies seasonally in precipitation at Summit, with higher values in the summer and lower values in the winter. Seasonal tritium variations occur due to seasonal atmospheric moisture source variation. We compare our samples to the winter time precipitation as our sites do not experience substantial summertime precipitation. After ~1990, the tritium signal becomes constant at ~9 TU. The tritium peak in Greenland was lower than other locations, so a return to background levels could happen faster in Greenland. If this is the case, dating shallow firn cores becomes simple as the concentration in firn only depends on the decay over time, and requires only a few samples. This relatively constant input, combined with tritium decay, results in the observed tritium decrease with depth. Our samples integrate ~ 30 cm of firn, and therefore contribute to smoothing of any seasonal signal. Additionally, meltwater percolation through the firn contributes to smoothing of the seasonal signals. Within the aquifer, all seasonal signals are smoothed out. Below the aquifer, the tritium concentration begins to increase as expected, approaching the bomb peak. Peak atmospheric tritium concentrations occurred in 1963 but our drill was not capable of reaching ice at this depth.

4.4.3.2 Chlorofluorocarbon Dating

CFC-11 concentrations and apparent recharge years for each site are shown in Figure 4.6. CFC-12 and CFC-113 were also measured, and show similar patterns. The concentration and apparent age generally decreases with depth. However, the water

appears to have recharged before the firn in which it now resides. To get this unusual age relationship, we suggest that the traditional CFC dating model does not apply to firn aquifers. Under the traditional CFC dating model, water equilibrates with the atmosphere at the land surface or in the atmosphere. The water maintains that equilibrium concentration after it recharges a terrestrial aquifer. However, in the case of a firn aquifer, CFCs are essentially excluded from ice. When the ice melts, it recharges the aquifer before atmospheric equilibration can occur, causing recharge to the aquifer to have very low CFC concentrations (and therefore older apparent recharge years). Once meltwater is in the aquifer, the only gas that can dissolve into the water is gas present in pore space. While this may increase the CFC concentration in the water, the volume is too small to raise the concentration in the water enough to appear even as old as the firn. Therefore, although CFC apparent recharge years cannot be determined, the unusually low gas concentrations suggest that recharge occurs quickly.

4.4.3.3 Fluorescein Dye

Fluorescent dye sprayed on the snow surface reached the aquifer in less than 2 days (Figure 4.7). It took us 49 hours to drill to the water table. The firn sample from the water table contained measurable amounts of fluorescent dye. The dye could have reached the water table in less time, but we did not drill fast enough to determine this. The variation in the concentration decrease with depth indicates that flow occurs along preferential flow paths. This is corroborated by piping identified in snow pits.

4.4.3.4 Mean Residence Time Estimates

Once water recharges the aquifer, it has a relatively short residence time between 4-35 years, for our best estimate of recharge rates between 10-30 cm/year and a range of porosities from 0.1-0.3 (Eq. 4.5), as summarized in Table 4.7. Recharge rates from measured and estimated specific discharge produces residence times between 9-43 years. Water in the aquifer will be fully replaced by new water in that time as the initial water discharges or freezes along the bottom of the aquifer. Higher porosities allow water to reside for longer within the aquifer. The low recharge rate of 2 cm/year is less likely, yet we included them to illustrate the significant effect the recharge rate has on water flow through the aquifer.

4.4.4 Conceptual Model

We can integrate the wide range of field data into a conceptual model of the firn aquifer (Figure 4.8). During the fall, winter, and spring, surface temperatures and incident radiation are too low to generate meltwater. Once summer warming and long days allow for meltwater generation, initial meltwater contributes to warming of the unsaturated firn overlying the firn aquifer. When the overlying firn finally becomes isothermal at 0 ºC, surface meltwater can rapidly recharge the aquifer. Recharge amount and timing estimates from a variety of methods all generally agree that recharge is ~5-30 cm/year, and that meltwater infiltrates to the aquifer rapidly. The portion of the surface melt that does not refreeze in the firn infiltrates through the ~10-20 m of unsaturated firn along preferential flow paths to recharge the aquifer in under 2 days. This recharge occurs too quickly for CFCs in the atmosphere to equilibrate with meltwater. However, tritium, as part of the water molecule, is conserved. The aquifer water comes to isotopic equilibrium

with the surrounding firn in the saturated zone. Recharge continues until snow surface temperatures cool and meltwater generation ceases. Recharge can continue until surface temperatures drop below 0 ºC and daylight hours decrease, at which point meltwater generation ceases. The remaining liquid in the unsaturated zone can still drain to the aquifer as it takes weeks-months for temperatures in the upper 10 m to decrease below 0 ºC.

Once meltwater has entered the saturated zone, it flows horizontally, governed by the hydraulic gradient and conductivity, to discharge zones (likely at crevasses between the aquifer and the edge of the ice sheet). Discharge may hydrofracture crevasses to the base of the ice sheet [*Mcnerney*, 2016; *Poinar et al.*, 2017]. The hydraulic conductivity of the aquifer is 2.7×10^{-4} m/s, similar to an unconsolidated sand or gravel. Recharge and horizontal flow contribute to changes in the water table. Changes to these parts of the system will alter flow through the firn. Increasing recharge, through warmer surface temperatures, or increasing hydraulic conductivity, by melting ice within the aquifer or developing fracture networks, will increase flow through the firn.

The temperature distribution within the ice sheet defines the bottom of the aquifer. The base occurs at the depth where the heat from the surface is inadequate to warm the ice to 0 ºC. Below this, subzero temperatures prevent liquid water from existing. Some refreezing occurs at the base of the aquifer, producing clear ice (Chapter 3).

4.4.5 SUTRA-ICE Simulations: 1D Sensitivity Analysis

Numerically simulating the conceptual model provides insight into major controls on the aquifer system. The most important input parameters are the surface temperature,

the residual total water saturation (minimum saturation of liquid plus ice), and the thickness of the capillary fringe (if it extends to the snow surface). The firn temperatures were only sensitive to the backbone fraction and freezing function parameters for the icy cases.

4.4.5.1 'Dry' Base Case

For the 'dry' base case and variations, the temperature distribution at the end of the winter in the unsaturated zone depends on the winter surface temperature and the unsaturated function. Still, these factors only influence the temperature distribution in the upper ~10 m of the firn column. Below that, the temperatures stay 0 ºC throughout the winter. Temperatures in the unsaturated zone do not substantially depend on the recharge rate, the backbone fraction, the relative permeability function, or the freezing function. Increasing or decreasing the winter surface temperature translates the temperature curve to warmer or cooler temperatures, but does not change the shape of the curve fundamentally. The depth that the firn column gets to 0 ºC changes by ~ 1 m for a winter temperature change between -10 and -20 ºC.

Increasing the residual water saturation in the unsaturated function decreases the depth that the firn goes to 0 ºC by several meters. Decreasing the residual liquid saturation increases the depth that the firn column goes to 0 ºC. Still even with a very low residual liquid saturation, the firn warms to 0 ºC at ~10 m depth. With a high (unrealistic, but illustrative) residual water saturation of 1, the firn warms to 0 ºC at a depth of 3 m. This is likely because the cold temperatures are insufficient to cool the increased mass (and heat) associated with a higher total water content.

Although highly unlikely to exist above the firn aquifer, a capillary fringe thicker

than ~10 m, obtained by increasing the pressure at residual saturation, also influences firn temperatures in the unsaturated zone from 0-10 m depth. A simulated capillary fringe that extends to the snow surface keeps the firn warmer than a capillary fringe that is below 10 m depth. This demonstrates how liquid in the pore spaces contributes to firn warming.

4.4.5.2 'Icy' Base Case

For the 'icy' base case (higher residual total water saturation), the temperature distribution at the end of the winter in the unsaturated zone depends on the winter surface temperature, the backbone fraction, the unsaturated function, and the freezing function. Similar to the 'dry' base case, these factors only influence temperatures in the upper ~10 m of the firn column. Temperatures in the unsaturated zone do not depend substantially on recharge rate or the relative permeability function for 'icy' simulations.

The winter surface temperature influences the temperature distribution in the unsaturated zone by shifting the temperature profile to warmer or cooler temperatures. Cooler surface temperatures (-20 ºC) cool the firn to 0 ºC at ~1 m deeper than warmer surface temperatures (-10 ºC). The firn column in the 'icy' base case stays warmer than the firn column in the 'dry' base case.

Increased backbone fraction (0.6) causes the firn temperature to cool slightly compared to the base case (backbone fraction = 0.4), although the temperature change is less than or equal to 1 ºC at a given depth. The cooler temperatures associated with a higher backbone fraction are likely due to reduced fraction of air, which is non-conductive in SUTRA-ICE. The increased ice from a higher backbone fraction conducts the cooler surface temperature to greater depths.

Increasing the total water residual saturation in the unsaturated function reduces

the depth where temperatures stay 0 ºC throughout the year. Similar to the dry base case, a capillary fringe thick enough to reach into the upper 0-10 m of the firn column warms the firn very slightly (up to 2 ºC). The warming is not uniform though, and occurs most significantly at ~3 m depth.

The firn temperatures depend on the freezing function because this function determines the amount of liquid in pore spaces. A higher minimum liquid saturation in the freezing function cools the firn, possibly because the liquid cannot freeze, so the cold temperatures cool the firn more, which has a higher thermal conductivity than water. Above a minimum liquid saturation of 0.5, the temperatures do not get cooler as the minimum liquid saturation increases. The maximum difference is 2 ºC at 5 m depth. Increasing *w* (the shape factor on the freezing function), which allows for a larger fraction of liquid to exist at cooler temperatures, reduces the depth that the firn warms to 0 ºC.

4.4.5.3 'Wet' Base Case

For the 'wet' base case (higher residual liquid saturation in the freezing function), the temperature distribution at the end of the winter in the unsaturated zone depends on the winter surface temperature and the unsaturated function. Similar to the 'dry' and 'icy' cases, these factors only influence temperatures in the upper ~10 m of the firn column. For the 'icy' cases, temperatures in the unsaturated zone do not depend on recharge rate, backbone fraction of ice, or the relative permeability function.

As in the 'dry' and 'icy' cases, the winter surface temperature influences the temperature distribution in the unsaturated zone by shifting the temperature profile to warmer or cooler temperatures. Cooler surface temperatures (-20 ºC) cool the firn to 0 ºC

at ~1 m deeper than warmer surface temperatures (-10 ºC).

Increasing the total water residual saturation in the unsaturated function reduces the depth where temperatures stay 0 ºC throughout the year. Similar to the 'dry' and 'icy' cases, having a capillary fringe thick enough to reach into the upper 0-10 m of the firn column warms the firn very slightly (up to ~2 ºC). The warming is not uniform though, and occurs most significantly at ~5 m depth.

4.4.5.4 Comparison to Measured Firn Temperatures

The temperatures simulated using the 'dry' and 'wet' base case most closely match the measured temperature profile (Figure 4.9). The temperatures are not sensitive to changes in recharge, backbone fraction, or relative permeability function. The largest temperature differences result from higher total water residual saturation, which causes the firn to be warmer than measured firn, and snow surface temperature in the winter, which can cause the firn temperatures to be either warmer or colder than the measured firn temperature. These simulations agree that the mean winter surface temperature is ~-13 ºC. The largest single temperature difference is 5 ºC, resulting from a total water residual saturation of 1, which means that the saturation of ice and liquid will always be 1. This is an unrealistic scenario. For a realistic scenario, the largest temperature difference occurs with the 'icy' base case, and a winter surface temperature of -5 ºC. In this scenario, the simulated firn is up to 4.9 ºC warmer than the measured firn.

4.4.6 SUTRA-ICE Simulations: 2D Simulation Results

Using the results from the 1D analysis, we expanded the model to simulate the aquifer in 2D to understand the effects of changing recharge on aquifer geometry. At

nearly steady state, the 2D simulations show that the aquifer expands upslope as recharge increases. When recharge decreases to the lower end of the recharge estimate (5 cm/year), the aquifer shrinks to nearly nonexistent (Figure 4.10). When recharge is 30 cm/year, the aquifer has approximately the same geometry as we observe. When recharge doubles to 60 cm/year, the water table rises to the snow surface at lower elevations. Increased recharge warms firn temperatures. Increased ice saturation occurs in areas where the aquifer exists, reflecting the increased densification relative to dry firn cores shown in *Koenig et al.* [2014]. Freezing also occurs along the base of the aquifer, and over time, the aquifer moves upwards. If this upward movement is balanced by the burial rate, which is not simulated in SUTRA-ICE, then the aquifer stays at the same depth. The presence of the aquifer causes ice saturation below the aquifer to increase.

These simulations do not have the variable surface temperature or recharge timing that happens in reality. As a result, they do not account for the heat and liquid that goes into warming the cold unsaturated zone in the spring. Future work should implement variable surface temperatures. However, as a first approximation of general conditions and behaviors of the aquifer, they provide validation of the conceptual model.

4.5 Conclusion

This paper describes a conceptual model of a firn aquifer located in southeast Greenland, upslope from Helheim Glacier. The conceptual model outlined in this paper and some of the firn aquifer properties can be integrated into more mathematically rigorous simulations to describe aquifer evolution and how it may change under different climate change scenarios.

For the aquifer to form initially, a certain volume of water was required to

infiltrate to depth. This volume had to contain enough heat to 1) warm the firn at depth to 0 ºC with enough water remaining in liquid form for the aquifer to persist until the next melt season. Melt rates have increased over time in Greenland. Therefore, recharge rates high enough to currently maintain an aquifer were probably adequate to initiate formation. The firn warming process may have taken several melt seasons. Once this initial heat barrier is overcome, the aquifer can persist for as long as the heat in the liquid allows the water to stay in liquid form. The heat in the liquid is replenished annually by new recharge. The residence time of water in the aquifer, with an average thickness of 11.5 m, porosity of 0.2 and recharge between 10-30 cm/year, is ~8-23 years, suggesting that the water in the aquifer is fully replaced in that time. Annual recharge is critical to aquifer persistence. Without it, the aquifer can refreeze from the bottom up. To maintain a firn aquifer at our field site, ~10-30 cm of meltwater per year are required to recharge the aquifer. This is not that much water, and suggests that even slight warming could allow for widespread aquifer expansion at locations where adequate pore space exists.

The bottom of the aquifer is thermodynamically controlled, and burial of warm ice alters the thermal regime of the ice sheet in areas where the aquifer exists. Once the aquifer exists, the ~surface (the base of the aquifer) temperature boundary condition of the ice sheet is warmed from ~the mean annual temperature to 0 ºC. This is a substantial alteration of the shallow temperature profile of the ice sheet and may have important implications for historical records of environmental conditions and their preservation, in addition to alteration of ice rheology in the shallow ice sheet.

This conceptual model can generally be simulated numerically, indicating that we understand and have characterized many of the major system drivers and parameters. Still, much remains unknown about the effect meltwater has on firn metamorphism,

aquifer expansion rates, glacier dynamics, or fate of water upon discharge from the aquifer. Further investigation of tritium in precipitation at this site would aid firn dating. Additionally, further research is needed to develop our understanding of the impacts discharging water may have on ice dynamics and sea level rise. As surface melt increases under a warming climate, the aquifer will likely grow, leading to further alteration of the thermal regime of the ice sheet, while increased discharge could impact sea level rise.

Table 4.1. SUTRA-ICE model parameters. Table showing general model specifications, boundary conditions, and physical parameters used in 1D and 2D simulations.

Description	**1D Simulation Value**	**2D Simulation Value**
Finite element mesh specifications		
Type	Fishnet	Fishnet
Element height (m)	0.5	0.5
Element width (m)	10	100
Boundary Conditions		
Specified pressure	294300 Pa (water table at 20 m depth)	Hydrostatic - right edge
Specified temperature (ºC)	0, -1 ºC on base	-1 ºC on base
Porosity	0.6	0.6
Permeability (m^2)	$3x10^{-10}$ to $3x10^{-12}$	$6x10^{-10}$ to $6x10^{-12}$
General physical properties		
Acceleration of gravity (m/s^2)	-9.81	-9.81
Fluid specific heat (J/kg)	4182	4182
Ice specific heat (J/kg)	2108	2108
Fluid thermal conductivity (J/s m ºC)	0.6	0.6
Ice thermal conductivity (J/s m ºC)	2.14	2.14
Fluid density (kg/m^3)	1000	1000
Ice density (kg/m^3)	920	920
Latent heat of fusion (J/kg)	$3.34x10^{-5}$	$3.34x10^{-5}$
Fluid compressibility ($kg/(ms^2)$)	0	0
Matrix compressibility ($kg/(ms^2)$)	0	0
Longitudinal dispersivity (max and min direction) (m)	0.5, 0.5	10 & 100, 1
Transverse dispersivity (max and min direction) (m)	0.5, 0.5	0.01, 0.01

Table 4.2. Sensitivity analysis model inputs and parameters. Table showing model inputs and parameters for sensitivity analysis and used in simulations.

Input or parameter		Dry Base case	Icy base case	Wet base case	High	Medium	Low	Very low
Winter surface temp (ºC)		-13	-13	-13	-5	-10	-15	-20
Infiltration (total added, cm/yr)		39	39	39	100	-	5	-
Recharge rate (kg/m^2*sec)		0.0001	0.0001	0.000100	0.000250	0.000049	0.000011	
Backbone fraction		0.4	0.4	0.4	0.6	0.5	0.3	
Total water saturation (piecewise linear)	**Residual total water saturation**	0.01	0.2	0.01	1	0.5	0.1	
	Pressure at residual liquid saturation	5000	5000	5000	196200	100000	10000	1000
	(thickness of capillary fringe)	0.5	0.5	0.5	20	10	1	0.1
Relative permeability function (linear)	**Saturation at which minimum relative permeability occurs**	0.01	0.01	0.01	1	0.5	0.1	
	Relative permeability at residual liquid saturation	0.01	0.01	0.01	0.05	0.001	0.0001	
Liquid water saturation (exponential)	**Minimum liquid saturation**	0.01	0.01	0.2	1	0.5	0.1	
	Exponential model parameter (w>0)	0.05	0.05	0.05	1	0.5	0.01	

Table 4.3. Melt available to recharge the aquifer.

Degree Day Factor (Tref = 273.15K) (mm/d K)	Melt (cm)			Degree Day Factor (Tref = 268K) (mm/d K)	Melt (cm)		
	2014	2015	2016		2014	2015	2016
8	62	31	39	**1**	45	31	32
10	78	39	48	**1.5**	68	46	47
20	156	79	97	**2**	90	61	63
30	234	118	145	**2.5**	113	77	79

Table 4.4. Recharge estimates using the volumetric flow method.

	Aquifer thickness (m)	Hydraulic conductivity (m/s)		
		Lower bound of 95% confidence interval	Mean	Upper bound of 95% confidence interval
		2.5E-04	2.7x10-4	2.9E-04
Recharge rate (cm/year)	30	16	17	18
	40	21	23	24

Table 4.5. Specific yield at FA16_5 and FA16_6.

Site		Well	Specific yield
FA16_4	Test 1	Observation 1	0.01
	Test 2	Observation 1	0.01
FA16_6	Test 1	Pumping	0.03
		Observation 1	0.22
		Observation 2	0.06
	Test 2	Pumping	0.06
		Observation 1	0.05
		Observation 2	0.04

Table 4.6. Recharge rates from water level rise. Water level change over the 82-day period of meltwater recharge to the aquifer, total recharge, and recharge rate for a range of specific yields at FA15_1 and FA15_2. Shading indicates best estimate. The water level began to rise on June 22, 2016. The last day of substantial melt was September 12, 2016. After this day, air temperatures were too cold for melt to occur.

		Specific yield				
		0.01	**0.05**	**0.10**	**0.20**	**Water level rise (m)**
FA15_1	**Recharge rate (cm/day)**	0.0	0.1	0.3	0.5	2.1
	Annual Recharge (cm/y)	2	11	21	42	
FA15_2	**Recharge rate (cm/day)**	0.0	0.2	0.5	0.9	3.9
	Annual Recharge (cm/y)	4	19	39	77	

Table 4.7. Residence times for a range of porosity and recharge rate estimates. Shading indicates best estimate values, assuming porosity is 0.2, which agrees with *Koenig et al.* [2014] and *Montgomery et al*.[2017].

	Residence Time (years)		
Recharge Rate (cm/year)	**Porosity**		
	0.1	**0.2**	**0.3**
2	58	115	173
5	23	46	69
7	16	33	49
10	12	23	35
15	8	15	23
20	6	12	17
30	4	8	12
80	1	3	4

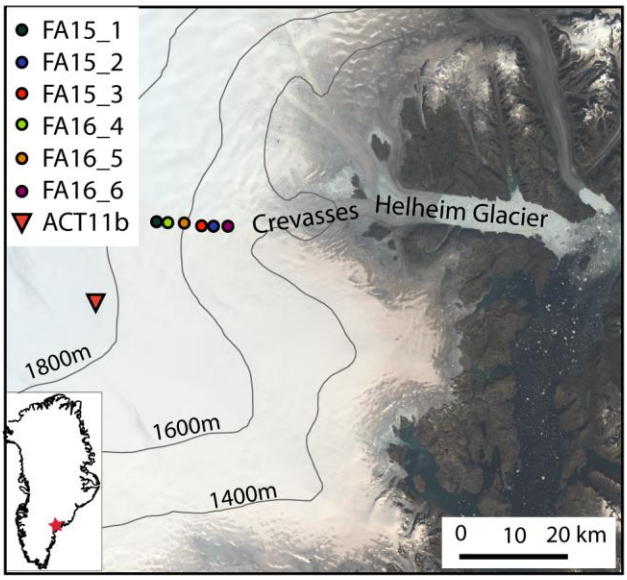

Figure 4.1.Site map. Landsat 8 composite image (August 21, 2014) showing field sites in southeast Greenland visited in April, July, and August 2015 and July and August, 2016, and location of ACT11b core. Elevation contours from Cryosat-2 DEM [*Helm et al.*, 2014].

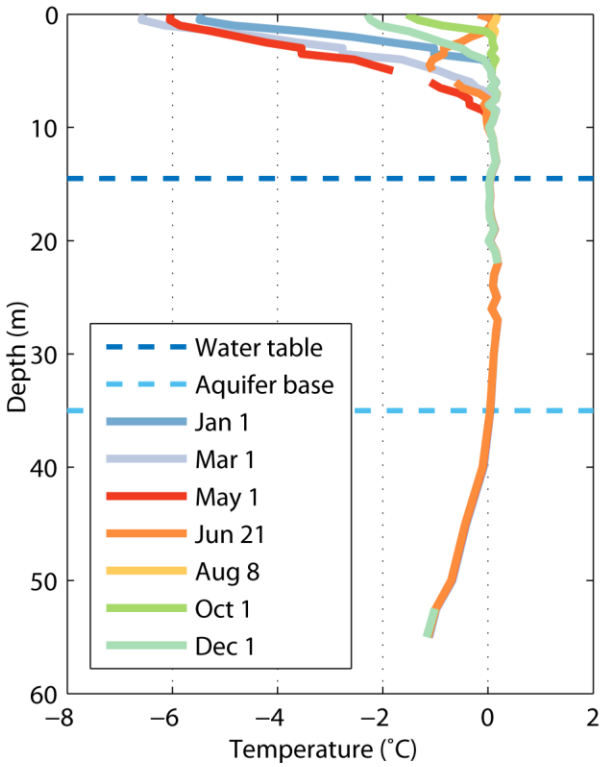

Figure 4.2. Firn temperature profile from January – December 2016 at FA15_2. Depths refer to sensor depth at installation in July 2016. Accumulation and burial means that the depths shown are shallower by ~1-2 m. Data from the sensors from ~22m-55m were lost after June 15.

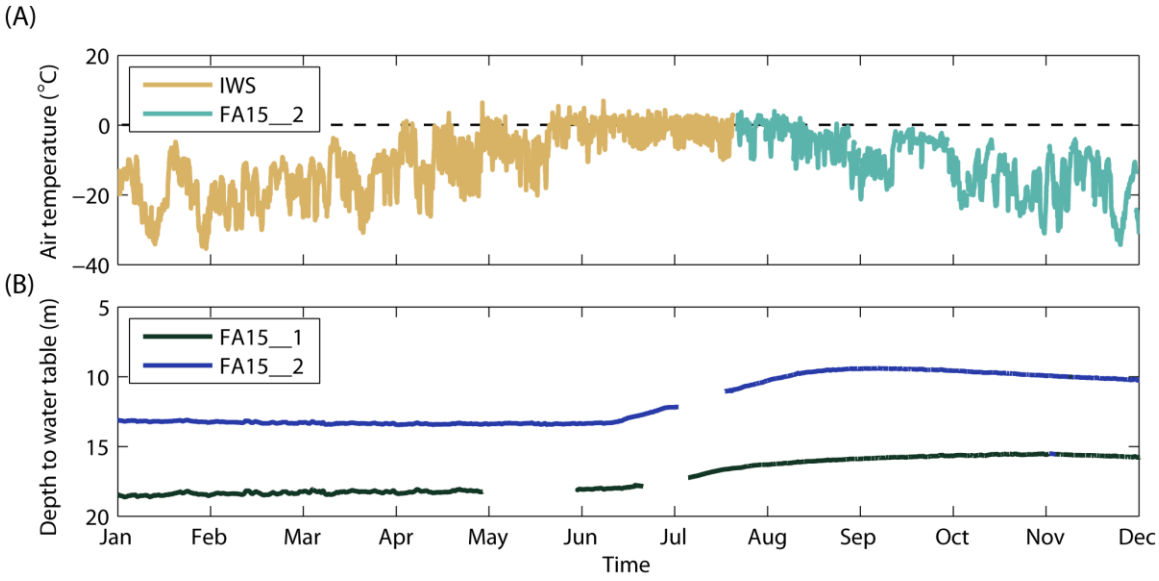

Figure 4.3.Air temperatures and water levels. Air temperature from the (A) and depth to the water table (B) in 2016.

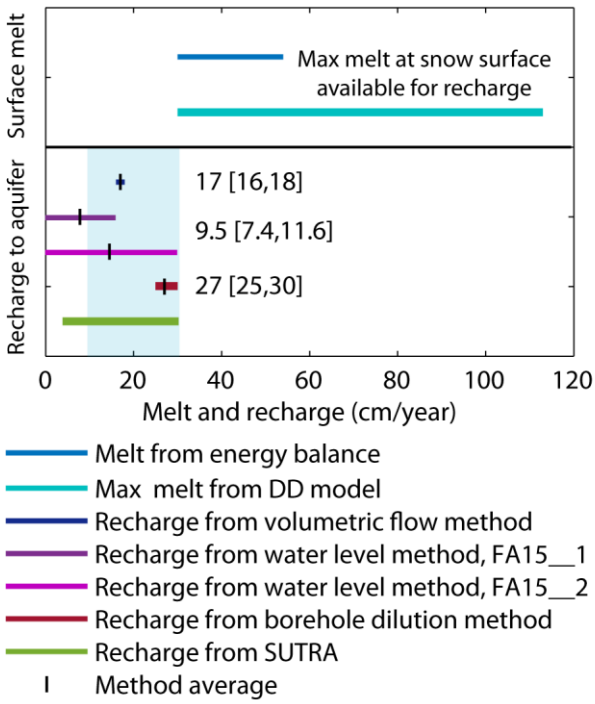

Figure 4.4. Comparison of melt and recharge estimates. Comparison of surface melt calculated from an energy balance, total melt generated from degree day modeling (using reference temperature of 268K), and average and 95% confidence interval estimates of recharge to the aquifer the volumetric flow, water level, borehole dilution methods, and range of plausible recharge estimates from SUTRA-ICE modeling. Blue shading indicates our best estimate of recharge, ~10-30 cm/year. The total available meltwater from the degree day model is the maximum possible water that could recharge the aquifer. It is generally greater than the recharge estimates due to retention of meltwater in the unsaturated zone through freezing. Water that freezes in the unsaturated zone does not contribute to recharge of the aquifer.

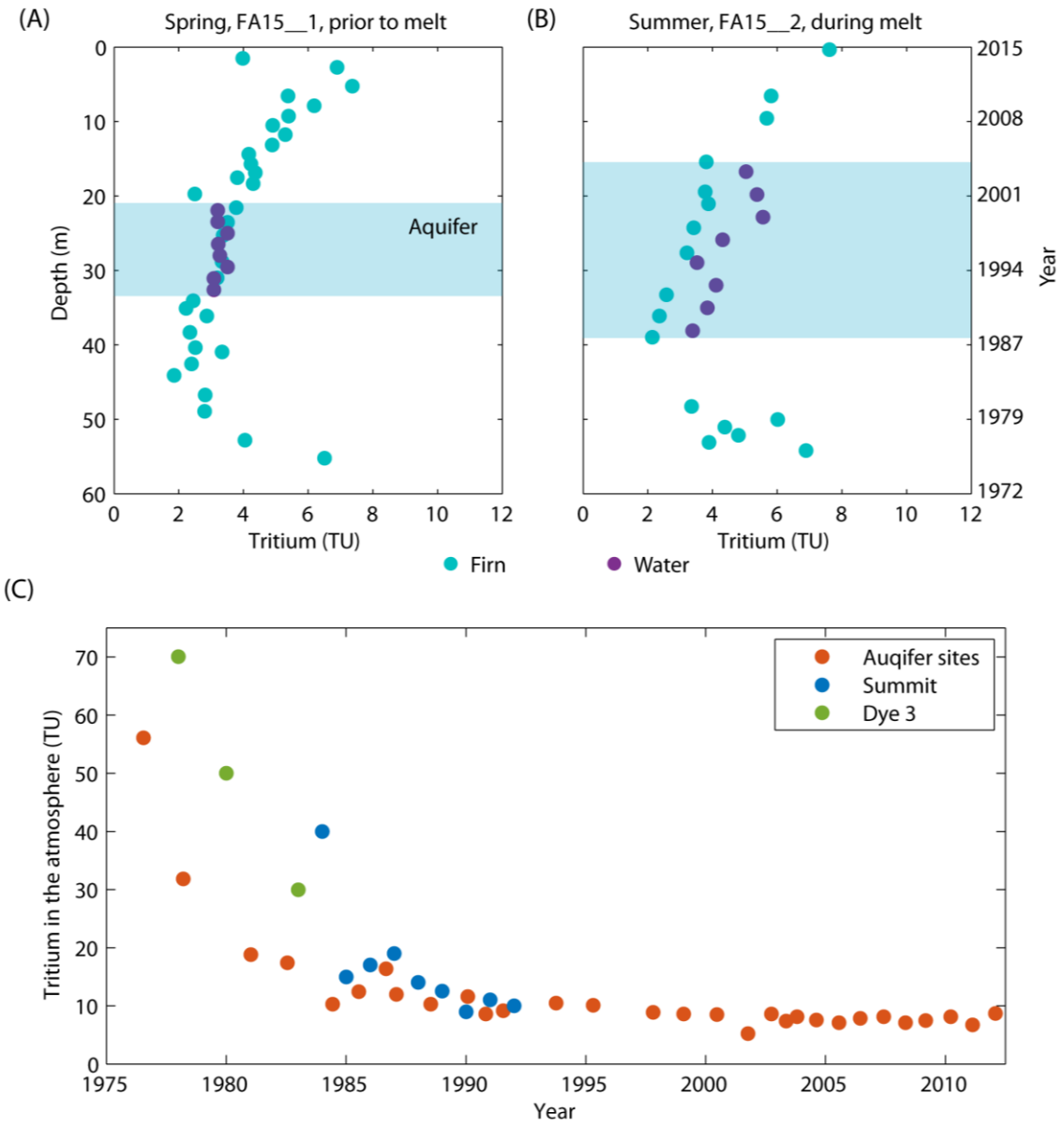

Figure 4.5. Tritium measurements. Tritium measured in firn and water at depth in the spring (A) and summer (B), and tritium at the time of deposition (C) calculated from firn samples at our field sites compared to tritium in the atmosphere at Summit and Dye 3, Greenland from *Fourré et al.* [2006]. Core depth model developed from ACT-11b core. Over the winter, tritium in water equilibrates with tritium in firn. The tritium in liquid water increases in the summer due to recharge of surface meltwater.

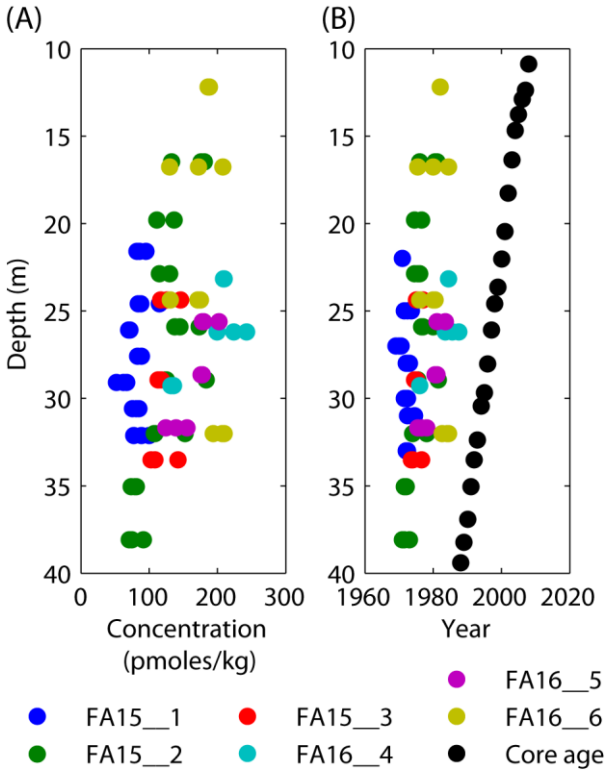

Figure 4.6.CFC-11 concentrations and model ages. Concentration of CFC-11 (A) and apparent recharge year compared to firn core age model from ACT-11b (B) for all sites.

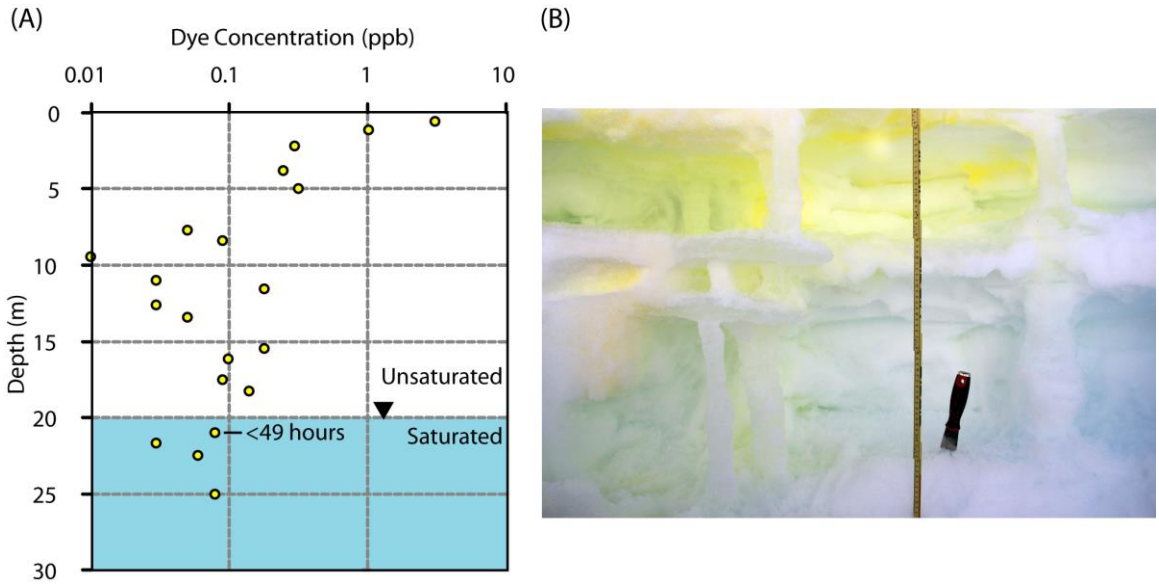

Figure 4.7. Dye infiltration through firn. Plot showing dye concentration at depth within the unsaturated and saturated firn (A) and photo of piping observed in the wall of a snow pit. Dye was present when we drilled into the saturated zone after 49 hours. The yellow dye in the photo was sprayed on the snow surface. Measuring tape is in cm. Pipes are ~5-30 cm tall and 5 cm diameter. Photo credit: Clément Miège, 2016.

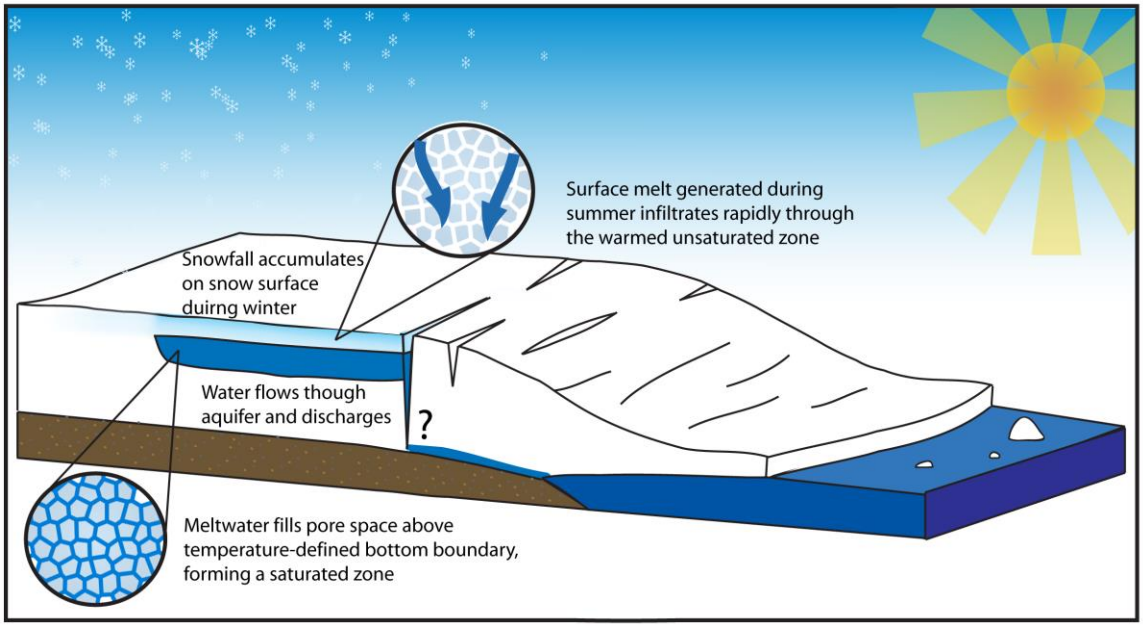

Figure 4.8. Conceptual model of the firn aquifer. Snow accumulates during the winter on the surface of the ice sheet. In the summer, the warm temperatures and intense solar radiation allow some of the surface snow to melt, which warms the firn pack as it infiltrates and refreezes until the unsaturated zone is 0 ºC. At this point, surface melt can infiltrate to depth and recharge the aquifer. The temperature of the ice sheet controls the depth of the base of the aquifer. The base of the aquifer occurs where the cold of the interior of the ice is sufficient to freeze the liquid water within the aquifer. Water flows relatively quickly through the aquifer to discharge, likely into crevasses near the edge of the ice sheet. We do not know what happens to the water after it discharges.

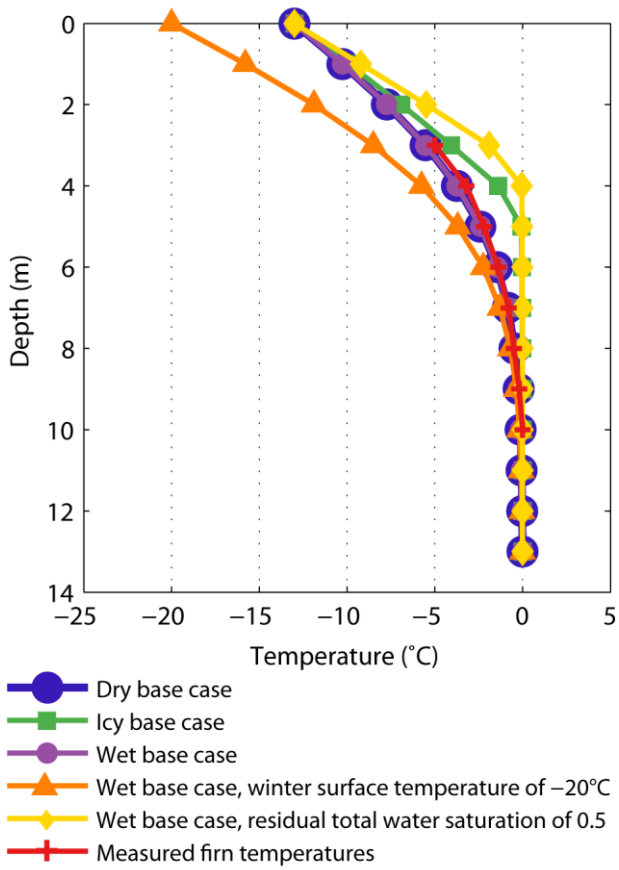

Figure 4.9. Measured and simulated firn temperatures. Measured and simulated firn temperatures for the 'icy', 'wet', and 'dry' base cases, the 'wet' base case with surface temperatures = -20 ºC and 'wet' base case with residual total water = 0.5.

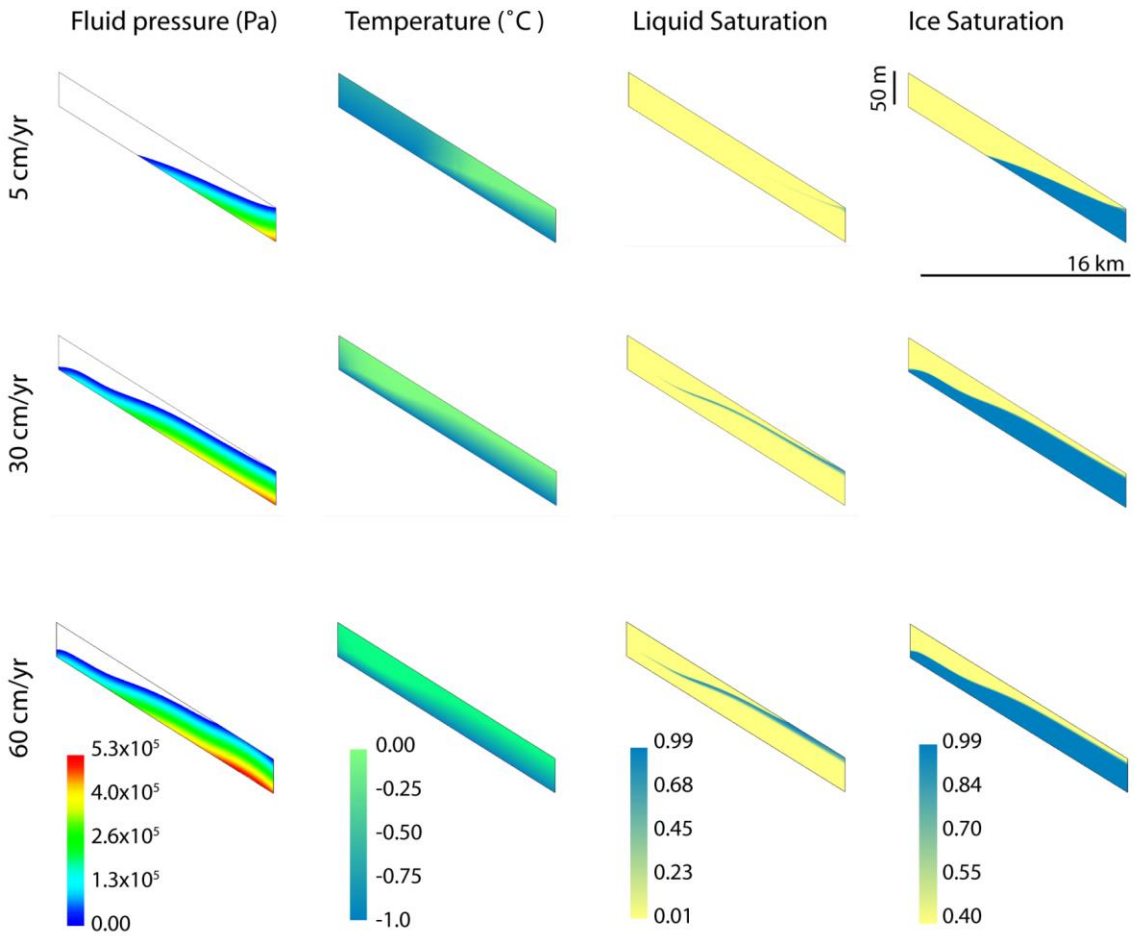

Figure 4.10. Aquifer changes under a range of recharge rates. Effects of changing the recharge rate to the aquifer on fluid pressure, firn temperature, liquid saturation, and ice saturation. The water table occurs where the fluid pressure is zero (shown in blue). Liquid saturation is the volume of liquid per volume of pore space. Ice saturation is the volume of ice per volume of pore space.

CHAPTER 5

CONCLUSION

The Arctic is changing rapidly as a result of global climate change. Greenland is losing ~270 Gt/year of ice [*Richter-Menge et al.*, 2016]. To reduce uncertainty in predictions of future ice mass loss and associated sea level rise, we need to accurately characterize current mass balance processes on glacier and ice sheets. The discovery of firn aquifers highlighted significant gaps in our understanding of those processes particularly in Greenland and increasingly on Antarctic ice shelves [*Lenaerts et al.*, 2016; *Bell et al.*, 2017]. However, through our current research, we are developing a more comprehensive assessment of how the ice sheet melts.

In this dissertation, I describe the physical and hydraulic characteristics of a firn aquifer in southeast Greenland. In Chapter 2, I describe the hydraulic parameters of the firn aquifer. Hydraulic conductivity decreases slightly with depth through the aquifer but does not vary greatly laterally. In Chapter 3, I describe evidence that water flows through the aquifer. The firn aquifer does not permanently store meltwater. I also describe a salt mass balance method to show that the aquifer formed no earlier than the late 1980s, and is therefore likely a result of widespread warming of the Arctic associated with global climate change. In Chapter 4, I combine further field observations with the findings of Chapter 2 and 3, in addition to aquifer geometry described in *Forster et al.* [2014], *Koenig et al.* [2014], *Miege et al.* [2016] and *Montgomery et al.* [2017] to develop and

numerically validate a conceptual model of the firn aquifer. Using this model, I show that increased recharge, through increased melt associated with climate change, increases aquifer extent inland.

Firn aquifers contain substantial volumes of meltwater, leading to uncertainty in estimates of meltwater runoff to the ocean. If they connect to the subglacial hydrologic system, firn aquifers may also influence ice mass loss by increasing ice discharge to the ocean. I have shown that the firn aquifer upstream from Helheim Glacier does not permanently store substantial volumes of water. Instead, water drains, seemingly continuously, from the aquifer, likely into downstream crevasses. The major question remains however, of what happens to the water once it leaves the aquifer. *Poinar et al.* [2017] suggest that this discharging meltwater can hydrofracture crevasses to the base of the ice sheet, and that minimal refreezing within the crevasses occurs. Basal lubrication of the ice sheet can increase ice velocity [*Zwally*, 2002], which can increase ice discharge into the ocean, thereby increasing mass loss. In this way, firn aquifers may increase ice mass loss through both promoting meltwater loss to the ocean and ice discharge to the ocean.

Still, uncertainty remains regarding the fate of discharging firn aquifer water. This water may contribute to crevasse fracture propagation to the base of the ice sheet. *Poinar et al.* [2017] show that aquifer water can cause hydrofracturing in under 180 days. However, the discharge they use in their analysis is larger (6,000 – 15,000 m^2) than we calculate from flow measurements. Although they use flux units of m^2, if we assume that they correspond to a unit width of aquifer, we can compare them to the flow of meltwater measured through the aquifer. Using the measured mean specific discharge of 4.3×10^{-6} m/s and a 10m thick aquifer, we calculate a flux of 1356 m^3/year. Using the total

discharge flowing through the aquifer at site FA16_6 ($1.7x10^{-4}$ m^2/s) flowing through a unit thickness of aquifer, we calculate a flux of 5316 m^3/year. We also do not know if discharge is constant or variable over time. However, the seasonality of recharge suggests that discharge should also vary seasonally. To improve our understanding of the impacts of firn aquifers on ice sheet mass balance and sea level rise, we need direct evidence of meltwater discharge to crevasses, hydrofracture occurrence, or meltwater reaching the ocean. We also need more research to identify connections between aquifer discharge and ice velocity.

APPENDIX A

SUPPLEMENTARY METHODS

A.1 Slug tests: Hvorslev Method

According to the Hvorslev method, the water level response to an instantaneous change in water level can be described as:

$$\ln(H_o) - \ln(h) = \frac{2KLt}{r_c^2 ln\left(\frac{L}{2r_{we}} + \sqrt{1+\left(\frac{L}{2r_{we}}\right)^2}\right)} \quad \text{(A1)}$$

where

$$r_{we} = r_w\sqrt{K_z/K_r} \quad \text{(A2)}$$

and h (length) is displacement at time t, H_o is the initial displacement (length), K_r is the radial hydraulic conductivity (length/time), K_z is the vertical hydraulic conductivity (length/time), L is the length of the screened interval (length), r_c is the casing radius (length), r_w is the well radius (length), r_{we} is the equivalent well radius (length), and t is time (Figure 2.3). When the screened interval of the piezometer contacts an impermeable boundary (e.g., impermeable ice thicker than the screened interval), the term r_{we} is used instead of $2r_{we}$. The equivalent well radius can be used for a partially penetrating well in

an anisotropic aquifer [*Zlotnik*, 1994]. However, for this study, the aquifer was assumed to be isotropic (i.e., $K_z = K_r$) and so $r_{we} = r_w$.

A.2 Slug tests: Bouwer and Rice method

The empirical relationship describing the water level response to an instantaneous change in water level developed by Bouwer and Rice is:

$$\ln(H_o) - \ln(h) = \frac{2KLt}{r_c^2 ln\left(\frac{R_e}{r_{we}}\right)} \quad \text{(A3)}$$

where h is displacement at time t, H_o is the initial displacement, K is the hydraulic conductivity, L is the length of the screened interval, r_c is the casing radius, R_e is the effective radius over which a water level change occurs , r_w is the well radius, r_{we} is the equivalent well radius, and t is time. R_e depends on the geometry of the flow system and is determined by the well length below the water table, screened interval length, saturated thickness, and well radius (for further description, see *Bouwer and Rice* [1976]).

A.3 Aquifer Test: Theis Solution

The Theis solution for the drawdown distribution surrounding a well at any time is:

$$s = \frac{Q}{4\pi T} W(u) \quad \text{(A4)}$$

where

$$W(u) = \int_{u}^{\infty} \frac{1}{u'} e^{-u'} du' \quad \text{(A5)}$$

and

$$u = \frac{r^2 S}{4Tt} \quad \text{(A6)}$$

and Q is the pumping rate (length^3/time), r is the radial distance (length), s is drawdown (length), S is storativity (dimensionless), t is time, and T is transmissivity (length^2/time) (Figure 2.3).

APPENDIX B

SUPPLEMENTARY TABLE

Table B1. Hydraulic conductivity estimates. Hydraulic conductivity estimates from the Hvorselv and Bouwer and Rice analysis method of repeated tests at each depth at each site.

			Hvorslev Method		Bower Rice Method	
Site	**Depth (m)**	**Test #**	**K (m/s)**	**Standard Error**	**K (m/s)**	**Standard Error**
FA15_1	21.9	1	7.3E-04	2.3E-05	5.6E-04	1.8E-05
FA15_1	21.9	2	7.1E-04	2.2E-05	5.5E-04	1.7E-05
FA15_1	22.3	1	4.4E-04	1.8E-05	3.4E-04	1.4E-05
FA15_1	22.3	2	4.9E-04	2.1E-05	3.8E-04	1.6E-05
FA15_1	22.6	1	4.0E-04	1.7E-05	3.1E-04	1.3E-05
FA15_1	22.6	2	3.9E-04	1.4E-05	3.1E-04	1.1E-05
FA15_1	22.9	1	3.6E-04	1.2E-05	2.9E-04	9.7E-06
FA15_1	22.9	2	3.7E-04	9.5E-06	2.9E-04	7.6E-06
FA15_1	23.2	1	3.8E-04	1.4E-05	3.1E-04	1.1E-05
FA15_1	23.2	2	3.3E-04	9.5E-06	2.7E-04	7.7E-06
FA15_1	23.5	1	3.2E-04	9.9E-06	2.6E-04	8.0E-06
FA15_1	23.5	2	3.1E-04	8.0E-06	2.5E-04	6.5E-06
FA15_1	23.8	1	2.9E-04	1.2E-05	2.4E-04	9.6E-06
FA15_1	23.8	2	3.0E-04	1.0E-05	2.4E-04	8.2E-06
FA15_1	24.1	1	2.8E-04	1.1E-05	2.3E-04	9.0E-06
FA15_1	24.1	2	2.8E-04	1.1E-05	2.3E-04	9.0E-06
FA15_1	24.4	1	2.7E-04	1.0E-05	2.3E-04	8.6E-06
FA15_1	24.4	2	2.7E-04	8.3E-06	2.2E-04	6.9E-06
FA15_1	24.7	1	2.6E-04	4.7E-06	2.2E-04	3.9E-06
FA15_1	24.7	2	2.6E-04	7.2E-06	2.2E-04	6.0E-06
FA15_1	25.0	1	2.5E-04	1.3E-05	2.1E-04	1.1E-05
FA15_1	25.0	2	2.5E-04	1.3E-05	2.1E-04	1.1E-05
FA15_1	25.3	1	1.7E-04	3.3E-06	1.4E-04	3.0E-06
FA15_1	25.3	2	1.8E-04	3.8E-06	1.5E-04	3.2E-06
FA15_1	25.6	1	2.3E-04	1.2E-05	2.0E-04	1.0E-05
FA15_1	25.6	2	2.3E-04	8.5E-06	2.0E-04	7.2E-06

Table B1 continued

Site	Depth (m)	Test #	Hvorslev Method K (m/s)	Bower Rice Method Standard Error	K (m/s)	Standard Error
FA15_1	25.9	2	2.3E-04	9.6E-06	2.0E-04	8.1E-06
FA15_1	26.2	1	2.3E-04	8.5E-06	2.0E-04	7.2E-06
FA15_1	26.5	1	2.2E-04	8.8E-06	1.9E-04	7.5E-06
FA15_1	26.5	2	2.1E-04	5.9E-06	1.8E-04	5.0E-06
FA15_1	26.8	1	2.1E-04	4.3E-06	1.8E-04	3.7E-06
FA15_1	26.8	2	2.1E-04	6.9E-06	1.8E-04	5.9E-06
FA15_1	27.1	1	2.1E-04	9.6E-06	1.8E-04	8.3E-06
FA15_1	27.1	2	2.2E-04	8.5E-06	1.9E-04	7.3E-06
FA15_1	27.4	1	1.9E-04	5.7E-06	1.7E-04	5.0E-06
FA15_1	27.4	2	2.0E-04	5.5E-06	1.7E-04	4.8E-06
FA15_1	27.7	1	2.1E-04	5.0E-06	1.8E-04	4.4E-06
FA15_1	27.7	2	2.0E-04	4.9E-06	1.8E-04	4.3E-06
FA15_1	28.0	1	1.9E-04	3.0E-06	1.6E-04	2.6E-06
FA15_1	28.0	2	2.0E-04	4.8E-06	1.7E-04	4.2E-06
FA15_1	28.3	1	1.9E-04	4.4E-06	1.7E-04	3.8E-06
FA15_1	28.3	2	1.9E-04	5.1E-06	1.7E-04	4.4E-06
FA15_1	28.7	1	2.0E-04	5.7E-06	1.7E-04	5.0E-06
FA15_1	28.7	2	1.9E-04	6.1E-06	1.7E-04	5.4E-06
FA15_1	29.0	1	1.8E-04	6.0E-06	1.6E-04	5.3E-06
FA15_1	29.0	2	1.9E-04	5.9E-06	1.7E-04	5.2E-06
FA15_1	29.3	1	1.9E-04	5.7E-06	1.7E-04	5.1E-06
FA15_1	29.3	2	1.9E-04	4.2E-06	1.7E-04	3.7E-06
FA15_1	29.6	1	1.9E-04	5.4E-06	1.7E-04	4.8E-06
FA15_1	29.6	2	1.8E-04	5.3E-06	1.6E-04	4.7E-06
FA15_1	29.9	1	2.0E-04	8.4E-06	1.8E-04	7.6E-06
FA15_1	29.9	2	1.9E-04	8.5E-06	1.7E-04	7.6E-06
FA15_1	30.2	1	1.9E-04	6.4E-06	1.7E-04	5.7E-06
FA15_1	30.2	2	1.9E-04	6.4E-06	1.7E-04	5.8E-06
FA15_1	30.2	3	1.9E-04	5.5E-06	1.7E-04	4.9E-06
FA15_1	30.5	1	1.9E-04	5.6E-06	1.7E-04	5.1E-06
FA15_1	30.5	2	1.9E-04	5.8E-06	1.7E-04	5.3E-06
FA15_1	30.8	1	1.8E-04	6.1E-06	1.7E-04	5.6E-06
FA15_1	30.8	2	1.8E-04	5.4E-06	1.6E-04	5.0E-06
FA15_1	31.1	1	1.8E-04	5.3E-06	1.6E-04	4.9E-06
FA15_1	31.1	2	1.8E-04	5.8E-06	1.7E-04	5.3E-06
FA15_1	31.4	1	2.0E-04	8.7E-06	1.8E-04	8.0E-06
FA15_1	31.4	2	1.9E-04	7.4E-06	1.8E-04	6.9E-06
FA15_1	31.7	1	1.9E-04	8.3E-08	1.8E-04	7.8E-06

Table B1 continued

Site	Depth (m)	Test #	Hvorslev Method K (m/s)	Bower Rice Method Standard Error	K (m/s)	Standard Error
FA15_1	32.3	2	1.9E-04	6.9E-06	1.8E-04	6.6E-06
FA15_1	32.6	1	1.8E-04	6.4E-06	1.8E-04	6.2E-06
FA15_1	32.6	2	1.8E-04	6.3E-06	1.7E-04	6.1E-06
FA15_1	32.9	1	5.8E-05	7.4E-07	5.7E-05	7.3E-07
FA15_1	32.9	2	4.8E-05	5.2E-07	4.7E-05	5.1E-07
FA15_1	33.2	1	2.5E-04	1.1E-05	2.5E-04	1.1E-05
FA15_1	33.2	2	2.5E-04	1.0E-05	2.5E-04	1.0E-05
FA15_1	33.5	1	3.5E-04	1.5E-05	3.7E-04	1.6E-05
FA15_1	33.5	2	3.4E-04	1.5E-05	3.6E-04	1.6E-05
FA15_1	33.8	1	3.9E-04	1.6E-05	4.3E-04	1.8E-05
FA15_1	33.8	2	3.7E-04	1.2E-05	4.1E-04	1.3E-05
FA15_1	33.8	3	3.8E-04	1.6E-05	4.2E-04	1.8E-05
FA15_1	34.1	1	3.8E-04	1.5E-05	4.2E-04	1.6E-05
FA15_1	34.1	2	3.6E-04	1.4E-05	4.0E-04	1.6E-05
FA15_1	34.1	3	4.6E-04	1.9E-05	5.1E-04	2.1E-05
FA15_1	34.1	4	4.3E-04	2.0E-05	4.8E-04	2.3E-05
FA15_1	35.1	1	3.6E-04	1.3E-05	4.0E-04	1.4E-05
FA15_1	35.1	2	3.8E-04	1.4E-05	4.2E-04	1.6E-05
FA15_1	35.7	1	3.1E-04	1.1E-05	3.4E-04	1.2E-05
FA15_1	35.7	2	3.2E-04	1.2E-05	3.6E-04	1.3E-05
FA15_2	19.8	1	4.2E-04	1.7E-05	3.5E-04	1.5E-05
FA15_2	19.8	2	4.6E-04	2.0E-05	3.8E-04	1.7E-05
FA15_2	19.8	3	4.7E-04	2.2E-05	4.0E-04	1.8E-05
FA15_2	19.8	4	4.2E-04	2.0E-05	3.5E-04	1.7E-05
FA15_2	22.9	1	4.0E-04	1.8E-05	3.5E-04	1.5E-05
FA15_2	22.9	2	3.8E-04	1.4E-05	3.3E-04	1.2E-05
FA15_2	22.9	3	4.0E-04	1.7E-05	3.4E-04	1.5E-05
FA15_2	22.9	4	3.7E-04	1.3E-05	3.2E-04	1.2E-05
FA15_2	25.9	1	3.8E-04	1.5E-05	3.4E-04	1.3E-05
FA15_2	25.9	2	3.9E-04	1.9E-05	3.5E-04	1.7E-05
FA15_2	25.9	3	3.8E-04	1.7E-05	3.4E-04	1.5E-05
FA15_2	29.0	1	3.5E-04	1.9E-05	3.1E-04	1.7E-05
FA15_2	29.0	2	3.4E-04	1.5E-05	3.1E-04	1.4E-05
FA15_2	29.0	3	3.4E-04	1.6E-05	3.1E-04	1.4E-05
FA15_2	32.0	1	3.4E-04	1.8E-05	3.2E-04	1.7E-05
FA15_2	32.0	2	3.3E-04	1.7E-05	3.1E-04	1.6E-05
FA15_2	32.0	3	3.4E-04	1.5E-05	3.3E-04	1.4E-05

Table B1 continued

Site	Depth (m)	Test #	Hvorslev Method K (m/s)	Bower Rice Method Standard Error	K (m/s)	Standard Error
FA15_2	35.1	3	3.2E-04	1.7E-05	3.7E-04	1.9E-05
FA15_2	38.1	1	3.7E-04	1.8E-05	4.3E-04	2.1E-05
FA15_2	38.1	2	3.9E-04	2.0E-05	4.5E-04	2.3E-05
FA15_2	38.1	3	3.7E-04	1.8E-05	4.3E-04	2.1E-05
FA15_3	24.4	1	4.7E-04	2.4E-05	3.9E-04	2.0E-05
FA15_3	24.4	2	4.9E-04	2.1E-05	4.1E-04	1.8E-05
FA15_3	24.4	3	4.5E-04	1.9E-05	3.8E-04	1.6E-05
FA15_3	29.0	1	5.2E-04	2.8E-05	5.4E-04	2.8E-05
FA15_3	29.0	2	4.9E-04	2.3E-05	5.2E-04	2.4E-05
FA15_3	29.0	3	4.8E-04	2.5E-05	5.0E-04	2.7E-05
FA16_4	23.2	1	6.1E-04	5.0E-05	4.9E-04	4.0E-05
FA16_4	23.2	2	6.2E-04	2.7E-05	4.9E-04	2.2E-05
FA16_4	26.2	1	1.6E-04	7.1E-07	1.4E-04	6.0E-07
FA16_4	26.2	2	1.6E-04	6.7E-07	1.4E-04	5.7E-07
FA16_4	29.3	1	7.9E-05	1.9E-06	7.1E-05	1.7E-06
FA16_4	29.3	2	8.8E-05	9.4E-07	7.9E-05	8.4E-07
FA16_4	32.0	1	2.5E-05	1.4E-07	2.4E-05	1.4E-07
FA16_5	25.9	1	3.9E-04	1.1E-05	3.1E-04	9.2E-06
FA16_5	25.9	2	4.2E-04	7.8E-06	3.4E-04	6.3E-06
FA16_5	29.0	1	3.2E-04	5.5E-06	2.9E-04	4.9E-06
FA16_5	29.0	2	3.2E-04	4.4E-06	2.9E-04	4.0E-06
FA16_5	32.1	1	4.0E-04	7.6E-06	4.3E-04	8.0E-06
FA16_5	32.1	2	4.0E-04	6.7E-06	4.3E-04	7.1E-06
FA16_5	32.1	3	4.0E-04	6.9E-06	4.3E-04	7.3E-06
FA16_5	32.1	4	4.1E-04	7.3E-06	4.4E-04	7.7E-06
FA16_6	12.3	1	1.1E-03	1.2E-04	8.8E-04	9.1E-05
FA16_6	12.3	2	8.4E-04	4.8E-05	6.5E-04	3.7E-05
FA16_6	16.9	1	3.5E-04	1.2E-05	3.0E-04	9.9E-06
FA16_6	16.9	2	3.6E-04	1.2E-05	3.1E-04	9.9E-06
FA16_6	24.5	1	2.7E-04	7.4E-06	2.5E-04	6.7E-06
FA16_6	24.5	2	2.7E-04	1.5E-05	2.4E-04	1.3E-05
FA16_6	32.0	1	2.6E-04	9.5E-06	2.4E-04	8.8E-06
FA16_6	32.0	2	2.5E-04	8.5E-06	2.4E-04	8.0E-06

REFERENCES

Adolph, A. C., and M. R. Albert (2014), Gas diffusivity and permeability through the firn column at Summit, Greenland: Measurements and comparison to microstructural properties, *Cryosph., 8*(1), 319–328, doi:10.5194/tc-8-319-2014.

Albert, M., C. Shuman, Z. Courville, R. Bauer, M. Fahnestock, and T. Scambos (2004), Extreme firn metamorphism: Impact of decades of vapor transport on near-surface firn at a low-accumulation glazed site on the East Antarctic plateau, *Ann. Glaciol., 39*(1), 73–78, doi:10.3189/172756404781814041.

Albert, M. R., and E. F. Shultz (2002), Snow and firn properties and air–snow transport processes at Summit, Greenland, *Atmos. Environ., 36*(15-16), 2789–2797, doi:10.1016/S1352-2310(02)00119-X.

Albert, M. R., E. F. Shultz, and F. E. Perron (2000), Snow and firn permeability at Siple Dome, Antarctica, *Ann. Glaciol., 31*(1), 353–356, doi:10.3189/172756400781820273.

Alley, R. B., T. K. Dupont, B. R. Parizek, and S. Anandakrishnan (2005), Access of surface meltwater to beds of sub-freezing glaciers: Preliminary insights, *Ann. Glaciol., 40*, 8–14, doi:10.3189/172756405781813483.

van Angelen, J. H., J. T. M. Lenaerts, S. Lhermitte, X. Fettweis, P. Kuipers Munneke, M. R. van den Broeke, E. van Meijgaard, and C. J. P. P. Smeets (2012), Sensitivity of Greenland ice sheet surface mass balance to surface albedo parameterization: A study with a regional climate model, *Cryosph., 6*(5), 1175–1186, doi:10.5194/tc-6-1175-2012.

van Angelen, J. H., J. T. M. Lenaerts, M. R. van den Broeke, X. Fettweis, and E. van Meijgaard (2013), Rapid loss of firn pore space accelerates 21st century Greenland mass loss, *Geophys. Res. Lett., 40*(10), 2109–2113, doi:10.1002/grl.50490.

Armstrong, R. L. (2008), *Snow and climate: Physical processes, surface energy exchange and modeling*, Cambridge Univ. Press.

Bell, R. E., W. Chu, J. Kingslake, I. Das, M. Tedesco, K. J. Tinto, C. J. Zappa, M. Frezzotti, and A. Boghosian (2017), Antarctic ice shelf potentially stabilized by export of meltwater in surface river, *Nat. Publ. Gr., 544*, doi:10.1038/nature22048.

Bilello, M. A. (1968), Water temperatures in a shallow lake during ice formation, growth,

and decay, *Water Resour. Res.*, *4*(4), 749–760, doi:10.1029/WR004i004p00749.

Bouwer, H. (1989), The Bouwer and Rice slug test - An update, *Groundwater*, *27*(3), 304–309, doi:10.1111/j.1745-6584.1989.tb00453.x.

Bouwer, H., and R. C. Rice (1976), A slug test for determining hydraulic conductivity of unconfined aquifers with completely or partially penetrating wells, *Water Resour. Res.*, *12*(3), 423–428, doi:10.1029/WR012i003p00423.

Braithwaite, R. J. (1985), Calculation of degree-days for glacier-climate research, *Zeitschrift fue Gletscherkd. und Glazialgeol.*, *20*, 1–8.

Bredehoeft, J. D., H. H. Cooper, and I. S. Papadopulos (1966), Inertial and storage effects in well-aquifer systems: An analog investigation, *Water Resour. Res.*, *2*(4), 697–707, doi:10.1029/WR002i004p00697.

Van Den Broeke, M., C. Bus, J. Ettema, and P. Smeets (2010), Temperature thresholds for degree-day modelling of Greenland ice sheet melt rates, *Geophys. Res. Lett.*, *37*(18), 1–5, doi:10.1029/2010GL044123.

Brown, D. L., T. N. Narasimhan, and Z. Demir (1995), An evaluation of the Bouwer and Rice method of slug test analysis, *Water Resour. Res.*, *31*(5), 1239–1246, doi:10.1029/94WR03292.

Butler, J. J. J. (1996), Slug tests in site characterization: Some practical considerations, *Environ. Geosci.*, *3*(3), 154–163.

Butler, J. J. J. (1997), *The design, performance, and analysis of slug tests*, CRC Press, New York.

Canfield, D. E., R. W. Bachmann, and M. V Hoyer (1983), Freeze-out of salts in hard-water lakes, *Limnol. Oceanogr.*, *28*(5), 970–977.

Carte, A. E. (1961), Air bubbles in ice, *Proc. Phys. Soc. Lond.*, *77*(3), 757–768.

Cazenave, A. (2006), How fast are the ice sheets melting?, *Science*, *314*(5803), 1250–1252, doi:10.1126/science.1133325.

Christianson, K., J. Kohler, R. B. Alley, C. Nuth, and W. J. J. van Pelt (2015), Dynamic perennial firn aquifer on an Arctic glacier, *Geophys. Res. Lett.*, *42*(5), 1418–1426, doi:10.1002/2014GL062806.

Chu, V. W. (2014), Greenland ice sheet hydrology: A review, *Prog. Phys. Geogr.*, *38*(1), 19–54, doi:10.1177/0309133313507075.

Church, J. A. et al. (2013), Sea Level Change. In: *Climate Change 2013: The Physical Science Basis. Contribution of Working Group I to the Fifth Assessment Report of*

the Intergovernmental Panel on Climate Change, edited by T.F. Stocker, et al., Cambridge University Press, Cambridge, U.K. and New York.

Cook, P. G., and J.-K. Böhlke (2000), Determining timescales for groundwater flow and solute transport, in *Environmental Tracers in Subsurface Hydrology*, pp. 1–30, Springer US, Boston, MA.

Cook, P. G., and D. K. Solomon (1997), Recent advances in dating young groundwater: Chlorofluorocarbons, 3H3He and 85Kr, *J. Hydrol.*, *191*(1), 245–265, doi:10.1016/S0022-1694(96)03051-X.

Das, S. B., I. Joughin, M. D. Behn, I. M. Howat, M. A. King, D. Lizarralde, and M. P. Bhatia (2008), Fracture propagation to the base of the Greenland ice sheet during supraglacial lake drainage, *Science*, *320*(5877), 778–781, doi:10.1126/science.1153360.

Drost, W., D. Klotz, A. Koch, H. Moser, F. Neumaier, and W. Rauert (1968), Point dilution methods of investigating ground water flow by means of radioisotopes, *Water Resour. Res.*, *4*(1), 125–146, doi:10.1029/WR004i001p00125.

Duffield, G. M. (n.d.), AQTESOLV, *HydroSOLVE, Inc.* Available from: http://www.aqtesolv.com/

Enderlin, E. M., I. M. Howat, S. Jeong, M.-J. Noh, J. H. van Angelen, and M. R. van den Broeke (2014), An improved mass budget for the Greenland ice sheet, *Geophys. Res. Lett.*, *41*(3), 866–872, doi:10.1002/2013GL059010.

Ettema, J., M. R. van den Broeke, E. van Meijgaard, W. J. van de Berg, J. L. Bamber, J. E. Box, and R. C. Bales (2009), Higher surface mass balance of the Greenland ice sheet revealed by high-resolution climate modeling, *Geophys. Res. Lett.*, *36*(12), L12501, doi:10.1029/2009GL038110.

Ferris, J. G., D. B. Knowles, R. H. Brown, and R. W. Stallman (1962), Theory of aquifer tests, *Water Supply Pap. U.S. Geol. Surv.*, 174.

Fettweis, X., M. Tedesco, M. Van Den Broeke, and J. Ettema (2011), Melting trends over the Greenland ice sheet (1958–2009) from spaceborne microwave data and regional climate models, *Cryosph.*, *5*, 359–375, doi:10.5194/tc-5-359-2011.

Focazio, M. J., L. N. Plummer, J. K. Bohlke, E. Busenberg, L. J. Bachman, and D. S. Powars (1998), Preliminary estimates of residence times and apparent ages of ground water in the Chesapeake Bay watershed, and water- quality data from a survey of springs, *Water-Resources Investig. Rep. 97-4225*.

Forster, R. R. et al. (2014), Extensive liquid meltwater storage in firn within the Greenland ice sheet, *Nat. Geosci.*, *7*(2), 1–4, doi:10.1038/ngeo2043.

Fountain, A. G. (1989), The storage of water in, and hydraulic characteristics of, the firn of South Cascade Glacier, Washington State, USA, *Ann. Glaciol.*, *13*, 69–75.

Fountain, A. G. (1996), Effect of snow and firn hydrology on the physical and chemical characteristics of glacial runoff, *Hydrol. Process.*, *10*(4), 509–521, doi:10.1002/(SICI)1099-1085(199604)10:4<509::AID-HYP389>3.0.CO;2-3.

Fountain, A. G., and J. S. Walder (1998), Water flow through temperate glaciers, *Rev. Geophys.*, *36*(97), 299, doi:10.1029/97RG03579.

Fourré, E., P. Jean-Baptiste, A. Dapoigny, D. Baumier, J. R. Petit, and and J. Jouzel (2006), Past and recent tritium levels in Arctic and Antarctic polar caps, *Earth Planet. Sci. Lett.*, *245*(1-2), 56–64, doi:10.1016/j.epsl.2006.03.003.

Freeze, A., and J. Cherry (1979), *Groundwater*, Prentice Hall, Englewood Cliffs, NJ.

Garber, M. S., and F. C. Koopman (1968), Methods of measuring water levels in deep wells, in *U.S. Geological Survey Techniques of Water-Resources Investigations*, p. 23.

Hall, D. K., J. C. Comiso, N. E. DiGirolamo, C. A. Shuman, J. E. Box, and L. S. Koenig (2013), Variability in the surface temperature and melt extent of the Greenland ice sheet from MODIS, *Geophys. Res. Lett.*, *40*(10), 2114–2120, doi:10.1002/grl.50240.

Harper, J., N. Humphrey, W. T. Pfeffer, J. Brown, and X. Fettweis (2012), Greenland ice-sheet contribution to sea-level rise buffered by meltwater storage in firn., *Nature*, *491*(7423), 240–3, doi:10.1038/nature11566.

Havely, E., H. Moser, O. Zellhofer, and A. Zuber (1967), Borehole dilution techniques a critical review, *Isot. Hydrol. I.A.E.A., Vienna*, 531–564.

Helm, V., A. Humbert, and H. Miller (2014), Elevation and elevation change of Greenland and Antarctica derived from CryoSat-2, *Cryosph.*, *8*(4), 1539–1559, doi:10.5194/tc-8-1539-2014.

Hock, R. (2003), Temperature index melt modelling in mountain areas, *J. Hydrol.*, *282*(1-4), 104–115, doi:10.1016/S0022-1694(03)00257-9.

Howat, I. M., I. Joughin, and T. A. Scambos (2007), Rapid changes in ice discharge from Greenland outlet glaciers, *Science*, *315*(5818), 1559–1561, doi:10.1126/science.1138478.

Hubbard, B., J. L. Tison, L. Janssens, and B. Spiro (2000), Ice-core evidence of the thickness and character of clear-facies basal ice: Glacier de Tsanfleuron, Switzerland, *J. Glaciol.*, *46*(152), 140–150, doi:10.3189/172756500781833250.

Humphrey, N. F., J. T. Harper, and W. T. Pfeffer (2012), Thermal tracking of meltwater

retention in Greenland's accumulation area, *J. Geophys. Res. Earth Surf.*, *117*(F1), n/a–n/a, doi:10.1029/2011JF002083.

Hvorslev, M. J. (1951), *Time lag and soil permeability in ground-water observations*, Bulletin No. 36, U.S. Army Corps of Engineers, Vicksburg, Mississippi.

Hyder, Z., and J. J. J. Butler (1995), Slug tests in unconfined formations: An assessment of the Bouwer and Rice technique, *Ground Water*, *33*(1), 16–22, doi:10.1111/j.1745-6584.1995.tb00258.x.

Hyder, Z., J. J. J. Butler, C. D. McElwee, and W. Liu (1994), Slug tests in partially penetrating wells, *Water Resour. Res.*, *30*(11), 2945–2957, doi:10.1029/94WR01670.

IAEA/WMO (2015), Global Network of Isotopes in Precipitation. The GNIP Database., Available from: http://www.iaea.org/water

Iken, A., K. Fabri, and M. Funk (1996), Water storage and subglacial drainage conditions inferred from borehole measurements on Gornergletscher, Valais, Switzerland, *J. Glaciol.*, *42*(141), 233–248.

IPCC (2014), *Climate Change 2013 - The Physical Science Basis*, edited by Intergovernmental Panel on Climate Change, Cambridge University Press, Cambridge.

Jacob, C. E. (1944), Notes on determining permeability by pumping tests under watertable conditions, *U.S. Geol. Surv.*, (Open File Report).

Jacob, C. E. (1947), Drawdown test to determine effective radius of artesian well, *Trans. Am. Soc. Civ. Eng.*, *112*, 1047–1064.

Jamin, P., P. Goderniaux, O. Bour, T. Le Borgne, A. Englert, L. Longuevergne, and S. Brouyère (2015), Contribution of the finite volume point dilution method for measurement of groundwater fluxes in a fractured aquifer, *J. Contam. Hydrol.*, *182*, 244–255, doi:10.1016/j.jconhyd.2015.09.002.

Jansson, P., R. Hock, and T. Schneider (2003), The concept of glacier storage: A review, *J. Hydrol.*, *282*(1), 116–129, doi:10.1016/S0022-1694(03)00258-0.

Joughin, I., S. B. Das, M. A. King, B. E. Smith, I. M. Howat, and T. Moon (2008), Seasonal speedup along the western flank of the Greenland ice iheet, *Science*, *320*(5877), 781–783, doi:10.1126/science.1153288.

Kameda, T., S. Takahashi, K. Goto-Azuma, S. Kohshima, O. Watanabe, and J. O. Hagen (1993), First report of ice core analyses and borehole temperatures on the highest icefield on western Spitsbergen in 1992, *Bull. Glacier Res.*, *11*, 51–61.

Van der Kamp, G. (1976), Determining aquifer transmissivity by means of well response tests: The underdamped case, *Water Resour. Res.*, *12*(1), 71–77, doi:10.1029/WR012i001p00071.

Kawashima, K. (1997), Formation processes of ice body revealed by the internal structure of perennial snow patches in Japan, *Bull. Glacier Res.*, *15*, 1–10.

Keegan, K., M. R. Albert, and I. Baker (2014), The impact of ice layers on gas transport through firn at the North Greenland Eemian Ice Drilling (NEEM) site, Greenland, *Cryosph.*, *8*(5), 1801–1806, doi:10.5194/tc-8-1801-2014.

Koenig, L. S., C. Miege, R. R. Forster, and L. Brucker (2014), Initial in situ measurements of perennial meltwater storage in the Greenland firn aquifer, *Geophys. Res. Lett.*, *41*(1), 81–85, doi:10.1002/2013GL058083.

Koerner, R. M. (1997), Some comments on climatic reconstructions from ice cores drilled in areas of high melt, *J. Glaciol.*, *43*(143), 90–97.

Kruseman, G. P., N. A. De Ridder, and J. M. Verwei (1994), *Analysis and Evaluation of Pumping Test Data*, 2nd ed., ILRI Publication, Wageningen, The Netherlands.

Kuipers Munneke, P., S. R. M. Ligtenberg, M. R. van den Broeke, J. H. van Angelen, and R. R. Forster (2014), Explaining the presence of perennial liquid water bodies in the firn of the Greenland Ice Sheet, *Geophys. Res. Lett.*, *41*(2), 476–483, doi:10.1002/2013GL058389.

Kulessa, B., B. Hubbard, M. Williamson, and G. H. Brown (2005), Hydrogeological analysis of slug tests in glacier boreholes, *J. Glaciol.*, *51*(173), 269–280, doi:10.3189/172756505781829458.

de la Peña, S., I. M. Howat, P. W. Nienow, M. R. van den Broeke, E. Mosley-Thompson, S. F. Price, D. Mair, B. Noël, and A. J. Sole (2015), Changes in the firn structure of the western Greenland ice sheet caused by recent warming, *Cryosph.*, *9*(3), 1203–1211, doi:10.5194/tc-9-1203-2015.

Langen, P. L., R. S. Fausto, B. Vandecrux, R. H. Mottram, and J. E. Box (2017), Liquid water flow and retention on the Greenland ice sheet in the regional climate model HIRHAM5: Local and large-scale impacts, *Front. Earth Sci.*, *4*, 110, doi:10.3389/feart.2016.00110.

Lenaerts, J. T. M. et al. (2016), Meltwater produced by wind–albedo interaction stored in an East Antarctic ice shelf, *Nat. Clim. Chang.*, *7*(1), 58–62, doi:10.1038/nclimate3180.

Lewis, S. M., and L. C. Smith (2009), Hydrologic drainage of the Greenland ice sheet, *Hydrol. Process.*, *23*(14), 2004–2011, doi:10.1002/hyp.7343.

Lindbäck, K., R. Pettersson, A. L. Hubbard, S. H. Doyle, D. van As, A. B. Mikkelsen, and A. A. Fitzpatrick (2015), Subglacial water drainage, storage, and piracy beneath the Greenland ice sheet, *Geophys. Res. Lett.*, *42*(18), 7606–7614, doi:10.1002/2015GL065393.

Luciano, G. L., and M. R. Albert (2002), Bidirectional permeability measurements of polar firn, *Ann. Glaciol.*, *35*(1), 63–66, doi:10.3189/172756402781817095.

Machguth, H., M. MacFerrin, D. van As, J. E. Box, C. Charalampidis, W. Colgan, R. S. Fausto, H. A. J. Meijer, E. Mosley-Thompson, and R. S. W. van de Wal (2016), Greenland meltwater storage in firn limited by near-surface ice formation, *Nat. Clim. Chang.*, *6*(4), 390–393, doi:10.1038/nclimate2899.

McKenzie, J. M., C. I. Voss, and D. I. Siegel (2007), Groundwater flow with energy transport and water–ice phase change: Numerical simulations, benchmarks, and application to freezing in peat bogs, *Adv. Water Resour.*, *30*(4), 966–983, doi:10.1016/j.advwatres.2006.08.008.

McLinn, E., and C. Palmer (1988), An electrical resistivity borehole-dilution device for the determination of ground-water flux, in *Proceedings of the Second National Outdoor Action Conference on Aquifer Restoration, Ground Water Monitoring and Geophysical Methods*, pp. 851–874.

Mcnerney, L. (2016), Constraining the Greenland firn aquifer's ability to hydrofracture a crevasse to the bed of the ice sheet, Master's Thesis, University of Utah. Available at: https://collections.lib.utah.edu/details?id=197636.

Meierbachtol, T. W., J. T. Harper, N. F. Humphrey, J. Shaha, and J. H. Bradford (2008), Air compression as a mechanism for the underdamped slug test response in fractured glacier ice, *J. Geophys. Res.*, *113*(F4), F04009, doi:10.1029/2007JF000908.

Miège, C., R. R. Forster, J. E. Box, E. W. Burgess, J. R. Mcconnell, D. R. Pasteris, and V. B. Spikes (2013), Southeast Greenland high accumulation rates derived from firn cores and ground-penetrating radar, *Ann. Glaciol.*, *54*(63), 322–332, doi:10.3189/2013AoG63A358.

Miège, C. et al. (2016), Spatial extent and temporal variability of Greenland firn aquifers detected by ground and airborne radars, *J. Geophys. Res. Earth Surf.*, *121*(12), 2381–2398, doi:10.1002/2016JF003869.

Miller, L. G., and G. R. Aiken (1996), Effects of glacial meltwater inflows and moat freezing on mixing in an ice-covered antarctic lake as interpreted from stable isotope and tritium distributions, *Limnol. Ocean.*, *41*(0), 966–976.

Miller, O. L., D. K. Solomon, C. Miège, L. S. Koenig, R. R. Forster, L. N. Montgomery, N. Schmerr, S. R. M. Ligtenberg, A. Legchenko, and L. Brucker (2017), Hydraulic conductivity of a firn aquifer in southeast Greenland, *Front. Earth Sci.*, *5*, 38,

doi:10.3389/feart.2017.00038.

Montgomery, L. N., N. Schmerr, S. Burdick, R. R. Forster, L. Koenig, S. Ligtenberg, C. Miège, O. L. Miller, K. Solomon, and A. Legchenko (2017), Investigation of firn aquifer structure in southeastern Greenland using active source seismology, *Front. Earth Sci., 5*, 10, doi:10.3389/FEART.2017.00010.

Moon, T., I. Joughin, B. Smith, and I. Howat (2012), 21st-century evolution of Greenland outlet glacier velocities, *Science*, *336*(6081).

Moon, T., I. Joughin, B. Smith, M. R. van den Broeke, W. J. van de Berg, B. Noël, and M. Usher (2014), Distinct patterns of seasonal Greenland glacier velocity, *Geophys. Res. Lett.*, *41*(20), 7209–7216, doi:10.1002/2014GL061836.

Neuman, S. P. (1982), Statistical characterization of aquifer heterogeneities: An overview, *GSA Spec. Pap.*, *189*, 81–102, doi:10.1130/SPE189-p81.

Nghiem, S. V. (2012), The extreme melt across the Greenland ice sheet in 2012, *Geophys. Res. Lett.*, *39*, doi:10.1029/2012GL053611.

Nienow, P., M. Sharp, and I. Willis (1998), Seasonal changes in the morphology of the subglacial drainage system, Haut Glacier d'Arolla, Switzerland, *Earth Surf. Process. Landforms*, *23*(9), 825–843, doi:10.1002/(SICI)1096-9837(199809)23:9<825::AID-ESP893>3.0.CO;2-2.

Oerter, H., and H. Moser (1982), Water storage and drainage within the firn of a temperate glacier (Vernagtferner, Oetztal Alps, Austria), in *Hydrological Aspects of Alpine and High Mountain Areas (Proceedings of the Exeter Symposium,)*, vol. 138, edited by J. W. Glen, pp. 71–81, IAHS Publ, Exeter.

Oerter, H., O. Reinwarth, and H. Rufli (1983), Core drilling through a temperate alpine glacier (Vernagtferner, Oetztal Alps) in 1979, *Zeitschrift für Gletscherkd. und Glazialgeol., 18 (1)*(1983), 1–11, doi:10013/epic.38420.d001.

Parizek, B. R., and R. B. Alley (2004), Implications of increased Greenland surface melt under global-warming scenarios: Ice-sheet simulations, *Quat. Sci. Rev.*, *23*(9-10), 1013–1027, doi:10.1016/j.quascirev.2003.12.024.

Parry, V., P. Nienow, D. Mair, J. Scott, B. Hubbard, K. Steffen, and D. Wingham (2007), Investigations of meltwater refreezing and density variations in the snowpack and firn within the percolation zone of the Greenland ice sheet, *Ann. Glaciol.*, *46*, 61–68, doi:10.3189/172756407782871332.

Pfeffer, W. (1991), Retention of Greenland runoff by refreezing: Implications for projected future sea level change, *J. Geophys. Res.*, *96*, doi:10.1029/91JC02502.

Pfeffer, W. T., M. F. Meier, and T. H. Illangasekare (1991), Retention of Greenland

runoff by refreezing: Implications for projected future sea level change, *J. Geophys. Res.*, *96*(C12), 22117, doi:10.1029/91JC02502.

Pitrak, M., S. Mares, and M. Kobr (2007), A simple borehole dilution technique in measuring horizontal ground water flow, *Ground Water*, *45*(1), 89–92, doi:10.1111/j.1745-6584.2006.00258.x.

Poinar, K., I. Joughin, D. Lilien, L. Brucker, L. Kehrl, and S. Nowicki (2017), Drainage of Southeast Greenland firn aquifer water through crevasses to the bed, *Front. Earth Sci.*, *5*, 5, doi:10.3389/FEART.2017.00005.

Richter-Menge, J., J. E. Overland, and J. T. Mathis (2016), Arctic Report Card, *Arct. Rep. Card*.

Risser, D. W., W. J. Gburek, and G. J. Folmar (2005), Comparison of methods for estimating ground-water recharge and base flow at a small watershed underlain by fractured bedrock in the eastern United States, *U.S. Geol. Surv. Sci. Investig. Rep.*, 31.

Ronen, D., M. Magaritz, N. Paldor, and Y. Bachmat (1986), The behavior of groundwater in the vicinity of the water table evidenced by specific discharge profiles, *Water Resour. Res.*, *22*(8), 1217–1224, doi:10.1029/WR022i008p01217.

Schneider, T. (1999), Water movement in the firn of Storglaciaren, Sweden, *J. Glaciol.*, *45*(150), 286–294, doi:10.3189/002214399793377211.

Schneider, T., and P. Jansson (2004), Internal accumulation in firn and its significance for the mass balance of Storglaciaren, Sweden, *J. Glaciol.*, doi:10.3189/172756504781830277.

Shepherd, A. et al. (2012), A reconciled estimate of ice-sheet mass balance, *Science*, *338*(6111), 1183–1189, doi:10.1126/science.1228102.

Smith, L. C. et al. (2015), Efficient meltwater drainage through supraglacial streams and rivers on the southwest Greenland ice sheet, *Proc. Natl. Acad. Sci.*, *112*(4), 1001–1006, doi:10.1073/pnas.1413024112.

Sole, A. J., D. W. F. Mair, P. W. Nienow, I. D. Bartholomew, M. A. King, M. J. Burke, and I. Joughin (2011), Seasonal speedup of a Greenland marine-terminating outlet glacier forced by surface melt–induced changes in subglacial hydrology, *J. Geophys. Res.*, *116*(F3), F03014, doi:10.1029/2010JF001948.

Steger, C. R. et al. (2017), Firn meltwater retention on the Greenland ice sheet: A model comparison, *Front. Earth Sci.*, *5*, 3, doi:10.3389/FEART.2017.00003.

Stone, D. B., and G. C. Clark (1972), Estimation of subglacial hydraulic properties frotn induced changes in basal water pressure : A theoretical fratnework for borehole-

response tests, *J. Glaciol.*, *39*(1), 327–340.

Taylor, K. C., J. W. Hess, S. W. Wheatcraft, and M. A. T. (1990), *Evaluation of selected borehole geophysical methods for hazardous waste site investigations and monitoring*, Desert Research Institute, US Environmental Protection Agency, Office of Research and Development, Environmental Monitoring Systems Laboratory.

Tedesco, M. (2013), Evidence and analysis of 2012 Greenland records from spaceborne observations, a regional climate model and reanalysis data, *Cryosphere*, *7*, doi:10.5194/tc-7-615-2013.

Theis, C. V. (1935), The relation between the lowering of the piezometric surface and the rate and duration of discharge of a well using ground-water storage, *Trans. Am. Geophys. Union*, *16*, 519–524, doi:10.1029/TR016i002p00519.

Titus, J. G., R. A. Park, S. P. Leatherman, J. R. Weggel, M. S. Greene, P. W. Mausel, S. Brown, C. Gaunt, M. Trehan, and G. Yohe (1991), Greenhouse effect and sea level rise: The cost of holding back the sea, *Coast. Manag.*, *19*(2), 171–204, doi:10.1080/08920759109362138.

Tóth, J. (1963), A theoretical analysis of groundwater flow in small drainage basins, *J. Geophys. Res.*, *68*(16), 4795–4812, doi:10.1029/JZ068i016p04795.

Vallon, M., J.-R. Petit, and B. Fabre (1976), Study of an ice core to the bedrock in the accumulation zone of an Alpine glacier, *J. Glaciol.*, *17*, 13–28.

Vaughan, D. G. et al. (2013), Observations: Cryosphere. In: *Climate Change 2013: The Physical Science Basis. Contribution of Working Group I to the Fifth Assessment Report of the Intergovernmental Panel on Climate Change*, edited by T.F. Stocker, et al., Cambridge University Press, Cambridge, U.K. and New York.

Voss, C. I., and A. Provost (2010), SUTRA: A model for saturated-unsaturated variable density groundwater flow with solute or energy transport, *U.S. Geol. Surv. Water-Resources Investig. Rep. 02-4231*, 291.

Van Der Wel, L. G., H. J. Streurman, E. Isaksson, M. M. Helsen, R. S. W. Van De Wal, T. Martma, V. A. Pohjola, J. C. Moore, and H. A. J. Meijer (2011), Using high-resolution tritium profiles to quantify the effects of melt on two Spitsbergen ice cores, *J. Glaciol.*, doi:10.3189/002214311798843368.

Zlotnik, V. (1994), Interpretation of slug and packer tests in anisotropic aquifers, *Groundwater*, *32*(5), 761–766, doi:10.1111/j.1745-6584.1994.tb00917.x.

Zwally, H. J. (2002), Surface melt-induced acceleration of Greenland ice-sheet flow, *Science*, *297*(5579), 218–222, doi:10.1126/science.1072708.